General Disclaimer

One or more of the Following Statements may affect this Document

- This document has been reproduced from the best copy furnished by the organizational source. It is being released in the interest of making available as much information as possible.

- This document may contain data, which exceeds the sheet parameters. It was furnished in this condition by the organizational source and is the best copy available.

- This document may contain tone-on-tone or color graphs, charts and/or pictures, which have been reproduced in black and white.

- This document is paginated as submitted by the original source.

- Portions of this document are not fully legible due to the historical nature of some of the material. However, it is the best reproduction available from the original submission.

ARKANSAS
REMOTE SENSING
LABORATORY

ANALYSIS OF GEOLOGIC TERRAIN MODELS FOR DETERMINATION OF OPTIMUM SAR SENSOR CONFIGURATION AND OPTIMUM INFORMATION EXTRACTION FOR EXPLORATION OF GLOBAL NON-RENEWABLE RESOURCES:

PILOT STUDY

ARKANSAS REMOTE SENSING LABORATORY

ARSL TR 81-2

Part II Authors

V. H, Kaupp, Asst. Professor,
Dept. of Electrical Engineering
H. C. MacDonald, Professor,
W. P. Waite, Professor,
Dept. of Electrical Engineering
University of Arkansas, Fayetteville, Arkansas 72701

Part III Authors

J. A. Stiles
F. S. Frost
K. S. Shanmugam, Assoc. Professor
S. A. Smith
V. Narayanan
J. C. Holtzman, Professor
Remote Sensing Laboratory
University of Kansas Center for Research, Inc.
Lawrence, Kansas 66045

UNIVERSITY OF ARKANSAS

FAYETIEVILLE, ARKANSAS 72701

ANALYSIS OF GEOLOGIC TERRAIN MODELS FOR DETERMINATION OF OPTIMUM SAR SENSOR CONFIGURATION AND OPTIMUM INFORMATION EXTRACTION FOR EXPLORATION OF GLOBAL NON-RENEWABLE RESOURCES:

PILOT STUDY

ARKANSAS REMOTE SENSING LABORATORY

ARSL TR 81-2

Part II Authors

V. H, Kaupp, Asst. Professor,
Dept. of Electrical Engineering
H. C. MacDonald, Professor,
W. P. Waite, Professor,
Dept. of Electrical Engineering
University of Arkansas, Fayetteville, Arkansas 72701

Part III Authors

J. A. Stiles
F. S. Frost
K. S. Shanmugam, Assoc. Professor
S. A. Smith
V. Narayanan
J. C. Holtzman, Professor
Remote Sensing Laboratory
University of Kansas Center for Research, Inc.
Lawrence, Kansas 66045

ABSTRACT

Part II Abstract

A tradeoff analysis has been started using computer-generated radar simulations and mathematical geologic terrain models for establishing the optimum radar sensor operating parameters for geologic research. An initial set of mathematical geologic terrain models has been created for three basic landforms. Families of simulated radar images have been prepared from these terrain models for numerous interacting sensor, platform, and terrain variables. Selected images are shown to establish that computer-generated radar image simulation and geologic terrain modeling afford powerful tools for conducting parametric optimization studies. Three detailed analyses using computer-generated radar image simulation and geologic terrain modeling are provided in the appendices.

Part III Abstract

Two research problems pertaining to synthetic aperture radar for geologic mapping applications have been investigated: (1) the tradeoffs between the various sensor parameters and the quantity and quality of the extractable geologic data and (2) the development of automated techniques of digital SAR image analysis. Initial work on a texture analysis of Seasat SAR imagery is reported; the gray level co-occurrence matrix approach was utilized to produce results. Synthesis of simple terrain models, imaging radar models, and implementation of the two as a ground truth data base and simulation algorithms have been accomplished. Computer-generated radar simulations are shown for combinations of two geologic models and three SAR angles of incidence.

PREFACE

A one-year pilot study has been completed by the Universities of Arkansas and Kansas in a joint effort to define an optimum SAR (synthetic aperture radar) sensor and an interpretation system for global exploration of non-renewable resources via radar remote sensing. This report relates the work and accomplishments of the past year at both universities and identifies the present status of the research program.

The report is divided into three parts. Part I consists of introductory material describing the purpose and scope of work performed in the pilot study, background information, and an overview of the program as a whole, as well as a statement of the actual work performed and a summary of the present status of the work. Part II describes the work and accomplishments at the University of Arkansas, and Part III relates those at the University of Kansas. This structure was adopted because the two efforts were sufficiently disparate that an integrated approach to preparing a report was impractical. In addition, analysis conducted during the pilot study are reported in three appendices.

TABLE OF CONTENTS

LIST OF FIGURES

LIST OF TABLES

PART I

INTRODUCTION

Chapter 1

INTRODUCTION

The Universities of Arkansas and Kansas have completed a one-year pilot study to initiate the research necessary to define an optimum SAR (synthetic aperture radar) sensor and interpretation system for global exploration of non-renewable resources. In this initial work, terrain modeling and radar image simulation techniques have been developed for use in subsequent phases of the overall program. An intial set of textbook-example terrain models has been developed and simulated radar images prepared from them. Computer-modeling via image simulation is concluded to be a cost-effective method for evaluating terrain variations, predicting results, and defining optimum sensor parameters. In addition, a preliminary texture analysis of radar imagery was performed and analysis of the radar system response for geologic targets was started.

1.1 PURPOSE

The goals pursued in this pilot study were (1) development of key research techniques (i.e., terrain modeling and image simulation), (2) initiation of critical analyses (i.e., texture analysis of radar imagery and radar system response for geologic targets), and (3) creation of preliminary results for simple test cases. These goals were all necessary to demonstrate the feasibility of using computer-modeling techniques to attain the dual program goals of (1) defining an optimum SAR sensor system and (2) developing an interpretation strategy for global exploration of non-renewable resources using microwave remote sensing.

1.2 SCOPE

Because of the low level of funding for this effort, the research was limited to performing a pilot study in three primary areas of geologic modeling: (1) mineral exploration, (2) petroleum exploration, and (3) study of igneous activity. The pilot study was limited to work with simple textbook-example cases.

1.3 BACKGROUND

The search for and management of non-renewable resources on both regional and global scales need no lengthy justification. The ability of radar remote sensing to contribute significantly to these critical efforts has been well documented with the studies of Dellwig et al. [1], MacDonald [2], Wing [3], Wing and MacDonald [4], Dellwig et al. [5], MacDonald [6], and Dellwig and Moore [7].

Geologists have done an impressive job of imagery interpretation and of development of geologic models that require a minimum of calibration where image recognition elements such as tone, texture, pattern, shadow, size, shape, and context are prime discriminants. These geologic models are much like the three-dimensional concepts achieved in the field, where outcrop observations provide information for geologic maps (i.e., the plan view) and structural cross-sections of the subsurface. Radar imagery enables the geologist to analyze systematically the visual pattern elements of the terrain (i.e., drainage, vegetation, landforms, etc.) for geologic significance, and develop geologic models rapidly. Models ultimately provide the geologist with insight into the three-dimensional structure (i.e., inferences about landform type and origins, rock characteristics, and structural complexity).

Since 1969, commercial radars have provided imagery for geologic mapping in parts of South America, Central America, Southeast Asia, Africa, and the United States. The most impressive radar mapping program ever conducted was the Aero Service/Goodyear project RADAM (RAdar of the AMazon) [8]. The entire country of Brazil, about 8.5 million sq km, was eventually imaged for natural resource studies. Clearly, radar remote sensing has proven potential in aiding global exploration for non-renewable resources.

Although to date most of the proven benefits of radar remote sensing have arisen from geologic interpretation for non-renewable resouces, relatively little research has been devoted to the development of optimum specifications for the radar sensor, or for optimum strategies for information extraction from radar data. Surprisingly, advances in applied radar geologic research (i.e., the development of techniques that will aid in mapping of surface/tectonic features) have been spearheaded by the private sector. For many years only a limited number of radar systems were available for geologically dedicated research programs, and evaluation consisted of empirical observations derived from analysis of imagery. Research was conducted with only a limited number of combinations of sensor parameters such as frequency, polarization, depression angle, look direction, and resolution. Until now, the geometric distortions (i.e., layover,

foreshortening, etc.) and scattering phenomena caused by the various geologic features (i.e., predominatly landforms) could not be modeled, nor could their characteristic expression in an image be realized.

This inability to control system parameters has been overcome with the advent of computer modeling techniques via radar image simulations. Definitive studies to optimize the complete radar remote sensing system (including sensor, image processing, and interpretation) can now be done. Image simulation provides a cost-effective method for modeling of terrain variation, prediction of results, and definition of optimum sensor parameters.

A research program is being conducted to achieve optimization of both an imaging radar system and a total remote sensing system for non-renewable resource exploration. The research effort involves developing mathematical models of complex geologic structures, producing families of simulated radar images for these geologic models, evaluating both the models and simulations, and from these developing interpretation strategies and the best radar configuration for geologic exploration. This report relates the initial work completed in a pilot study for this research.

Chapter 2

OVERVIEW

A proposal entitled "Analysis of Geologic Terrain Models for Determination of Optimum SAR Sensor Configuration and Optimum Information Extraction of Global Non-Renewable Resources," was submitted to NASA headquarters in July 1979. This proposal was submitted in response to OSTA-79-A for the Resource Observation Division, Non-Renewable Resources Program. It consisted of a systematic plan for the Universities of Arkansas and Kansas, in a joint program, to conduct the necesary research over a three-year period to define an optimum SAR sensor and interpretation system for global exploration of non-renewable resources via radar remote sensing. This project was funded as a one-year pilot study for approximately 42% of the original request (NASA Contract NAG 9-3). Despite the shortfall and its imposed reduction in scope for the effort, substantial progress has been made to date. The significant results attained in the pilot study are largely the result of two important factors:

1. The originally proposed task descriptions were modified to establish a research effort compatible with reduced external fudnding.

2. The matching contributions of the Universities of Arkansas and Kansas were increased significantly for the pilot study.

The research performed during the past year has been to develop the means by which the overall program can be accomplished in a subsequent three-year period. A central goal of the program is to determine the interpretation strategy and best radar sensor configuration for geologic exploration. Accomplishment of this goal requires analysis of multiple parameter radar imagery. Past experience has shown that the acquisition of multiple parameter radar imagery over extensive control sites is not economically feasible, except for specific and very limited objectives. Thus, a major objective of the pilot study was to develop the means by which studies can be conducted through computer modeling (i.e., simulation), thereby affording the control of variables needed to establish mathematical description of the terrain-sensor interaction. Terrain modeling and radar image simulations are the computer modeling tools used to perform these extensive parametric and sensitivity studies.

The approach followed in developing the computer modeling capability is a logical progression through several phases of increasing complexity. These phases are numerically labeled 1st order (i.e., deterministic models), 2nd order (i.e., natural terrain models), and 3rd order (i.e., realistic models).

The research performed in developing the radar image simulations and terrain modeling capabilities is specified in the following section, and the various phases of the computer modeling are described in a subsequent section.

2.1 WORK PERFORMED

The following tasks were performed during the pilot study.

1. Develop Geologic Terrain Models. This task consisted of identifying the landscape expression of key geologic features for exploration of non-renewable resources, and developing mathematical models (i.e., deterministic or 1st order) to represent their geometric properties such as shape, slope, relief, etc.

2. Produce Simulated Radar Images. Simulated radar images were produced from the 1st order geologic models by use of empirical and theoretical backscatter functions for an extensive matrix of parameters of both radar and terrain.

3. Perform Initial Parametric Sensitivity Analysis. An initial family of simulated images was produced and analyzed for a range of parameters from each of the 1st order terrain models.

The primary focus of the work performed in the pilot study is the development of 1st order geologic or terrain models. As the study progresses, complex models wil be developed from these simple ones. They will be used to facilitate extensive parametric studies.

2.2 TERRAIN MODELS DEFINED

Several geologic test sites have been selected where the surface characteristics of the terrains have been proven to be correlative with the subsurface structures. These sites represent essentially classic examples of the landform expression of common geologic structures of perhaps several erosional stages.

Subtly expressed geologic features are considered in stages as 1st order, 2nd order, and 3rd order terrain models. These terrain models are mathematical representations of the geometric properties such as shape, slope, relief, etc., of the geologic features. The terrain models are developed in a logical progression of phases from 1st order to 3rd order.

1st order models are deterministic. These models are composed of relatively simple geometric shapes that are analytically defined. For example, a ridge, in plan view, may be formed in the shape of a parabola, or ellipse, to represent a syncline or anticline. This technique can be extended further to consider the effect on the surface expression of different folding periods and pitch angles. The main features of 1st order models are that they are completely deterministic and are used to investigate parametric behavior and sensitivity of specific geometric shapes.

2nd order models are natural terrain elevation models. The 2nd order model is the actual elevation surface for a region of terrain containing a well-defined example of one of the 1st order models (e.g., an anticline or syncline geologic structure). A typical digital elevation model (i.e., a 2nd order model) can be acquired from digital elevation tapes such as those produced by NCIC (National Cartographic Information Center) [9]. The problem with a digital elevation model as acquired is the sampling frequency. The elevation surface is sampled once every 30 m in two orthogonal horizontal directions. This frequency is not adequate to support simulating SAR's having 30 m resolution. This is a problem which must be solved. As a first approach, frequency plane interpolation via the FFT [10] and the technique of adding zeroes to increase the apparent sampling rate will be investigated. A feature of the 2nd order model is that the entire elevation surface will be treated as though it were covered with a homogeneous scattering category. That is, each radar image simulated will portray the ground in the region of the feature as though it were uniformly covered with a single type of scattering category. This means that the 2nd order model adds geologic noise such as drainage patterns and weathering characteristics to the stark portrayal of the 1st order one. In essence, the 1st order model allows for analysis in the absence of noise, whereas the 2nd order model permits evaluation in the presence of noise.

3rd order models are realistic. The 3rd order model represents an extension of the 2nd order one to obtain a more faithful portrayal of the terrain. It consists of the actual elevation surface together with the actual terrain cover boundaries of a region of terrain. It is, then, a 2nd order model with natural terrain cover boundaries added.

Creation of these models for specific test sites will involve much more effort than is needed for 1st or 2nd order models and will require extensive and detailed ancillary land use data for each site.

The 3rd order models will be exploited simply to provide confidence that the simulation transformations produce valid replicas of what would be recorded by an actual microwave imaging system. They also provide a model for evaluating the effect portrayed in a radar image of terrain masking by its cover.

Chapter 3

SUMMARY AND CONCLUSIONS

Because of the low level of funding, the research was limited to performing a pilot study which could be done for simple, textbook-example cases. In spite of this limitation, important preliminary results have shown that computer-generated radar image simulation and mathematical geologic terrain modeling are valid and valuable research tools for obtaining an optimum SAR configuration for exploration of global non-renenwable resources.

The detail and fidelity portrayed in a radar image depend upon both the sensor system parameters and the landform geometry. The interactions between system and terrain variables are extremely complex. Computer simulation affords a number of significant advantages over actual imagery for research. Chief among them is the capability of exercising rigorous mathematical control over both the input and the transformation of the input into an image. In addition, simulation affords a rigorous methodology for evaluating and comparing the results produced by different radar configurations viewing the same scene and by the same (or a different) radar viewing different scenes.

A general conclusion is reached that the research started and work completed in the pilot study provide the groundwork for attaining the ambitious goal set for the overall program. The different approaches followed at the two universities are intended to converge for attaining the goals of the program. These approaches are discussed separately.

3.1 SUMMARY OF WORK AT THE UNIVERSITY OF ARKANSAS

The approach followed at the University of Arkansas is a logical progression through several phases of increasing complexity. In the first phase (i.e., the work reported in this pilot study), 1st order geologic terrain models have been developed for three classes of basic geologic landforms, families of radar images have been simulated from them for numerous different parameters, and preliminary analyses have been conducted. These models will be extended and refined in succeeding phases (i.e., in subsequent years) from the simple, stark terrain models of the first phase to

more complex and realistic terrain models in the second and third phases.

Preliminary analyses have shown the simulated data to provide valuable information for understanding the sensor/terrain interaction as portrayed visually in an image. Extrapolation of these analyses indicates that this approach using computer modeling is feasible and that the dual goals of the program will be attained.

3.2 SUMMARY OF WORK AT THE UNIVERSITY OF KANSAS

The approach followed at the University of Kansas addresses two basic research problems with synthetic aperture radar: (1) the tradeoffs between the various sensor parameters and the quantity and quality of the extractable geologic data and (2) the development of automated techiques of digital SAR image analysis.

The analysis portion of the work shows promise for texture measures of SAR images using the GLC matrix approach. The look angle dependence of the GLC results must be investigated because these effects must be factored into future use of automated texture analysis.

The synthesis portion of the work produced geolgic feature data bases for linear and elliptical hogback ridges.

PART II

STUDIES PERFORMED AT THE UNIVERSITY OF ARKANSAS

Chapter 4

FOREWORD

Real and synthetic aperture radars are used most commonly for remote sensor surveys. In the usual geometry, side-looking radars employ an antenna with its long axis along the velocity vector of the platform. In this configuration, the antenna emits a narrow beam of electromagnetic energy to the side. This electromagnetic energy, transmitted at a desired microwave frequency, travels at the speed of light to the ground. A complex interaction occurs at the ground and a small fraction of the energy is reradiated, or backscattered, to the antenna. The backscattered energy returning to the radar from a single pulse is recorded versus time (i.e., amplitude versus distance) thereby forming a single line of an image. A series of short pulses is transmitted and the returning backscattered energy from each is recorded in sequence to build a continuous strip image pulse by pulse, line by line.

The return backscattered energy is received as a function of the slant range distance (i.e., the propagation time) from the platform to the ground. It is this property which introduces geometric effects such as layover, range compression, and shadow into radar imagery. Radar imagery collected at relatively small angles of incidence exhibits pronounced layover and foreshortening in high-relief areas, whereas imagery taken at larger incidence angles in similar terrain is characterized by extensive shadowing. In an image, areas of foreshortening are bright because foreslopes typically are compressed into a small image area. Also, the percentage of energy backscattered from the foreslope of a hill or ridge typically is greater than that from a backslope. Thus, depending on the angle of incidence, foreslopes are characteristically bright and backslopes are dark in a radar image.

In most cases both geometric and backscatter effects are simultaneously present in an image. For accurate geologic interpretation, the desired radar imagery is that which distorts least and enhances most the landforms or terrain characteristics most indicative of geologic features. It is important, therefore, to determine the optimum set of system parameters for imaging each different class of geologic features.

Propagation and backscatter are not the only effects important in determining the image expression of geologic features. They are the principal factors among many which contribute to the spatial presentation and visual tone of each feature as expressed in a radar image. Several other contributing factors are listed in Table 1.

TABLE 1

Principal Radar Image Factors

1. System parameters
   a) Frequency (wavelength)
   b) Polarization
   c) Resolution
   d) Incidence angle
   e) Fading
2. Platform parameters
   a) Altitude
   b) Aspect angle
3. Terrain parameters
   a) Slope
   b) Relief
   c) Surface roughness
   d) Surface cover

An important means of separately evaluating the contribution of each of the interacting parameters is offered by computer-generated geologic terrain models and radar image simulations. Geologic terrain models are mathematical representations of characteristic landforms indicative of subsurface geologic structure. Radar images are simulated from these models for a variety of the imaging parameters noted in Table 1. The simulated radar images portray the surface topography (i.e., landforms) for each geologic feature char-

acterized in a model. The simulated radar images, together with the geologic models, form the basis for all the subsequent evaluations. Geologic terrain models and radar image simulations are discussed separately in the following chapters.

Chapter 5

GEOLOGIC TERRAIN MODELS

In this initial work, several 1st order geologic terrain models have been created. They provide, in spite of their unrealistic and stark appearance, ideal constructions for evaluating how the radar scene changes for a specific geologic feature as radar sensor parameters are changed. An example of such a geologic terrain (i.e., landscape) model and its use in radar parameter evaluation is presented in Appendix A [11].

The geologic terrain models constructed in the pilot study are listed in Table 2. They constitute a basic set for construction of more complex geologic landforms or regions.

TABLE 2

Basic Geologic Landforms

1. Basic linear landforms
   a) Hogback ridges
   b) Homoclinal ridges
2. Basic domal landforms
3. Basic curvilinear landforms
   a) Breached anticline
   b) Breached anticline/syncline

These features are not the only ones for which 1st order geologic terrain models can be constructed. They are merely the first to be modeled in this pilot study. Each landform is discussed separately in the following sections.

5.1 BASIC LINEAR LANDFORMS

Geologic terrain models have been created for the basic linear landforms illustrated in Figure 1. These represent both homoclinal ridges and hogback ridges.

Each linear landform has been embedded five times in its own rectangular matrix, each placement representing a different look direction to the radar. This general scheme is illustrated in Figure 2. As can be seen from the figure, a given linear feature is oriented so that with a radar viewing the scene from the top of the figure, the feature is viewed from 0, 22.5, 45, 67.5, and 90 degrees. Simulated radar images created from a given geologic terrain model thus contain the image expression of that feature for all look directions as captured by a specific radar.

First order hogback ridges are treated here as stark, perfectly straight, symmetrical landforms which represent steeply dipping strata (i.e., the dip is generally greater than 45 degrees) exposed at the earth's surface. Where a sequence of steeply dipping rocks is truncated by erosion, the outcrop pattern (i.e., landforms) commonly appears as bands or hogbacks which, on a regional basis, are roughly parallel.

First order homoclinal ridges are represented as asymmetrical landforms which represent less steeply dipping strata (i.e., the dip is generally less than 45 degrees) than hogback ridges. There is a notable difference in the steepness as well as the length of the front and back slopes. These characteristic shapes often provide the geologist with distinctive clues for determining the strike and dip of formations.

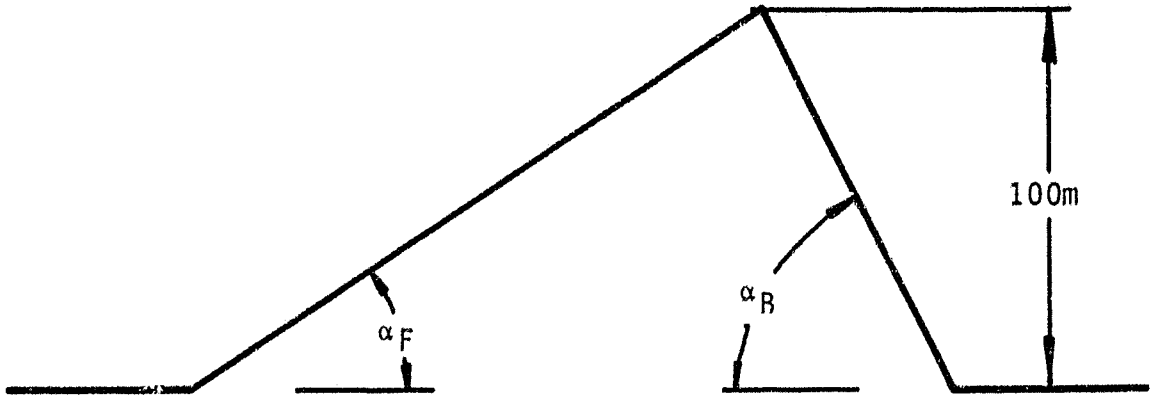

Foreslope; α_F	Backslope; α_B 10	20	30	40
10	X	X	X	X
20	X	X	X	X
30	X	X	X	X
40	X	X	X	X

Figure 1: Basic Linear Landforms

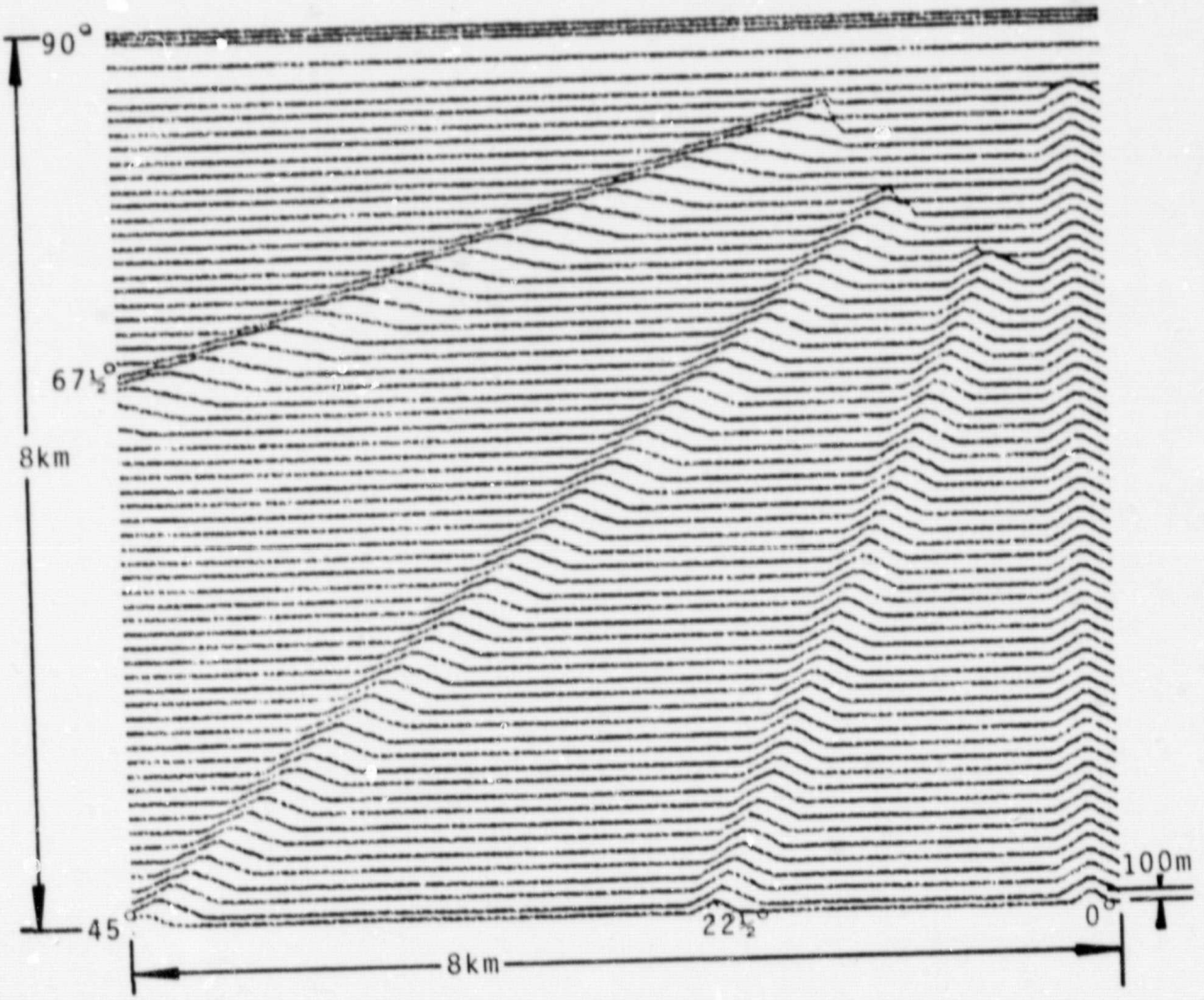

Figure 2: Landform Orientation

5.2 BASIC DOMAL LANDFORMS

Dome-shaped structures form a roughly circular to elliptical landform pattern with strata dipping away from a central area. These structures may range in size from small unbreached warps a few meters in diameter to regional features covering hundreds or thousands of square kilometers. A 1st order geologic terrain model of a dome-shaped landform is illustrated in Figure 3.

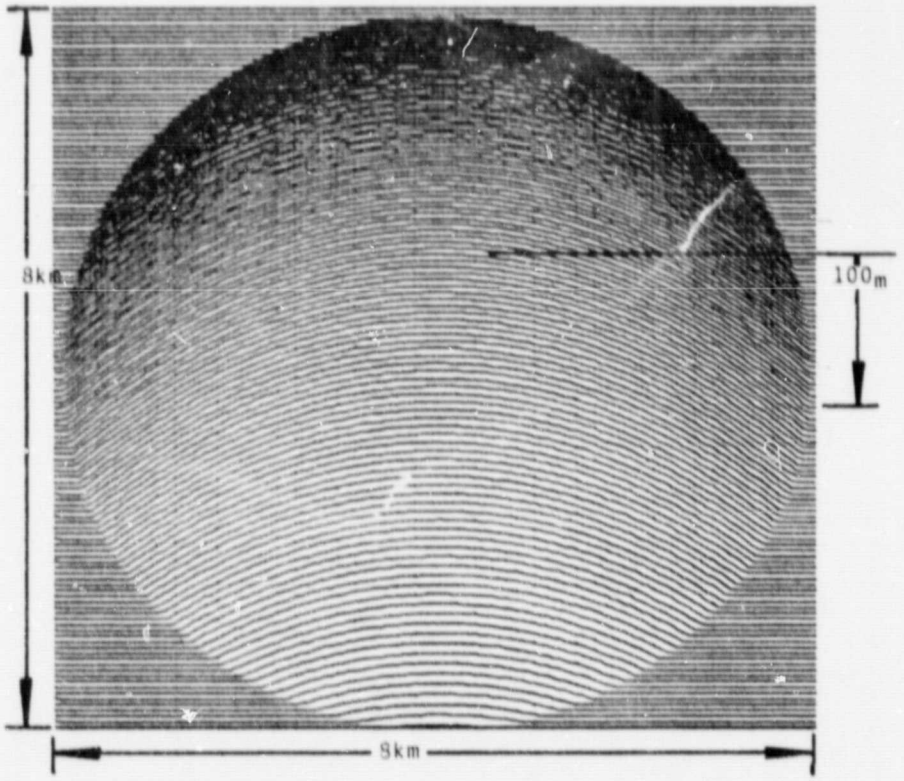

Figure 3: Basic Domal Feature Terrain Model

5.3 BASIC CURVILINEAR LANDFORMS

The first curvilinear geologic terrain model created was that of a simple anticline. The most complex 1st order curvilinear geologic terrain model created to date is the anticline and syncline structure shown in Figure 4 embedded in a square region (i.e., a square matrix). The simple zig-zag patterns are characteristic landforms resulting from differential erosion of gently folded, plunging structures. Folding is one of the most common types of structural deformation and these characteristic landform patterns are generally found in complex mountain ranges as well as less deformed lowlands.

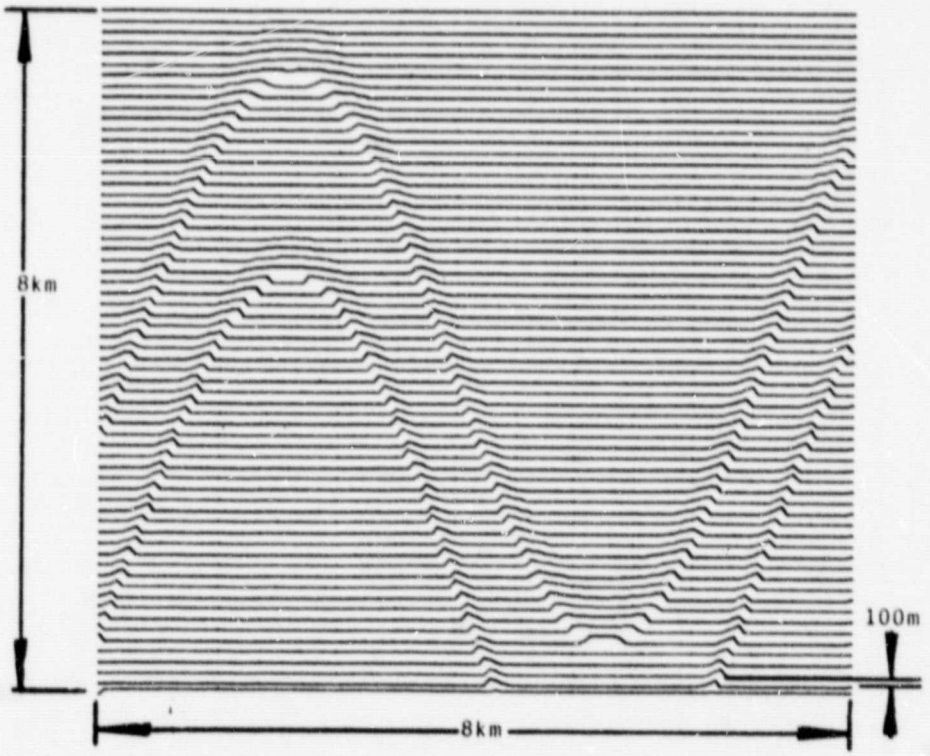

Figure 4: Anticline/Syncline Terrain Model

Chapter 6

RADAR IMAGE SIMULATION

Radar image simulation refers to synthesizing via a digital computer the image which an actual radar would have produced if it were flown. Radar image simulation is an extremely useful diagnostic and research tool. Simulation affords a number of significant advantages over actual imagery for research. Among these are the capability of exercising rigorous mathematical control over both the input (called a data base) and the transformation of the input into an image. In addition, simulation affords a rigorous methodology for evaluating and comparing the results produced by different radars as well as the results produced by changing various parameters of a specific design. Simulation also allows separation and individual evaluation of effects which are inextricably coupled in actual imagery, such as backscatter and propagation.

A very general approach to simulation has been developed at the University of Arkansas [12]. Figure 5 is a block diagram of the computer programs. The required inputs to the simulation programs are a data base and a backscatter file. As can be seen from the figure, the simulation computer programs can produce selected intermediate and final results: (1) power-map image, (2) slant-range image, (3) ground-range image, (4) slant-range image with noise, and (5) ground-range image with noise. Antenna and resolution effects can be incorporated by processing either in the spatial domain via convolution, or in the spatial frequency domain via the Fast Fourier Transform and multiplication.

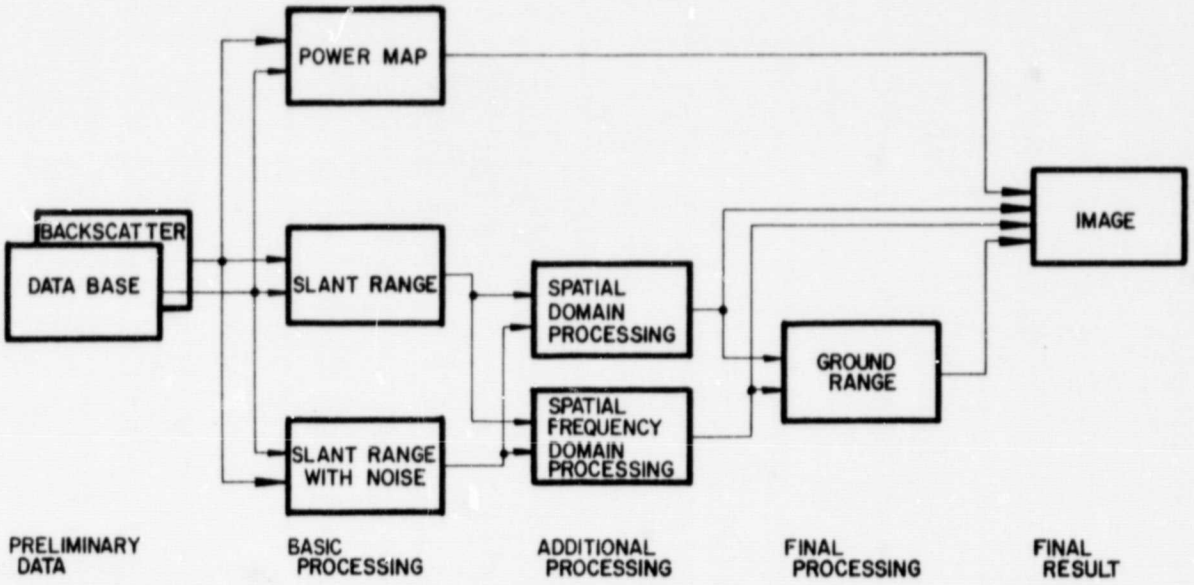

Figure 5: Block Diagram of Simulation Programs

6.1 BACKSCATTER

Radar return from the ground is described by the differential scattering cross-section, and is often called backscatter. Backscatter determines the percentage of electromagnetic energy which is reradiated back to the radar from each scattering element within a resolution cell. A resolution cell is considered to consist of many individual features or objects in relation to the scale of the radar wavelength, and each of these is termed a scattering element. A resolution cell is defined, for a short-pulse, side-looking imaging radar, to be the instantaneous area on the ground from which the backscatter arrives at the radar antenna simultaneously from each individual scattering center.

Variation of the intensity or shade of gray (i.e., tone) in radar images portrays the relative strength of the radar signal returned to the receiver from point to point on the ground. Variation of the radar signal arises from numerous interacting and complex causes. Two fundamental causes are (1) the interaction between the ground and the transmitted electromagnetic energy illuminating the ground (2) the geometric or propagation phenomena associated with the fact that radar is a ranging device (i.e., it records the returned signal versus time and thus orders features according to their individual distances, or ranges, to the radar). These causes are both discussed in a paper in Appendix B [13].

Typically, the percentage of energy backscattered from slopes facing a radar is greater than that from level terrain and from slopes facing away from a radar. Foreslopes are generally depicted in an image as brighter tones than level ground, and brighter still than backslopes. For the various terrain cover types present, this difference is governed by the backscatter trends versus the local angle of incidence (i.e., the angle between the local vertical and a line to the radar). The geometric relationships are illustrated in Figure 6.

Changes in backscatter arise from numerous sources, among the more important of which are (1) complex permittivity (both conductivity and permittivity), and (2) Roughness of the subsurface in relation to the radar wavelength to the depth where the electromagnetic wave is sufficiently attenuated. If the geometry and complex permittivity of two targets were identical, the target having the rougher surface would have the stronger return. The reason is that relatively smooth surfaces tend to reflect electromagnetic energy specularly, whereas extremely rough surfaces, called diffuse reflectors, tend to reradiate energy nearly uniformly in all directions. Specular surfaces produce an extremely strong return only when the angle of incidence is nearly normal to the surface (i.e., when the angle of reflection equals the angle of incidence). Rough surfaces produce a relatively strong radar return in any direction. In contrast, if the geometry and surface roughness of two targets were identical, the target having the higher complex permittivity would have the stronger return.

Figure 7 illustrates the general trends of backscatter versus angle of incidence. The four trends illustrated represent the average backscatter response for four very different types of ground: (1) specular or smooth, (2) slightly rough, (3) moderately rough, and (4) extremely rough. The surface which is smooth in relation to the radar wavelength produces an extremely strong return only when the angle of incidence is nearly normal to the surface, and the

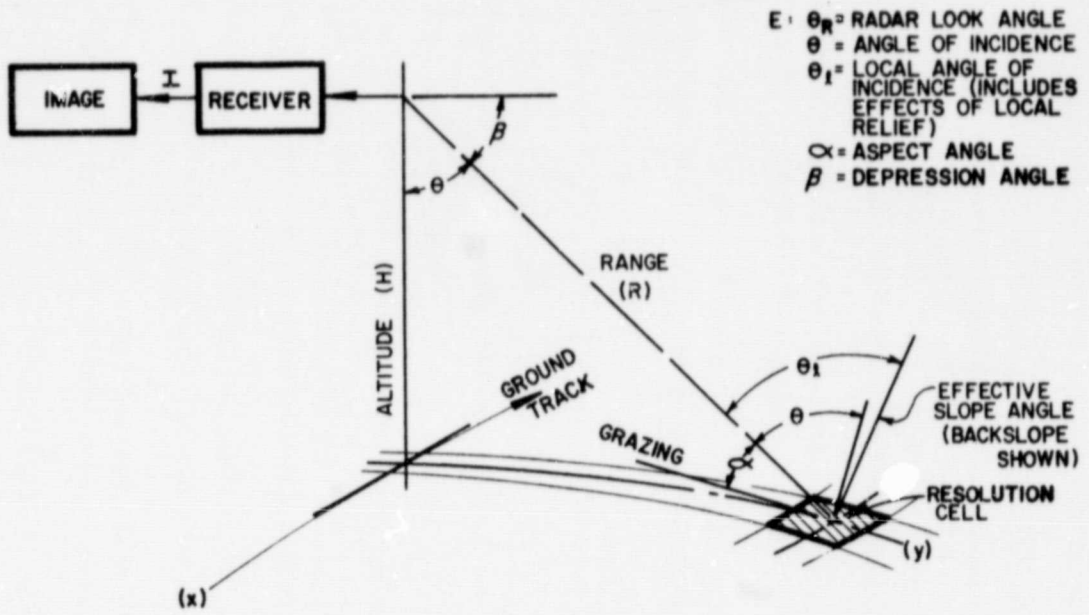

Figure 6: Geometry of Imaging Radar

strength of the return diminishes rapidly as the angle of incidence is increased. An extremely rough surface in relation to the radar wavelength is shown to have a backscatter versus local angle of incidence trend which is almost a horizontal line, consistent with the concept of producing a relatively strong return in any direction. In addition, the backscatter versus local angle of incidence trends are shown for two intermediate surfaces. As might be expected, the slightly rough surface exhibits a more specular trend whereas the moderately rough one exhibits a more uniform trend.

The scale of roughness in terms of the wavelength of the incident radiation is what is important. A given surface may appear almost smooth at sufficiently low frequencies (i.e., at long wavelengths) and thus exhibit nearly specular

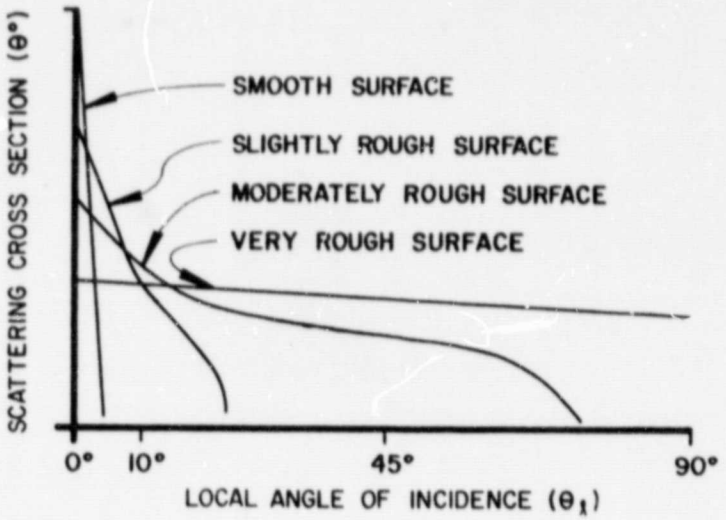

APPROXIMATE BACKSCATTERING RESPONSE OF ROUGH SURFACES (ROUGHNESS RELATIVE TO THE TRANSMISSION WAVELENGTH IS INDICATED)

Figure 7: Backscatter Trends

reflection. As the frequency is increased (i.e., as wavelengths become shorter), the same surface will appear progressively rougher until it becomes extremely rough and thus exhibits nearly uniform backscatter [14]. The scale of roughness of a surface in relation to the radar frequency, within the limitations of this simplistic, general discussion, defines the general shape of the backscatter curve.

The complex permittivity, for all practical purposes, sets the level and range of the backscatter curve. The complex permittivity is an electromagnetic description of the surface material and it controls the amplitude and phase of the reflected and refracted waves. The complex permittivity depends upon many physical properties of the material. A moderately rough surface (in relation to the radar wavelength) with a large percentage of water would exhibit a

backscatter trend like the one shown in Figure 7. A similar surface that is relatively dry would exhibit a similar trend, but it would be biased below the wet one.

Backscatter trends in imagery can be summarized in general terms as follows. For a given scale of roughness and complex permittivity, the smaller the local angle of incidence the higher the backscatter and thus the brighter the image tone.

As can be seen in Figure 5, backscatter data are used in the simulation programs to model the reflectivity for each terrain cover type present in a data base. It is these backscatter data which represent the interaction between the transmitted electromagnetic energy and each cover type. They account for important properties both of the ground such as the complex permittivity and surface roughness, and of the radar, such as the transmission frequency and polarization. Empirical backscatter data such as those published by Ulaby [15] or Cosgriff et al. [16] are used where possible. Theoretical backscatter models such as Fung and Chan [17] or Hevenor [18] are often important sources of data.

6.2 DATA BASE

The data base is a digital replica of the ground and is the input mechanism for getting the geologic terrain model into the computer simulation programs. This digital representation symbolizes the ground and its surface materials (i.e., its cover) in a grid matrix having at least four dimensions, two for the horizontal location of each point, one for its elevation, and at least one for its cover type.

Digital terrain data (i.e., digital representations of terrain elevations) are used as the spatial information in a data base. These data represent either actual terrain elevations or mathematical models of terrain elevations such as the geologic terrain models discussed in Chapter 5. Figure 4 is a three-dimensional plot of a mathematical model used as a data base (it is one of the 1st order geologic models presented in Section 5.2) and Figure 8 is a similar plot of actual terrain data.

The data plotted in Figure 4 represent the geologic terrain model of a simple anticline and syncline feature. The mathematical representation of the geologic feature has been embedded in a square matrix symbolizing a square region of ground. This matrix contains 512 X 512 elements. Each element symbolically represents a square region of 15.625 m on the ground (i.e., an area of 244.14 sq m). The complete ma-

trix, then, represents a square region of 64 sq km, each side being 8 km long. Each entry in the matrix specifies the terrain elevation at a point on the ground. The maximum elevation, along the crest line, was set at 100 m. In this way, data bases have been created from each of the geologic terrain models discussed in Section 5.

The geologic terrain model is illustrated in Figure 4 in a three-dimensional plot. The anticline is readily identified as the structure having the long, smooth nose and infacing escarpments, whereas the syncline has an abrupt scarplike nose and outfacing escarpments. Slope angles have been set for these features from a plunge angle of 8 degrees (on the nose of the anticline), to approximately 60 degrees for the very steep escarpments, to approximately 23 degrees on the more gradual slopes.

The data plotted in Figure 8 are a subset taken from a NCIC (National Cartographic Information Center) digital terrain tape[9] and represent the elevation surface for a region in the mountains of Tennessee. These data were produced by the Defense Mapping Agency Topographic Center (DMATC) from the 1:250,000-scale series of USGS (U. S. Geological Survey) maps, specifically from NJ 16-12E. These data consist of an array of 512 X 512 points or pixels (picture elements). Each pixel represents a ground spot size of 91.44 m X 91.44 m. The scene therefore portrays a portion of the ground representing 2192 sq km (i.e., a square of 46.8 km on each side) in the southern Appalachian basin region of Tennesee. Two types of terrain are present in this region, maturely dissected mountains and elongated mountain slopes.

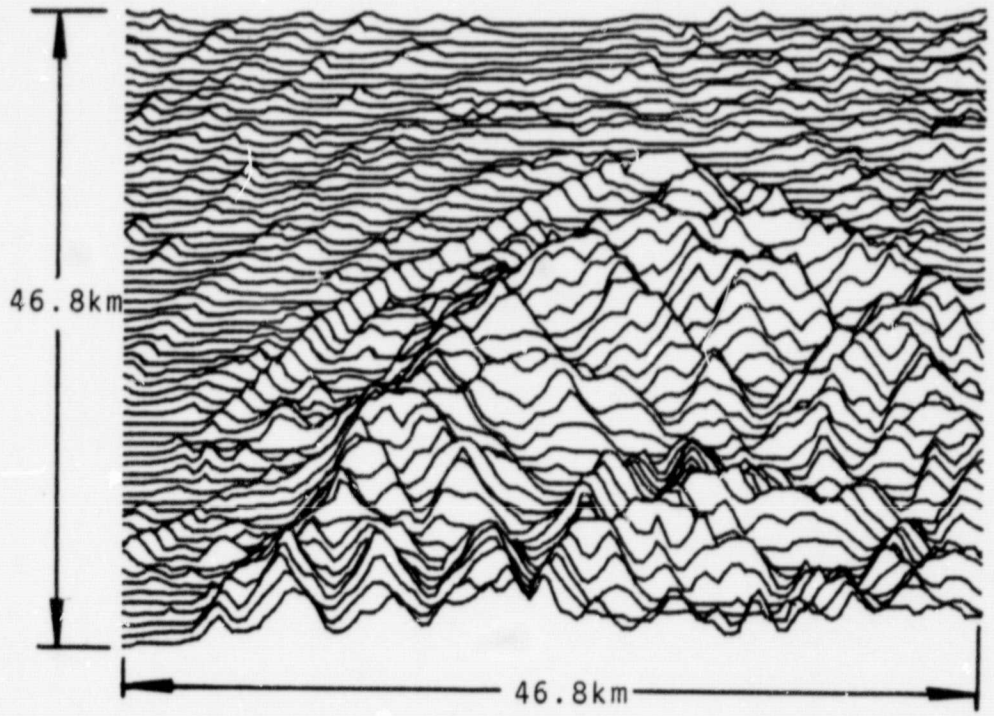

Figure 8: Plot of Actual Terrain

6.3 SIMULATION MODEL TRANSFER FUNCTION

For simulation purposes, a radar is modeled as the system illustrated in Figure 9. As can be seen from the figure, the transfer function can be symbolically written as

$$D = \gamma \log [f(h \star P_r)] + K \qquad (6.1)$$

where D symbolizes the density of silver grains in the film of an image, γ is the film gamma (i.e., the slope of the D vs logE curve), and K is a constant depending upon the development processing as discussed by Goodman [19]. This result arises from convolving the system's blurring function (h) with the input power (P_r)

$$P'_r = h*(\bar{P}_r \cdot N_0) = h*P_r \qquad (6.2)$$

where $\bar{P}_r$ is the return power predicted by the radar equation (Moore [20]), and the noise, N_0, is a random variable having the appropriate probability density function. The system's blurring function accounts for the various antenna and pulse length effects.

This result is next scaled in amplitude according to the characteristics of the system being modeled, thereby producing an intensity (I) as

$$I = f(P'_r) \qquad (6.3)$$

which is incident upon film and recorded as a density D

$$D = \gamma \log(I) + K \qquad (6.4)$$

which is identical with (6.1).

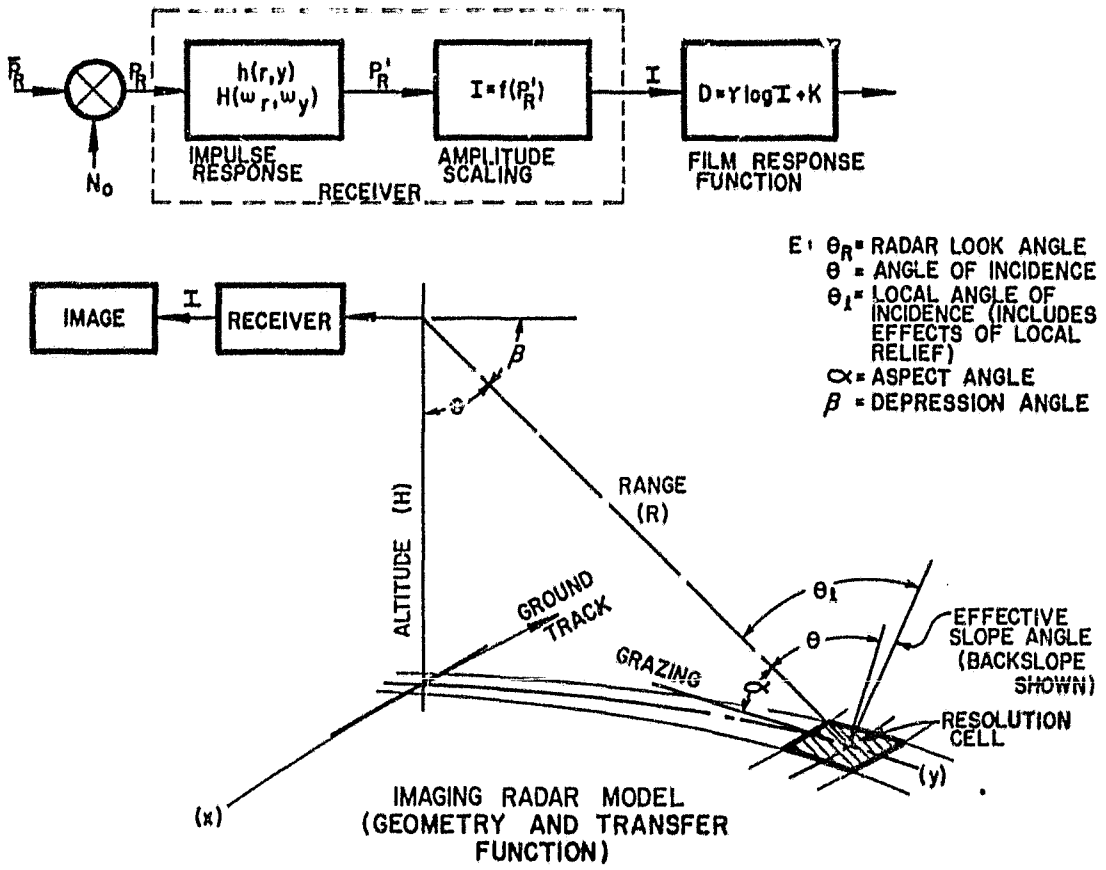

Figure 9: Simulation Model Transfer Function

6.4 POWER-MAP IMAGE

The power-map image represents, in image form, the power density being reradiated from each point on the ground back in the direction of the radar antenna. The power map has no actual radar analogue, but it is an important interim result because it provides diagnostic evidence of backscatter effects without the perturbations of added geometric or propagation distortions.

6.5 SLANT-RANGE IMAGE

The slant-range image can be considered as either an interim product or a final image. The simulated slant-range image is directly analogous to an actual slant-range image. It embodies all the geometric distortions inherent in radar. The energy being returned to the radar has been sorted and rearranged by time, or distance, in accordance with the geometry of the radar and the location of the individual resolution cell. Geometric distortions such as foreshortening, layover, and shadow all are incorporated and properly displayed. In essence, the slant-range image represents a mapping from the spatial coordinates (x,y,z) of the ground into the image coordinates (r,y), range and azimuth, respectively.

As is illustrated in Figure 5, two different versions of the slant-range image can be generated, with and without noise. In either case, the resolution, and in the noisy case the fading, can be processed in either the spatial domain or the spatial frequency domain. Processing of resolution and fading in the spatial domain involves more simplifying assumptions and is thus less precise than processing in the spatial frequency domain. As the programs are now structured, the spatial domain processing is faster and thus less expensive, and is generally used where simple statistical models are sufficient. Processing in the spatial frequency domain is generally done where higher order statistics are required.

6.6 GROUND-RANGE IMAGE

The simulated ground-range image is directly analogous to an actual radar ground-range image. It represents a nonlinear mapping from the slant-range image space back into a ground-range (x,y) image space. All the distortions due to elevation (i.e., relief) mapped into the slant-range image are accentuated when the mapping to the ground-range image is done. This mapping preserves the geometric fidelity or orthographic arrangement of features on a level or planar surface such as the mean ground surface. The location of any point above or below the flat surface is distorted in the slant-range image and is further distorted in the ground-range image.

Chapter 7

RESULTS

Families of computer-generated radar images have been prepared via the simulation progams discussed in Chapter 6 for each of the 1st order geologic terrain models presented in Chapter 5. Each family of images contains representative variations of the parameters in Table 1. Each image of a family portrays a specific geologic terrain model as it appears to a specific radar (i.e., a system representing one set of the parameters).

Figure 10 illustrates the value of using geologic terrain models and computer simulation. The figure contains a sample set of simulated radar images prepared from the breached anticline/syncline geologic terrain model discussed in Chapter 5 (Figure 4). This sample set of images represents the scene imaged by a radar having a specific operating configuration (i.e., frequency, polarization, resolution, etc.), from Table 1 held constant. The only variable in the figure is the angle of incidence.

All of the simulated radar images in Figure 10 are ground-range images. These images simulate the results of an X-band radar (i.e., one operating in the region 5 - 12 GHz) being flown across the top of each image from left to right at an altitude of 800 km. The radar operates symbolically with HH polarization (i.e., horizontal transmit and horizontal receive) and the antenna functions over the terrain formed from the geologic terrain model while attaining the angle of incidence listed in the figure.

The radar images in Figure 10 illustrate how landforms change appearance both with changing angle of incidence and with changing look direction. Presented in the figure are radar images simulated for 11 discrete angles of incidence in the angular range from 23 to 85 degrees (angle of incidence is illustrated in Figure 6). Note how vividly this presentation illustrates the changes. To a large extent the changes are so vivid because they are illustrated across the complete angular range for a single, simple, stark feature without the complications introduced by geologic noise (i.e., landscape cover variations, weathering effects, etc.). To a lesser degree, the impact of changing angle of incidence arises because the feature contained in the scene is isolated. This simple illustration demonstrates the

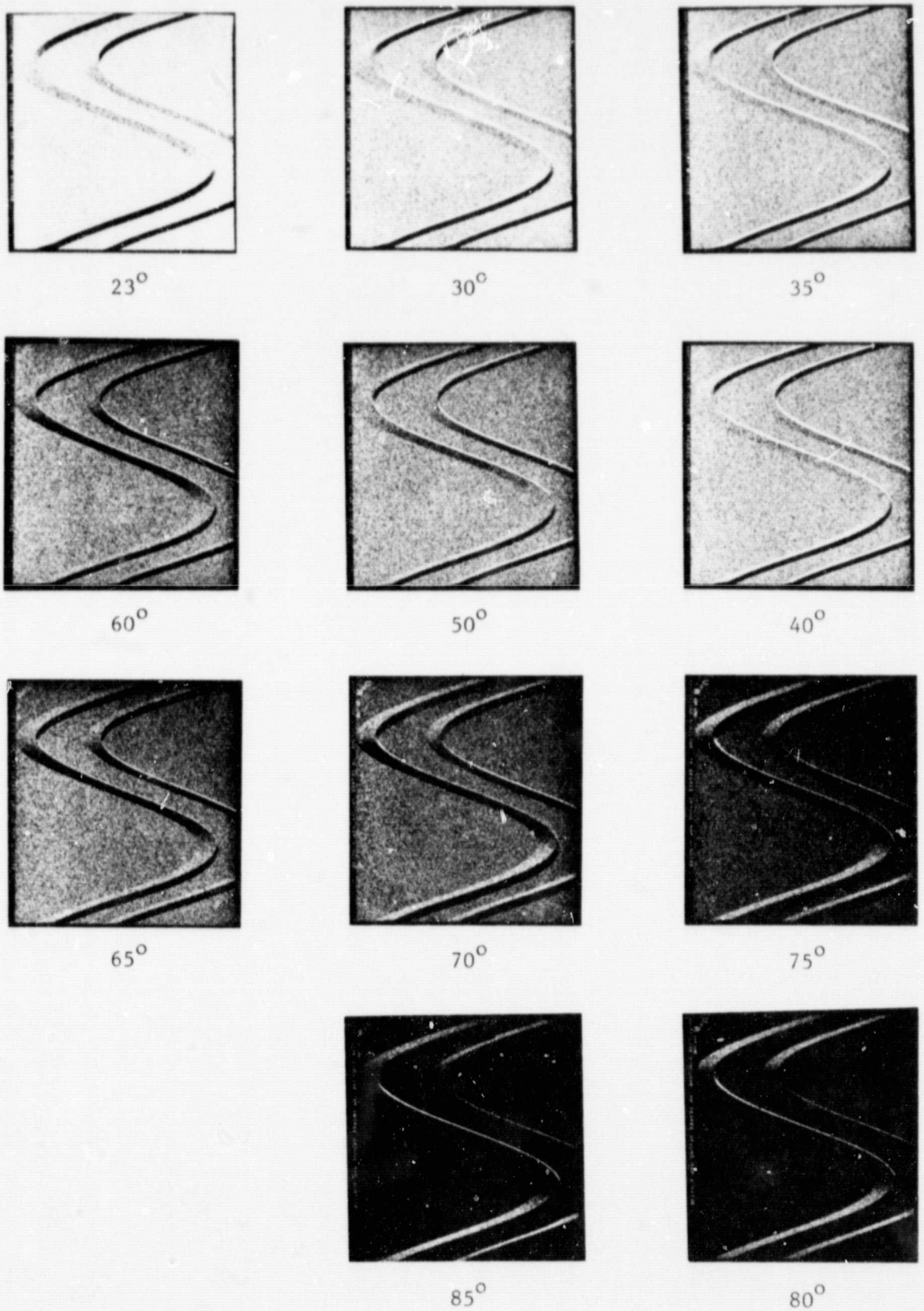

Figure 10: Example Simulated Radar Images

value and utility of using simulated radar images formed from geologic terrain models: parametric trade-off analyses can be made with all variables held constant (system, platform, and terrain - Table 1) except the specific ones being evaluated and the resultant variations are immediately evident.

The two detailed evaluations of radar images simulated from 1st order terrain models provided in Appendices A and B exemplify how much detailed and useful information can be obtained from the simulated images. Simulating radar images from 1st order geologic terrain models is a powerful tool for discerning the relationships among system, platform, and terrain variables as expressed visually in the product actually employed by the end user, the radar image.

Figure 11 illustrates a sample set of radar images simulated from the list of basic linear landforms (cf. Table 1). These images were produced for the same simulation scenario as that described for Figure 10: X-band, HH polarization, 800 km altitude, and flying to the right across the top of the image. The difference in this figure is that the geologic terrain model is changed from scene to scene while the angle of incidence is held at a constant 50 degrees (note that changing look direction is incorporated in the images by the way the linear landforms are oriented in relation to the radar). This figure, then, illustrates how a constant radar configuration would portray linear features as the geometry of the feature is changed.

Appendix C is a short paper [21] illustrating the application of radar simulation to actual terrain instead of 1st order terrain models. The terrain used is that plotted in Figure 8. The paper shows that the simulation computer programs produce images which are very acceptable as radar images, and thus demonstrates the significance of using radar image simulation as the principal research tool in this study: results obtained are applicable to actual imaging radars.

These sample preliminary results show that digital image simulation and geologic terrain modeling afford important advances for this kind of study. They provide cost-effective methods for evaluating both terrain variations and radar parameter changes, for predicting results, and for defining the optimum sensor parameters for geologic applications, as illustrated in Appendix A. In addition, they provide ways for interpreting image distortions, and for evaluating separate image effects such as backscatter versus layover, foreshortening, etc., as illustrated in Appendix B. Further, preliminary analyses of an optimum angle of incidence for geologic studies indicates the best angle is dependent upon the terrain type being studied. As sug-

Foreslope 20°
Backslope 10°

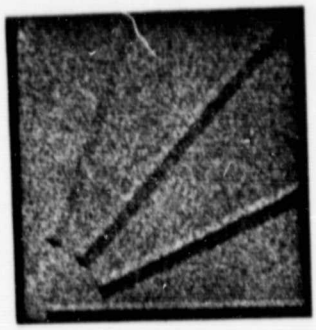

Foreslope 20°
Backslope 20°

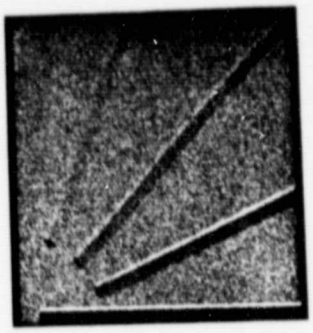

Foreslope 30°
Backslope 20°

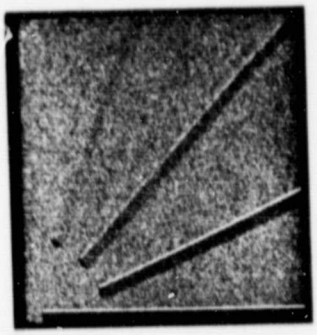

Foreslope 40°
Backslope 20°

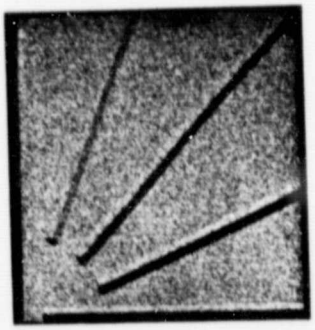

Foreslope 20°
Backslope 30°

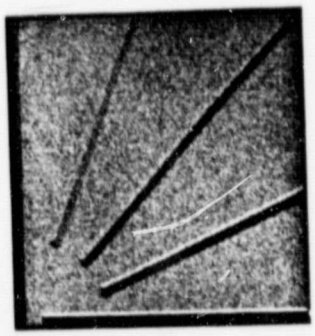

Foreslope 30°
Backslope 30°

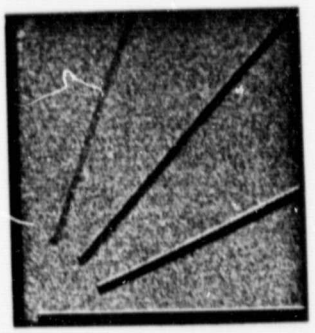

Foreslope 40°
Backslope 30°

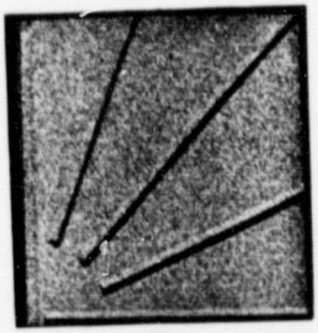

Foreslope 20°
Backslope 40°

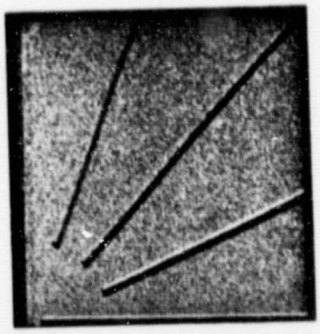

Foreslope 30°
Backslope 40°

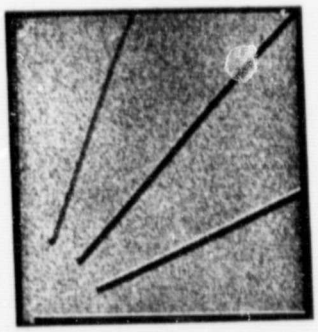

Foreslope 40°
Backslope 40°

Figure 11: Examples Simulated Radar Images of Linear Landforms

gested in Appendix C, for the mix of terrain types modeled thus far the best configuration appears to be a system having at least two angles of incidence, one large and one small. This configuration, however, is not definitive. It represents conclusions reached after preliminary analysis of a very limited number of terrain environments (i.e., cover and relief).

PART III

STUDIES PERFORMED AT THE UNIVERSITY OF KANSAS

Chapter 8

PROLOGUE

The application of imaging radar to geologic mapping has provided illuminating results [22]. Several successful mapping programs have been conducted using aircraft sensor platforms, but only recently, with the flight of the SEASAT-A satellite, has a spacecraft sensor platform been available for collecting radar imagery. Though the system parameters of the SEASAT-A were optimized for sensing the oceans, its synthetic aperture radar (SAR) has provided impressive synoptic views of the earth's surface which have subsequently been used for geologic mapping. However, the experience with the SEASAT-A SAR has revealed two research problems whose solutions would greatly enhance the utility of future space missions for geolgic mapping.

One research problem is the quantitative determination of the tradeoffs between various sensor parameters and the quantity and quality of the extractable geologic data. Obviously no one set of sensor parameters will provide optimum SAR images for mapping all geologic features of interest simply because of their diversity. It is important therefore to establish how various sensor configurations affect the mapping of different geologic features. From the results of such a tradeoff analysis the SAR system design can be tailored to produce the best images for extracting geologic features of special interest. For example, radar parameters such as angle of incidence and averaging of independent samples are closely tied to image appearance.

The other research problem is the development of automated techniques of image analysis. Though the synoptic view of the earth's surface is one of the spacecraft sensor platform's major advantages, it also presents significant problems for data reduction. That is, satellite SAR images which cover large surface areas now must be analyzed manually. Recent advances in digital image processing technology afford the possibility of machine-aided geologic analysis of SAR imagery. Because of the diversity of the image manifestations of geologic features, computer analysis is not expected to replace human interpretation of SAR imagery; rather the computer should be used to ease the required analysis tasks. This report describes how automated texture analysis can be used to separate various types of macrotexture (repetitive spatial patterns, many resolution elements

in size) which are indicative of different geologic features. Once identified, pertinent statistics (e.g., preferred directions of linears) would be available to the human interpreter.

Though the two research problems seem disjoint they are actually closely related. The investigation of each requires four elements for success:

Analysis
(1) Radar system response modeling for rough terrain.
(2) Radar image characterization (e.g., 1st and 2nd order statistics) as a function of geologic features.
(3) Terrain modeling for macro- and microstructures.

Synthesis
(4) Implementation of radar and terrain models to synthesize images. Analysis of images to determine useful geologic information.

Clearly, both problems require SAR modeling for rough terrain. Because of the many complex interactions between the sensing of the image and the production of geologic maps, the only feasible technique for establishing the desired tradeoffs is to model accurately the SAR response to representative types of terrain and then to evaluate quantitatively the quality of the extractable geologic data as the system configuration is varied. The automated data analysis problem is aided by the same modeling. All successful image-processing algorithms require a "world model" to describe the statistical characteristics of the data to be processed; thus, for data extraction, modeling and simulation are also required.

The second key element is the investigation of radar image properties (e.g., 1st and 2nd order statistics or texture) as a function of geologic features or vegetation cover. Signal-to-noise ratio and texture are two image properties which are strongly linked to the types of image surfaces. Quantitative relationships between terrain paramaters and image properties can be established by either theoretical systems analysis or sensor simulation. If the relationships between image characteristics and the image's geologic mapping potential could be identified, it would be possible to establish how the sensor parameters affect the geologic mapping potential of SAR images. Further, if this cause and effect mechanism were identified, it would provide a basis for using measured SAR image properties to indicate the presence or absence of geologic features of interest. The establishment of the correlation between SAR image characteristics and geologic features is thus important for system optimization and SAR data reduction.

Third, to support the first two components of the research the modeling of surface features and their spatial arrangement (e.g., a surface feature would be a ridge and a spatial arrangement of ridges would form a mountain range) is essential. This modeling effort would provide an understanding of what the radar system is attempting to sense. Clearly these models describing the geologic features are necessary for the development of automated data reduction algorithms because they are the phenomena which are to be estimated (or extracted) from the imagery. Both random and deterministic models are useful to describe surface features. Though structures of size on the order of a wavelength are best modeled as manifestations of random processes, larger structures may sometimes be modeled as either stochastic or deterministic; both approaches are being pursued by the authors.

This report describes the work that has been accomplished in the four areas outlined, specifically (1) texture characteristics (2nd order statistics) as a function of different geologic feature orientations, (2) radar system models for simulation and radar image processing, (3) simple deterministic models for large-scale geologic features, and (4) generation of images given the simple terrain models and imaging radar models.

The discussion of results is preceded by a few comments on geologic feature roughness scales. The many aspects of the microwave-terrain interaction are not reviewed as that topic is treated in many reports and texts (e.g., Daily et al. [22], Evans [23], Reeves et al. [24], and others).

Chapter 9

SAR IMAGING OF ROUGH TERRAIN SURFACES

We differentiate among three scales of geologic features: (1) those of size on the order of the wavelength of illumination (lithologic), (2) those on the order of a resolution cell (using the SEASAT-A SAR as an example), and (3) those on the order of many resolution cells (landforms). Radar response to category 1 is discussed in a nontheoretical treatment by Daily et al. [22]. Our research is aimed at categories 2 and 3. For example, we base our approach to the automated data reduction problem on the observation that large-scale repetitve geologic features give rise to repetitive patterns in the associated radar imagery. Such patterns can be viewed as texture features in SAR imagery. As we show in Section 10.1, available texture discrimination algorithms can be applied to radar scenes to separate scenes on the basis of 2nd order statistics.

Microwave propagation effects due to the large-scale terrain elevation variations such as shadow, foreshortening, layover, and local angle of incidence effects account for the vivid depiction of natural terrain that SAR can produce. These important factors have been incorporated in the terrain modeling and radar modeling. These factors are intimately linked to texture within radar imagery; we show that different orientations of landforms (and their consequent different shadow patterns) are separable by texture measures.

Chapter 10

STATISTICAL CHARACTERISTICS OF SAR IMAGERY

We have proposed to study both 1st and 2nd order statistics within radar images and to relate them to landforms, structural features, radar look direction, angle of incidence, and other factors. First order statistics are point statistics, whereas 2nd order statistics can measure neighboring point relationships.

Though for flat terrain the speckle statistics (μ,σ) have been known theoretically for many years (since the late 1800's) as interference phenomena, the point statistics have not been treated theoretically for particular random process models of terrain in conjunction with deterministic sensor models. We have conducted a preliminary experiment on the texture characteristics (2nd order statistics) of regions within SEASAT-A SAR images. The results show potential for a texture approach to automated data reduction. First order statistics investigations for SAR images of rough terrain models represent on-going work.

10.1 A PRELIMINARY TEXTURE ANALYSIS OF RADAR IMAGERY

Spectral, textural, temporal and contextual features are four important pattern elements used in human interpretation of image data. Spectral features describe the average band to band tonal variations in a multi-band image set whereas textural features describe the spatial distribution of tonal values within a band. Contextual features contain information about the relative arrangement of image segments belonging to different categories, and temporal features describe changes in image attributes as a function of time. When small image areas within, say, a synthetic aperture radar (SAR) image are processed independently on a computer, only the tonal and textural features are available to the machine.

In many of the automated procedures for processing radar image data from small areas, such as in crop classification studies, only the average tonal values are used for developing a classification algorithm. Textural features are generally ignored on the basis that the poor resolution of radar imagery does not provide meaningful textural information

for such applications. However, for many other applications such as the identification of large-scale geologic formations, land use patterns, etc., the resolution is more than adequate to provide textural information. Indeed, in these applications, texture is probably the most important image feature. We describe a procedure for obtaining numerical descriptors for characterizing the textural properties of segments of radar images.

The textural feature extraction algorithm we describe has been widely used (Rosenfeld and Troy [25], Haralick and Anderson [26], Sutton and Hall [27], Haralick et al. [28]) for analyzing a variety of photographic images. The procedure is based on the assumption that the texture information in an image block "I" is contained in the overall or "average" spatial relationship which the gray tones in the image "I" have to one another. This relationship can be characterized by a set of gray level co-occurrence (GLC) matrices. We describe a procedure for computing a set of GLC matrices for a given image block and define a set of numerical textural descriptors (features) that can be extracted from the GLC matrices. These textural features can be used for automated analysis and classification of blocks of radar imagery.

Segments of digitally correlated SEASAT-A SAR imagery have been processed using the textural features. The results are presented to show that these features can be used to classify large-scale geologic formations. Because the areal characteristics of texture carry so much information, we conclude that it is important to use textural features in automated radar image processing schemes except in appliations where the poor resolution of the imagery does not provide meaningful textural information.

10.2 TEXTURAL FEATURES

Texture is one of the important characteristics used in image analysis. Image texture may be viewed as a global pattern arising from a deterministic or random repetition of local subpatterns or primitives. The structure resulting from this repetition is very useful for discriminating among the contents of the image of a complex scene. A number of approaches have been suggested for extracting features that will discriminate between different textures (Rosenfeld and Troy [25], Haralick and Anderson [26], Sutton and Hall [27], Haralick et al. [28], Galloway [29]). Of these approaches, textural features derived from gray level co-occurrence matrices (GLCM) have been found to be the most useful for analyzing the contents of a variety of imagery in remote sensing, biomedical, and other applications (Shanmugam and Haralick [30], Haralick and Shanmugam [31], Kruger et

al. [32], Weszka et al. [33], Connors and Harlow [34]). The GLCM approach to texture analysis is based on the conjecture that the texture information in an image is contained in the overall or average spatial relationship among the gray tones of the image.

The 2nd order gray level co-occurrence matrix of an image is defined as follows. Let $f(x,y)$ be a rectangular digital picture defined over the domain $x \in [0,n_x)$, $y \in [0,n_y)$; $x, y \in I$. Let n_g be the number of gray levels in f. The unnormalized, 2nd order GLC matrix is a square matrix $\bar{P}$ of dimension n_g. The (i,j)-th entry in $\bar{P}$, denoted by P_{ij}, is a function of the image tonal values and a displacement vector $\bar{d} = (d_1,d_2)$. The entries P_{ij} are unnormalized counts of how many times two neighboring resolution cells which are spatially separated by $\bar{d}$ occur on the image, one with gray tone i and the other with gray tone j. That is,

$$P_{ij} = \#\left\{\left((m_1,n_1),(m_2,n_2)\right) \mid f(m_1,n_1) = i,\ f(m_2,n_2) = j,\ \text{and } (m_2,n_2) - (m_1,n_1) = \bar{d}\right\}, \tag{10.1}$$

where # denotes the number of elements in the set, and the indices m_1, m_2 and n_1, n_2 take on integer values in the intervals $(0_1, n_x),(0_1, n_y)$. The normalized GLC matrix P with entries P_{ij} is obtained from $\bar{P}$ by dividing each entry in $\bar{P}$ by the total number of paired occurrences. The definition of 2nd order GLC matrices can be extended to include 3rd and higher order GLC matrices. Though higher order GLC matrices may be important in some applications, much of the recent work in texture analysis has been based on 2nd order GLC matrices.

The 2nd order GLC matrices are computed for various values of the displacement vector $\bar{d}$, and features derived from the GLC matrices are used for classifying the contents of an image.

Some of the commonly used textural features derived from the GLC matrix are:

1) Uniformity (sum of squares) : $\sum_{ij} p_{ij}^2$ (10.2a)

2) Contrast : $\sum_i \sum_j (i-j)^2 p_{ij}$ (10.2b)

3) Correlation : $\sum_i \sum_j \frac{(i-\mu_x)(j-\mu_y) p_{ij}}{\sigma_x \sigma_y}$ (10.2c)

4) Entropy : $\sum_i \sum_j p_{ij} \log p_{ij}$ (10.2d)

5) Inverse difference moment : $$\sum_{\substack{i \\ i \neq j}} \sum_{j} (p_{ij})^{\rho} / |i-j|^{\upsilon} \qquad (10.2e)$$

6) Maximum Probability : $$\max_{i,j} p_{ij} \qquad (10.2f)$$

For a variety of imagery (aerial, micrographic, and x-ray) the relationship among these textural features, their values, and what they represent in terms of visual perception of texture are reasonably well understood. Using features of the form given above, Haralick and Shanmugam (Haralick et al. [28], Galloway [29], Shanmugam and Haralick [30]) were able to classify a variety of images with better than 85% classification accuracy.

Given the past success of image analysis using textural features on Landsat and other imagery, it seems reasonable to expect similar success in the case of textural features for analyzing radar images. Such has not been the case until now for several reasons, mainly the limited availability of radar images in digital form and the use of human interpretation of radar images. With the increasing need for automated procedures to analyze large volumes of radar data in digital form, textural features are expected to have an important role in radar image analysis. In the next section is an example which shows that textural features can be used for classifying segments of radar images corresponding to different geologic formations.

10.3 RESULTS

The textural features described in the preceding section were used to analyze segments of SEASAT-A SAR imagery over Tennessee (Figure 12). Four areas within this image were processed using the textural features described in the preceding section. All four areas are in the vicinity of the Pine Mountain thrust and are underlain by the same rock sequence: Pennsylvanian shales, sandstones, and siltstones. However, their surface manifestations are different because of the nature of the stress to which they have been subjected, orientation and nature of the fractures, and erosion. Six subimages were chosen from the four areas of analysis. Examples of the subimages which were analyzed in detail using textural features are shown in Figure 13.

The co-occurrence matrices and textural features were computed for each of the 24 samples. The sample image

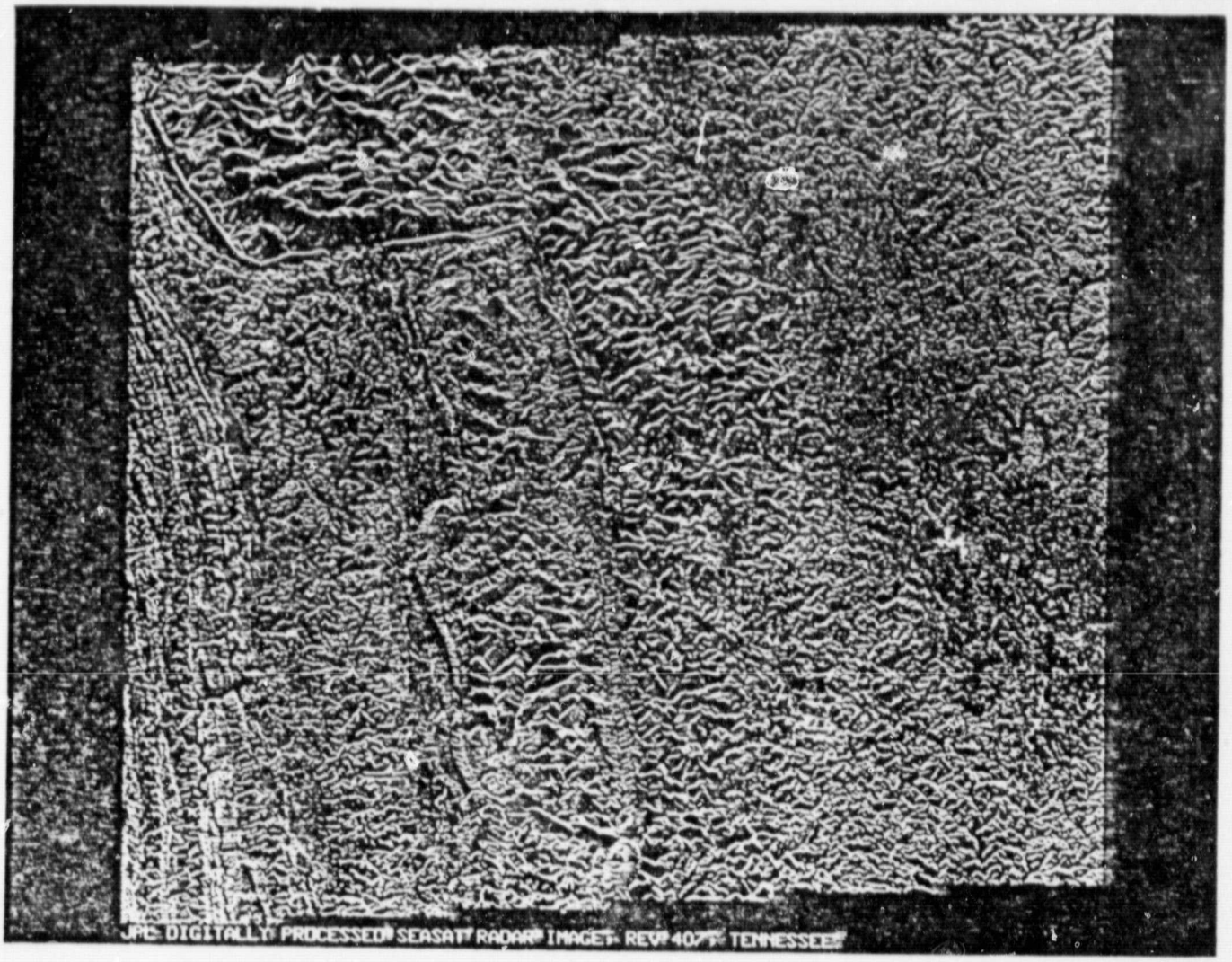

Figure 12: Original SEASAT-SAR Image

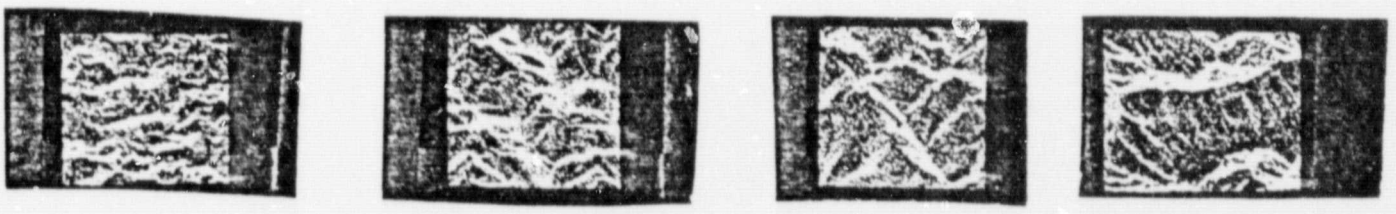

Set 1 Set 2 Set 3 Set 4

Figure 13: Typical Subimages for Four Image Categories

blocks were of size 200 X 200 and the image blocks were equal-probability quantized into 32 levels. Co-occurrence matrices were computed for $|\overline{d}|$ =1, 2, 4, and 8, and angle of $\overline{d}$ =0, 45, 90, and 135 degrees. The co-occurrence matrices for the four angles were averaged and the uniformity, contrast, maximum probability, and inverse difference moment features were computed from the average co-occurrence matrices. A total of 16 features were used to characterize the textural properties of each image block.

Scatter diagrams of the numerical values of pairs of textural features are shown in Figure 14, and plots of average feature values as a function of $|\overline{d}|$ are shown in Figure 15. The results displayed in Figures 14 and 15 clearly demonstrate the usefulness of textural features for classifying radar image segments. Though the image blocks have nearly the same mean and variance, the textural features separate the image categories very well.

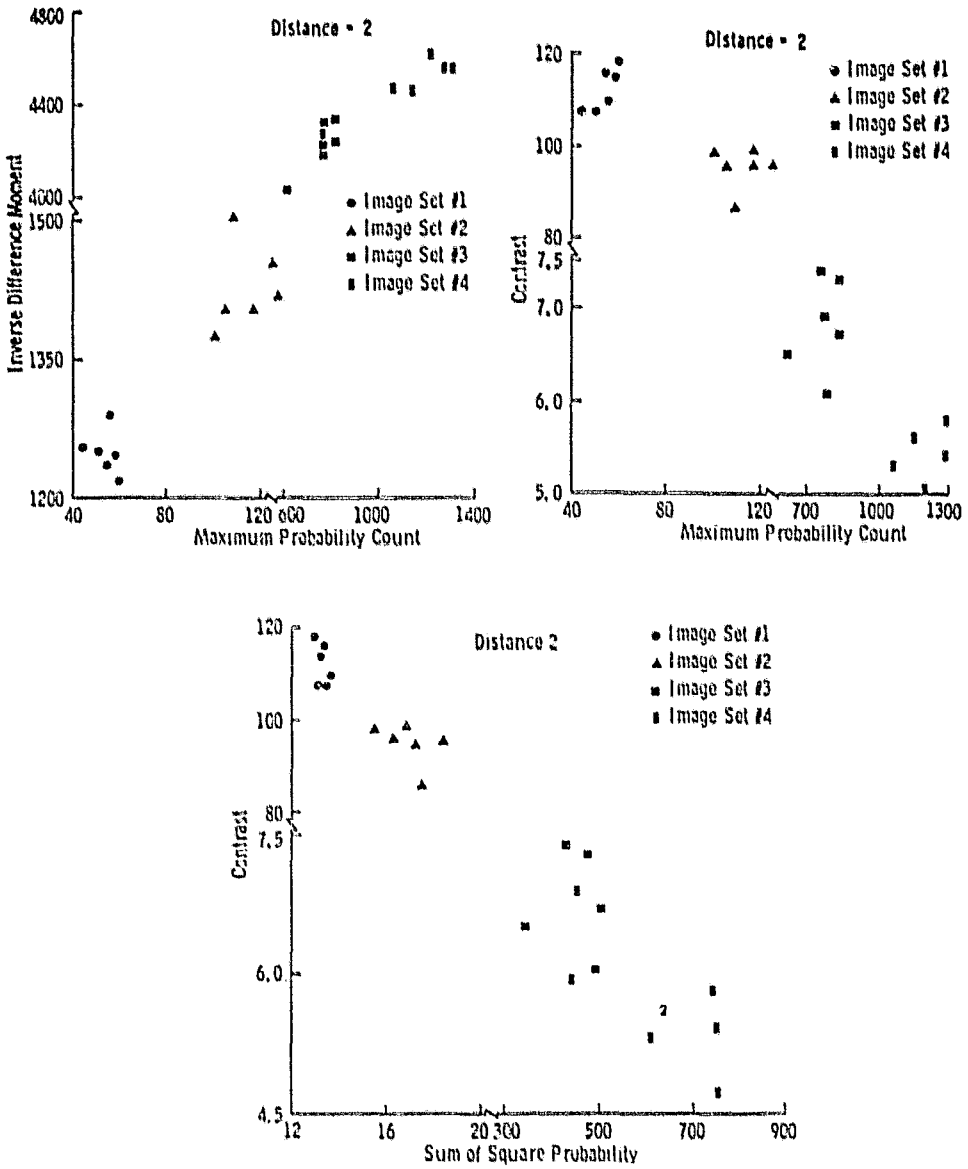

Figure 14: Scatter Diagram of Textural Features for Four Image Categories

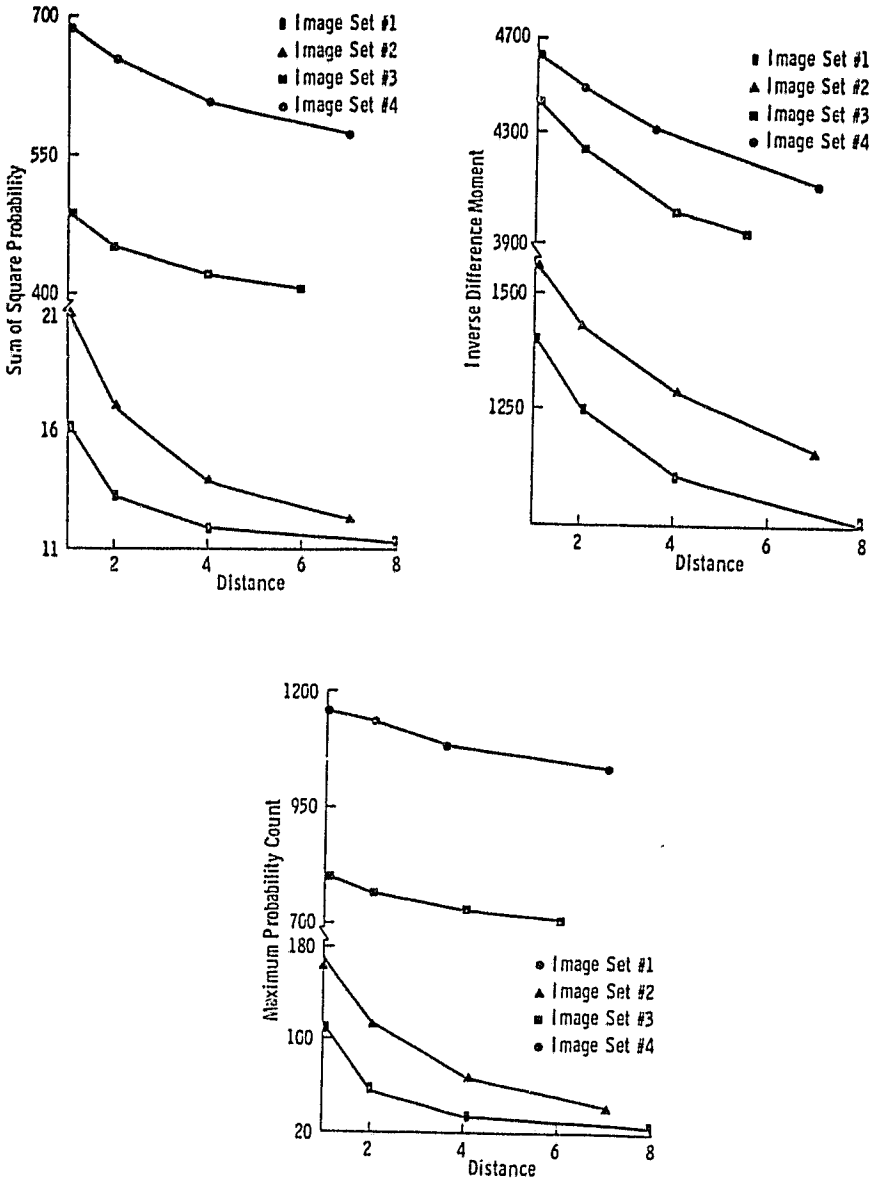

Figure 15: Feature Values Versus Distance

10.4 CONCLUSIONS

A set of features for characterizing the textural properties of segments of radar imagery is presented. The textural features were computed and used for identifying some simple geologic formations from radar imagery to demonstrate the potential usefulness of textural features for radar image classification.

Chapter 11

RADAR SYSTEM MODELING AND RADAR IMAGE SIMULATION

Experience of the image simulation group at the University of Kansas Remote Sensing Laboratory has led to two basic approaches in simulation: (1) calculate a geometry-corrected (range perspective) map of average return powers (real valued), incorporate signal fading, and subsequently perform smoothing operations on intensity data (Holtzman et al. [35,36]); (2) calculate a geometry-corrected complex map, and perform resolution degradation and averaging of looks independently on the complex data. In the latter method, additional looks can be obtained only by addition of images on an intensity basis; degradation of resolution on coherent data does not add to the number of looks (the random walk in space analysis is still appropriate).

Radar system modeling for ideal (isotropically reflecting point) targets is the standard SAR analysis (Brown [37], Harger [38]). Modeling for nonideal targets and collections of such targets according to random elevation models has not been accomplished; our efforts in the on-going phase of this research address these aspects of the SAR-geology interaction.

Several studies of radar image simulation have been reported (Mitchell [39], Bell [40], Beckner and Crow [41], Holtzman et al. [35,42,36,43]). Because of the numerous aspects involved in the implied geometry problems, data base construction, and implementation complexities, we forego a lengthy discussion here. However, we have found it necessary to derive processing algorithms to operate on the (real) output of the simulation software for system studies (resolution, looks). One incoherent filter which is useful for treating image (intensity or amplitude) data is presented next. Processing on the complex outputs of our simulations is based on well known techniques (Zelenka [44], Porcello et al. [45]).

11.1 COHERENT AND INCOHERENT PROCESSING FOR RADAR

Coherent processing will be defined as any operation on amplitude and phase of a radar signal; incoherent processing will be defined as operations on amplitudes only or on

power only. Thus, azimuth focusing and range compression are coherent operations; signal processing to improve the signal-to-noise ratio involves summing intensity images (incoherent processing).

The simulations presented in this report are not generated from a simulated signal film (which would need to be filtered in azimuth and range to produce a radar hologram). Rather, the complex radar image is calculated directly. For each facet in the data base (the facet size is dictated by the resolution of the data base) the angle of incidence, range, local angle of incidence and antenna weighting are computed and subsequently used in the radar equation (Moore [20]) to predict the average return power at the antenna terminals. This value of $\bar{P}_r$ is used to calculate the amplitude of the quadrature voltage components as shown in Figure 16. When this operation is completed for the entire data base the complex radar image is available for either coherent or incoherent processing. (Implicit in the calculation of $\bar{P}_r$ are the geometry calculations to incorporate shadow, layover, and foreshortening.)

The image is defined as the sum of the squares of the voltages out of the detector

$$V_D(t_0) = [(V_I(t)*h(t)|)^2 + (V_Q(t)*h(t)|)^2] = P_0(t_0) \qquad (11.1)$$
$$t=t_0 \qquad\qquad t=t_0$$

This value at t_0 corresponds to some image location x_0, y_0. Only incoherent processing can be done on $V_D(t_0)$. Coherent processing can be carried out prior to the detector.

A fixed amount of information is available in $V_I(t)$ and $V_Q(t)$. It is well-known that from this base of information many different SAR images can be formed, i.e., there is more than one processing route and some are more suited than others to various earth resource applications. Given the complex radar image I(t), i.e.,

$$I(t) = V_I(t)*h(t) + jV_Q(t)*h(t) = v_2(t) \qquad (11.2)$$

one can determine the image spectrum $I(w) = F[I(t)]$. If this image spectrum is subdivided and if intensity images are made from the inverse transformed subdivisions, the resultant intensity images can be added on an intensity basis to produce a radar image of the same scene which has poorer resolution, but an improved signal-to-noise ratio (Zelenka [44], Porcello et al. [45], Goodman [19]). Thus, resolution can in a sense be traded for signal-to-noise improvement. If only one of the images from the subdivided

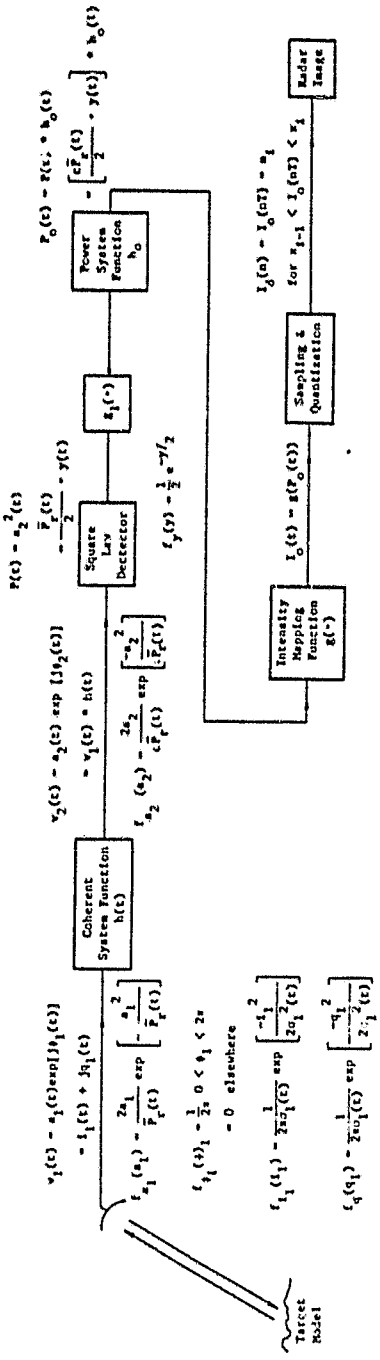

Figure 16: Radar System Block Diagram for Diffuse Scatterers

spectrum is examined, its resolution will be poor, and no improvement in signal-to-noise ratio will have been obtained.

If one assumes digital image processing (as is the case here), the image spectrum is obtained from the image by means of a discrete Fourier transform; the original image is padded to twice the original dimensions to avoid circular convolution effects (e.g., if the original image is 512 by 512 samples, its Fourier transform is a 1024 by 1024 sampling of the continuous function $I(\omega)$). Because $I(x)$ is complex, the spectrum is not symetric. If that spectrum is divided into four spectra of size 512 by 512, then, from the intensity images of the inverse transforms of the spectra an image can be made that has $N = 4$ statistics (where N is the number of independent samples) and one fourth the resolution of the original image ($\rho = \rho_{az} \times \rho_r$).

This technique is feasible when the desired value for N is small. However, it is not uncommon to specify $n > 10$, or even $N > 100$ for orbital imaging applications. In this situation the simulated radar image is produced by an incoherent degradation of an $N = 1$ image. It can be demonstrated that an incoherent filter transfer function can be found to operate on the spatial domain, to affect the operation of the multiple bandpass filtering (described in the preceding paragraph) in the frequency domain, based on Zelenka [44]. In general, it is possible to degrade the resolution and increase the number of looks (assuming the entire image bandwidth is utilized) according to the relation

$$N_{az_1} \cdot N_{r_1} = N_{az_0} \cdot N_{r_0} \cdot \frac{\rho_{az_1}}{\rho_{az_0}} \cdot \frac{\rho_{r_1}}{\rho_{r_0}} \qquad (11.3)$$

where

ρ_{az_0} = azimuth resolution before incoherent processing,

ρ_{r_0} = range resolution before incoherent processing,

ρ_{az_1} = azimuth resolution after incoherent processing,

ρ_{r_1} = range resolution after incoherent processing,

N_{az_0} = number of independent samples in azimuth before incoherent processing,

N_{r_0} = number of independent samples in range before incoherent processing,

N_{az_1} = number of independent samples in azimuth after incoherent processing,

N_{r_1} = number of independent samples in range after incoherent processing.

The image bandwidth can be subdivided more times in azimuth than range (or vice versa) to improve the number of looks in the azimuth dimension, independent of N_{r_0}. An incoherent transfer function to trade resolution for averaging has been implemented and used for results reported in Chapter 12.

11.2 DERIVATION OF AN INCOHERENT TRANSFER FUNCTION

The purpose of this development is to derive an incoherent transfer function (Goodman [19]) which performs in the spatial domain the continuous (scanning) mixed integration process described by Zelenka [44]. This procedure is commonly referred to as incoherent averaging. For the commonly needed case of large N statistics it is computationally inefficient to use the spatial frequency filtering approach to achieve the desired point statistics. The filter described simultaneously degrades resolution and achieves the needed large N statistics in one spatial domain operation by using image data (no phase data), in contrast to complex filtering in the spectral domain.

Zelenka [44] has shown an ideal linear system model for a synthetic aperture radar system as represented in Figure 17. Incoherent processing of the radar data to improve the signal-to-noise ratio is commonly implemented as seen as in Figure 18. The complex radar reflectivity s(x) is convolved with the impulse response p(x) and the data are filtered by scanning in the frequency plane. The detection on film represents square law detection and the finite frequency plane window and window velocity give rise to time averaging, the output of the averaging filter being the image Z(x). Zelenka has derived the equivalence between the scanning frequency plane mixed integrator and an incoherent transfer function $|h(x)|^2$ which operates on detected (intensity) data. The extension of this development to two dimensions is straightforward. The results state that

$$Z(x) = \frac{1}{T} \int_{-T/2}^{T/2} \int_{-\infty}^{\infty} \int_{-\infty}^{\infty} U(f_1)\, \overline{U}(f_2)\, H_p(f - \beta_t) \cdot \overline{H}_p(f_2 - \beta t)\, e^{j2\pi x(f_1 - f_2)}\, df_1\, df_2\, dt = |s(x) * p(x)|^2 * |h(x)|^2 \tag{11.4}$$

where $U(f) = F[u(x)]$ and the bar denotes conjugation. The transfer function $H(f) = F[h(x)]$ has the form of the low pass equivalent of the bandpass filters $H_p(f)$. For example, because the bandpass filters are uniformly weighted windows, i.e., $H_p(f) = \text{rect}[f/B]$, the impulse response varies as $\sin(x)/x$ for the scanning filter, and the magnitude-square of $h(x)$ is a sinc-squared function. Therefore, $|h(x)|^2$ is sinc-squared response (the incoherent impulse response $h_{inc}(x) = |h(x)|^2$).

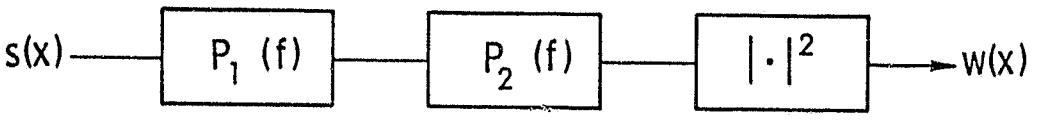

Figure 17: Simple Linear System Model for SAR

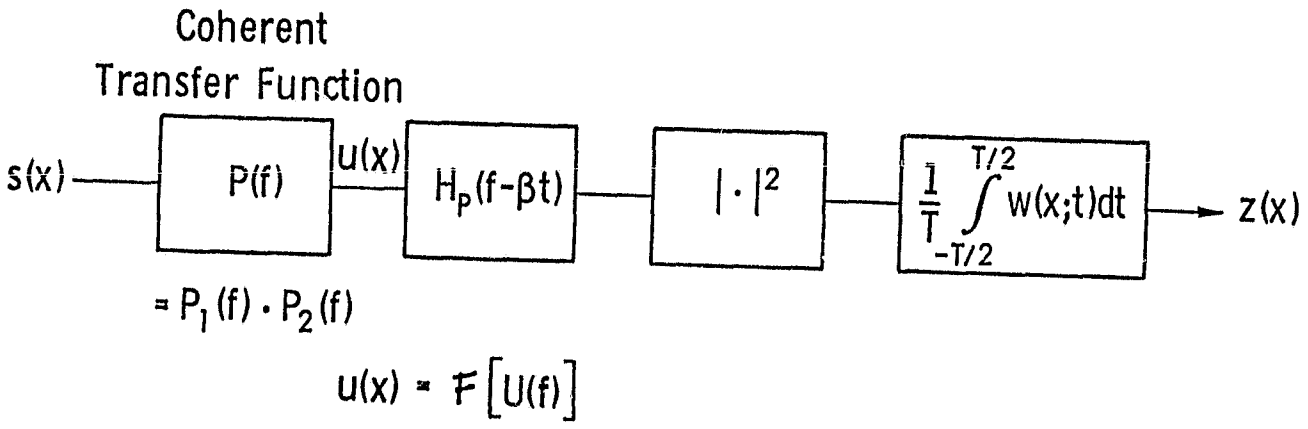

Figure 18: Scanning Mixed Integration Processing

We consider two cases in which the original image data are incoherently filtered to N looks and M looks, respectively. Then from equation (11.4) one can write

$$|s(x)*p(x)|^2*|h_N(x)|^2 = I_N(x) \qquad (11.5a)$$

and

$$|s(x)*p(x)|^2*|h_M(x)|^2 = I_M(x) \qquad (11.5b)$$

The impulse responses $h_M(x)$ and $h_N(x)$ have been written in this manner to indicate that the respective functions have the same analytical form, i.e., the same envelope, but the null-to-null widths may differ. If all the bandwidth B of the complex radar image spectrum is employed,

$$B = MB_M = NB_N \tag{11.6}$$

Let $g_N(x) = |h_N(x)|^2$ and $g_M(x) = |h_M(x)|^2$. . Using equation (11.4) and defining $I(x) = |s(x)*p(x)|^2$, , one can write

$$I_M(x) = I(x)*g_M(x)$$

$$I_N(x) = I(x)*g_N(x) \tag{11.7}$$

We note that because $I_M(x)$, $I_N(x)$ represent image data they are strictly positive functions, as must be $g_M(x)$ and $g_N(x)$ (they are sinc-squared impulse responses). Next we consider the filtering operation as shown in Figure 19, in which we seek to generate $I_M(x)$ from $I_N(x)$ using a filter with impulse response g(x), which also must be positive everywhere. Because the bandwidth of the data $I_N(x)$ is greater than that of $I_M(x)$ (g(x) is a lowpass filter), g(x) may exist for any situation in which M > N.
Thus, we seek g(x) to solve the problem

$$I(x)*g_N(x)*g(x) = I_M(x) = I(x)*g_M(x) \tag{11.8}$$

Taking the Fourier transform of both sides of equation (11.8), we obtain

$$I(f)\cdot G_N(f)\cdot G(f) = I(f)\cdot G_M(f) \tag{11.9a}$$

or, equivalently,

$$G(f) = \frac{G_M(f)}{G_N(f)} \tag{11.9b}$$

Because $g_N(x)$ and $g_M(x)$ are both sinc-squared impulse responses, $G_M(f)$ and $G_N(f)$ are both triangle functions (and zero phase functions) as shown in Figure 20 and can be described as

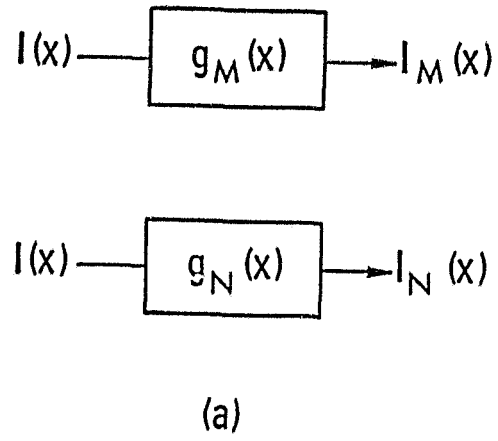

Figure 19: Inverse Filter-M Looks from N Look Image Data

$$G_M(f) = A_M(1 - |f|/B_M) \qquad |f| \leq B_M$$

$$= 0 \qquad \text{elsewhere}$$

$$G_N(f) = A_N(1 - |f|/B_N) \qquad |f| \leq B_N$$

$$= 0 \qquad \text{elsewhere} \qquad (11.10)$$

Therefore, G(f) has the form given by

$$G(f) = \frac{A_M}{A_N}\left[\frac{1 - |f|/B_M}{1 - |f|/B_N}\right] \qquad |f| \leq B_M$$

$$= 0 \qquad \text{elsewhere}$$

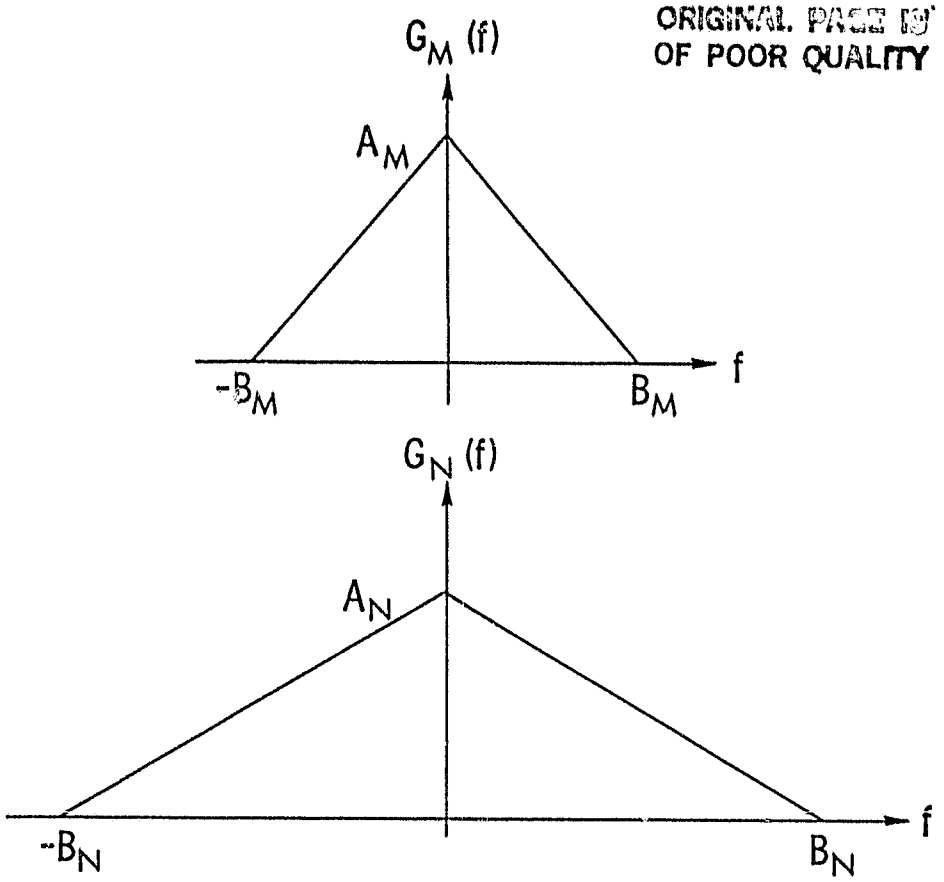

Figure 20: The Triangle Spectra of $G_M(f)$ an $G_N(f)$.

Because $B_N > B_M$ and f is always less than B_N over the nonzero region of G(f), the denominator of G(f) can be expanded in a convergent geometric series

$$G(f) = \left(1 - \frac{|f|}{B_M}\right)\left(1 + \frac{|f|}{B_N} + \frac{|f|^2}{B_N^2} + \cdots\right)$$

$$= \left(1 - \frac{M|f|}{B}\right)\left(1 + \frac{N|f|}{B} + \frac{N^2|f|^2}{B^2} + \cdots\right)$$

$$|f| \leq B_M \qquad (11.11)$$

Expanding G(f) and truncating the product beyond the quadratic terms yields

$$G(f) \approx 1 - \frac{(M-N)}{B}|f| - \frac{(MN-N^2)}{B^2}|f|^2 \qquad (11.12)$$

The truncation introduces negligible error, for example, when N=1 and M>10. When N increases, so must M to keep the approximation valid. G(f) can be rewritten as

$$G(f) \approx \frac{1}{2}\left(1 - \frac{|f|}{K_t} + 1 - \frac{|f|^2}{K_p}\right) \qquad |f| \leq B_M \qquad (11.13)$$

where

$$K_t = \frac{2(M-N)}{B}$$

$$K_p = \frac{2(MN-N^2)}{B^2}$$

Then it is fairly straightforward to find the Fourier transforms of the triangle portion of the spectrum and the parabolic portion, with the aid of the scaling rule (Bracewell [10]). The impulse response of the approximation in equation (11.13) was derived as g(x).

$$g(x) \approx \frac{\pi B}{2(M-N)}\left[\frac{\sin\left(\frac{\pi^2 Bx}{M-N}\right)}{\frac{\pi^2 Bx}{M-N}}\right]^2 +$$

$$\frac{\sqrt{2(MN-N^2)}}{4\pi^3 Bx^2}\left[\frac{\sin z}{z} - \cos z\right] \qquad (11.14)$$

where

$$z = \frac{4\pi^2 Bx}{\sqrt{2(MN-N^2)}}$$

The original requirement on g(x) was that it be positive everywhere, so application of the impulse response must be preceded by verifying that g(x) is non-negative. This was done experimentally for many values of M and N to examine the series (equation 11.11) truncation effects.

11.3 APPLICATION OF THE INCOHERENT FILTER

The importance of a technique for incoherently degrading an amplitude or intensity radar image (in the spatial domain) to an arbitrary number of looks stems from the fact that few investigators have access to the complex radar data. Likewise, it is not always feasible to generate the complex radar simulations described before, which can be filtered in the frequency domain to increase the number of looks at the cost of resolution.

Chapter 12

RADAR IMAGE SIMULATION: PRELIMINARY RESULTS

The purpose of this section is to present a sequence of radar image simulations which illustrate the simulation model and its successful implementation. Also these results show that simulation can be used to investigate the complex interactions (tradeoffs) between the terrain and sensor's images. In this preliminary tradeoff study, seven terrain features were modeled: linear hogback ridges oriented at five different angles with respect to the radar look direction and two symmetrical hogback ridges following elliptical paths each with different radii. Six different SAR system configurations were simulated for each terrain feature.

First, the simple models used to generate the elevation data bases characterizing the terrain are presented. Then the SAR system parameters are discussed and finally, the radar image simulations are presented.

12.1 SIMULATION OF SIMPLE GEOLOGIC TERRAIN FEATURES

A prerequisite to performing the system tradeoff study using radar image simulation is the modeling of the geologic terrain features. These models must then be used to generate terrain elevation data for input to the sensor simulation algorithms. The higher the level of realism in the simulated terrain the more useful the results of the sensor simulation and ultimately the more worthwhile the tradeoff study. However, as a first step only simple terrain features were modeled and simulated. (On-going research is being devoted to more realistic simulation of geologic terrain features.) Simple geologic features were selected because they are easy to implement and to evaluate; also, interpreting the resulting sensor images is also simple.

The simple terrain features were constructed by a two step process. The first step was to specify the location of the peak of the hogback ridges. For the linear ridges this was done simply by creating a binary digital image with each i,j pixel value assigned 255 if i,j was included as one location of the peak and zero otherwise. For the elliptical ridges the i,j pixel values assigned 255 were constrained to follow an elliptical path. (See Figures 21 and 22 for the

ridge location maps.) The second step in the process was to select the cross-section of the ridge which was to follow the path specified by the location maps, and to simulate the terrain feature by overlaying the selected cross-section orthogonal to the curve defining the peak positions. The cross-section used for this experiment is shown in Figure 23.

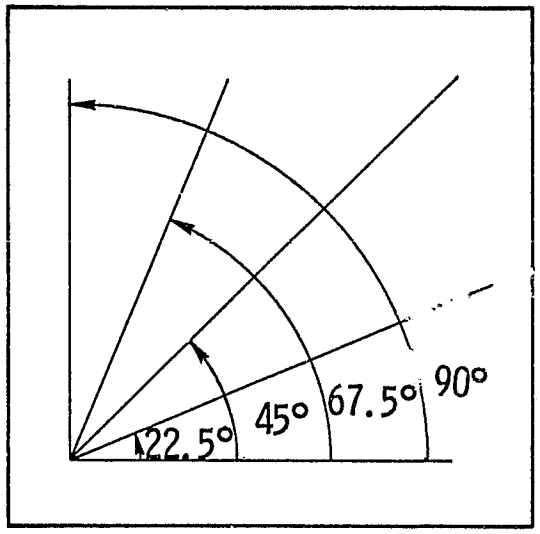

Figure 21: Angular Orientation of Linear Hogback Ridges

Two elevation data bases were thus constructed. However, to perform the sensor simulation each terrain location x,y (now on the i,j digital matrix position) must have an associated microwave scattering characteristic assigned as well as elevation. One microwave scattering characteristic was assigned to the entire scene, i.e., each data base matrix location i,j has a different elevation but the same scattering properties. Figure 24 is the graph of the microwave backscatter coefficient versus the angle of incidence used here. Note that this terrain property (scattering) is a function of several system parameters, e.g., frequency and

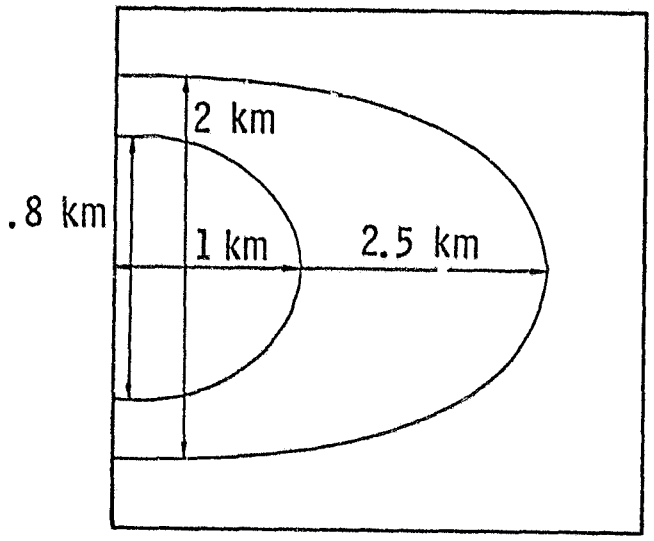

Figure 22: Geometry of Elliptical Hogback Ridges

polarization; thus in any tradeoff analysis the backscatter versus angle would change with these system parameters. In the simulation algorithms, the local angle of incidence is calculated and its corresponding backscatter value is used to determine the expected value of the return power for each terrain location.

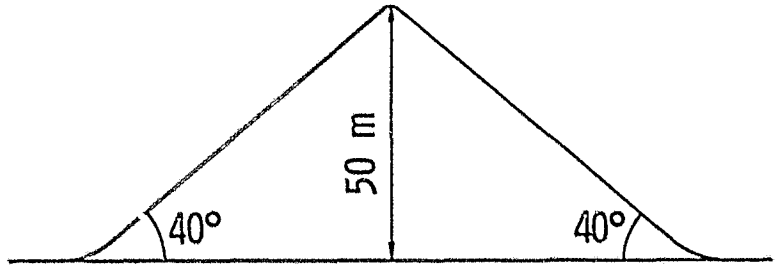

Figure 23: Cross-Sectional View of Geologic Feature Models

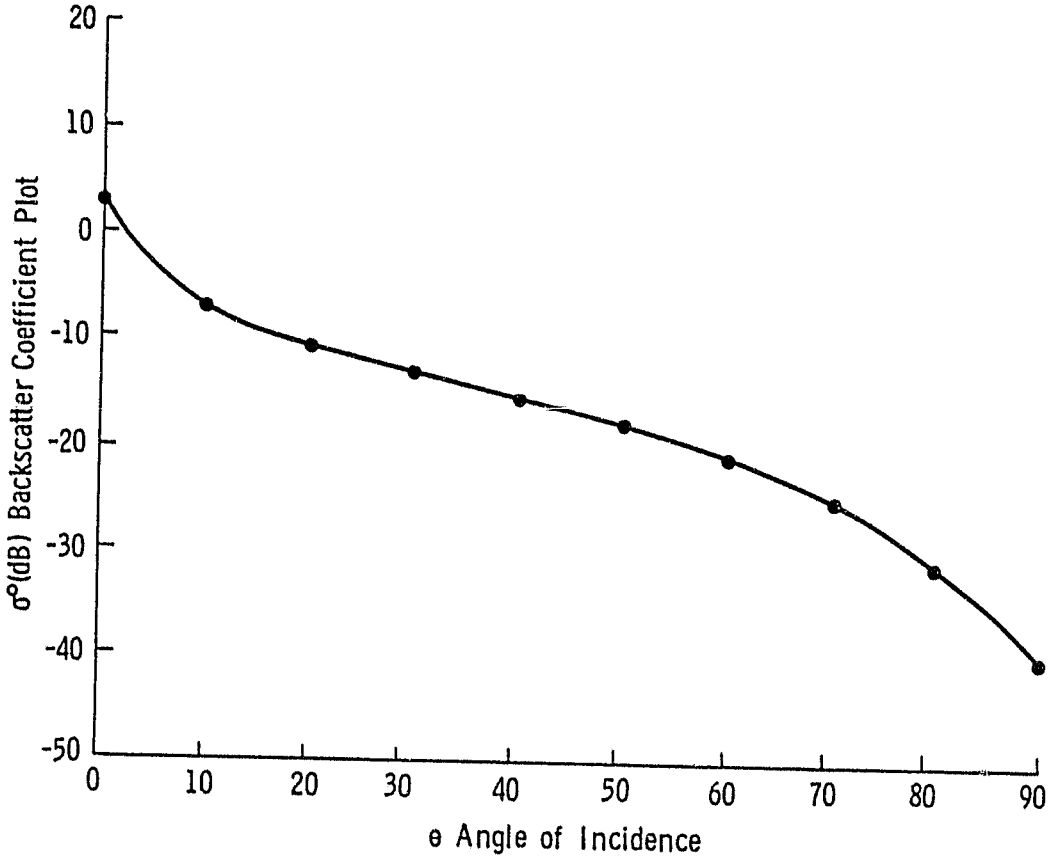

Figure 24: Backscatter Coefficient Data for Radar Simulation

12.2 SIMULATED SAR SYSTEM CONFIGURATIONS

Six different SAR system configurations were simulated for each of the data bases described in the preceding section. Table 3 contains the various system parameters for each configuration. This preliminary study was restricted to evaluating only two system parameters, radar angle of incidence and averaging.

TABLE 3

System Parameters

	Resolution	Radar Angle of Incidence	Number of Look Averaged
1	25m	23°	1
2	25m	23°	4
3	25m	40°	1
4	25m	40°	4
5	25m	60°	1
6	25m	60°	4

To interpret the images, the simulation procedure is very briefly reviewed. For each data base matrix location i,j (in this case the pixel spacing in the data base was set to 6.25 m) an average returned power is calculated. Incorporated into its calculation are all radar and geometric effects, e.g., layover, shadow, etc., for the selected angle of incidence. A matrix of averaged returned power is thus created. This matrix can be scaled and displayed as an image. The images are totally deterministic in nature and have also been generated for each of the three angles of incidence for each data base. These images allow for the investigation of deterministic tradeoff between sensor and terrain parameters. Even though these same tradeoffs could be determined analytically, the image analysis approach is superior because the ultimate users of the data are generally image interpreters.

A radar hologram is generated next directly from the power matrix by Monte Carlo techniques. Various resolution and averaging effects are simulated by applying a linear spatially invariant filter. This filter can be implemented in either the spatial or spatial frequency domain. The equivalent width of the filter's impulse response determines the simulated resolution. The output of the filter must be formatted for display. The transformation between the output complex pixel value and the output real pixel value can be arbitrarily specified. Common point transformations include displaying the pixel power, pixel amplitude on the logarithm of the pixel power. The SEASAT-A SAR system displayed the pixel amplitude; thus for these simulations the pixel amplitude was displayed. Noncoherent integration can be achieved either by directly mimicking a discrete mixed integration operating in the spatial frequency domain or an equivalent continuous mixed integration simulated by a filter in the spatial domain. Either approach produces the required averaging versus resolution trade-off.

The images presented in the following section were generated by techniques described above. The discrete mixed integrator was simulated to produce the four look images.

12.3 THE SIMULATION RESULTS

A series of radar simulations were generated for linear and elliptical hogback ridges on level ground. The geometric cross-sections of the features are triangular and symmetrical in general, with an angle of 40 degrees between the triangle base and sides. The maximum height of all the features is approximately 50 m as seen in Figure 23. A particular radar backscatter cross-section function (which varies with angle of incidence) was assigned to both the features and the level background (Figure 24). The same statistic characteristics were assigned to both the ridges and the level ground, i.e., Rayleigh statistics. For each simulation three images were generated which represent the power map of calculated average power based solely upon the radar equation, taking into account all considerations (e.g., local slope) except fading. The second image of each set represents a fully coherent, 25 m by 25 m resolution depiction of the scene. The third image of each set has the same resolution, but has four independent samples averaged (without sacrifice of resolution).

In the sensor images of the linear hogback ridges with an incidence angle of 23 degrees, there are no shadows in the simulation but the large local angles make the backslopes of the features appear dark in contrast with the high reflectivity of the level background (for the no-fading case), as

seen in Figure 25. The radar look direction goes from left to right. Because of the geomtery of this scene, layover is apparent for the first two ridges (counting from the vertically aligned ridge, left to right). Other functions of geometry that are noticeable are the narrowing foreslope representations with increased ridge angle away from vertical in the image. The horizontally aligned feature appears to have a flat top (and higher reflectivity than the sides of the ridge) because of the facet model effects. Figure 25 (1 look, 25 m resolution) shows the deleterious effects of poor signal-to-noise ratio characteristic of fully coherent sensor images. The horizontal feature has almost disappeared for this noise level. Averaging four looks, as is illustrated in the third image of Figure 25, restores the detectability of the fifth feature, although its characterization in this scene does not hint that the underlying feature is a linear ridge.

When the angle of incidence is increased to 40 degrees (altitude unchanged) the background backscatter variation is seen upon comparison with Figure 25. Again, local angle effects darken the backslopes; there is still no shadow given this particular geometry. Significant foreslope compression also occurs in this case; foreslope brightening is apparently due to a zero degree local slope for the vertically aligned ridge. The horizontal ridge is somewhat difficult to discern even in the "no-noise" case (Figure 26, power map). Figure 26 (1 look case) illustrates the loss of detectability for that ridge which is aligned parallel with the radar look direction (horizontally). Because a multiplicative noise model can be used to describe the faded scenes, note that the brightness variations are smaller for the 1 look case than for the 4 look case in Figure 26. (The mean-to-standard deviation ratios are approximately equal, however.) The 4 look case of Figure 25 shows that averaging four looks does not really restore the fifth ridge, but does improve the interpretability for the four other hogback ridges.

With an angle of incidence equal to 60 degrees the background region has dropped greatly in reflectivity, and simple geometric calculations show that shadows now exist for the backslope regions. Again layover can occur and foreslopes are compressed in this representation; they are very bright because of local angle considerations. In the power map of Figure 27, the horizontally aligned ridge is all but gone, disappears in the speckle of the 1 look case, and is not visible in the averaged image (4 look case).

The elliptical hogback ridges were simulated for sensor parameters illustrated previously. For the case of 23 degree angle of incidence, Figure 28, power map case, there is no shadow, but very dark (relative to the background) back-

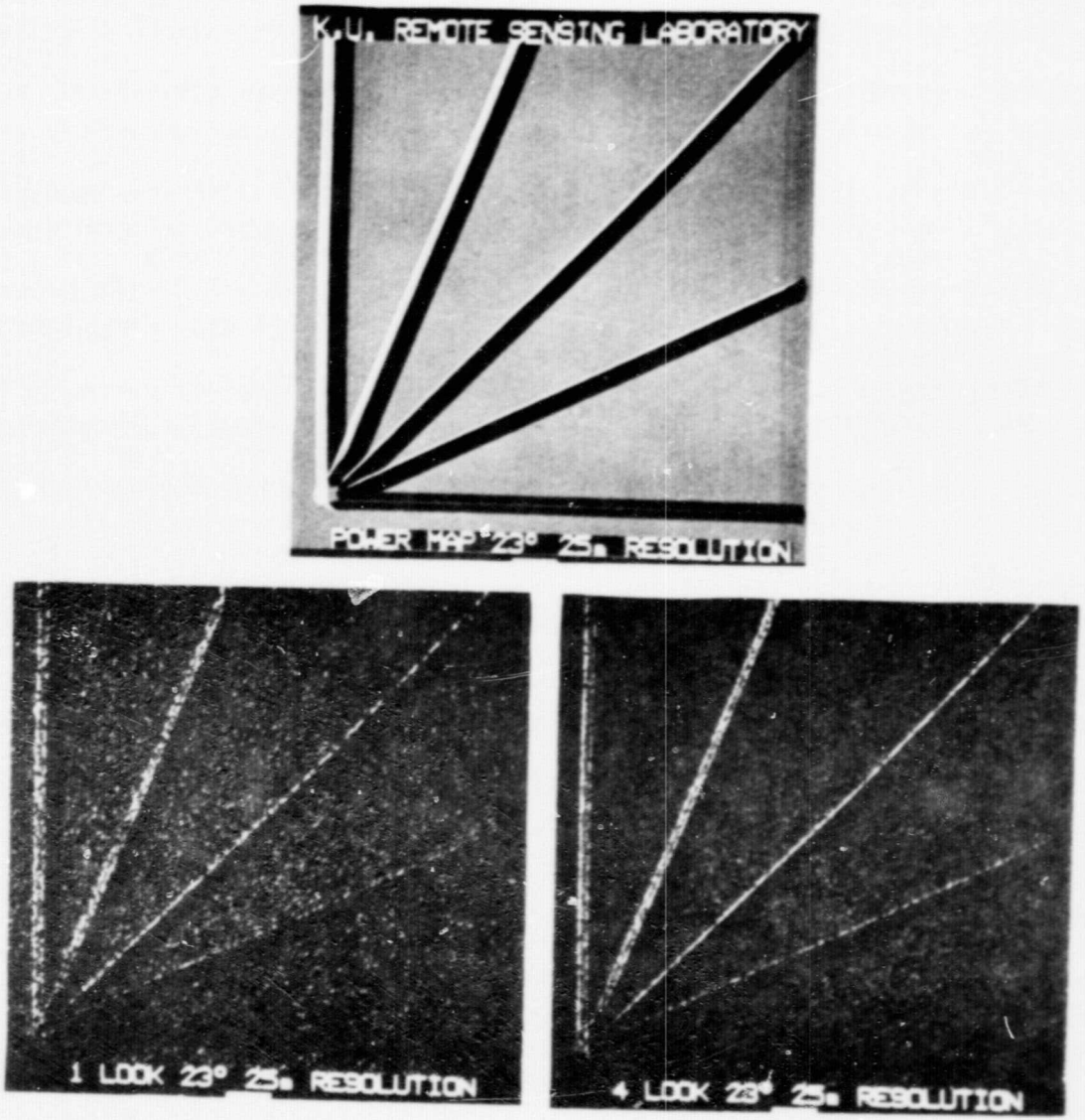

Figure 25 Linear Ridges and 23° Angle of Incidence.

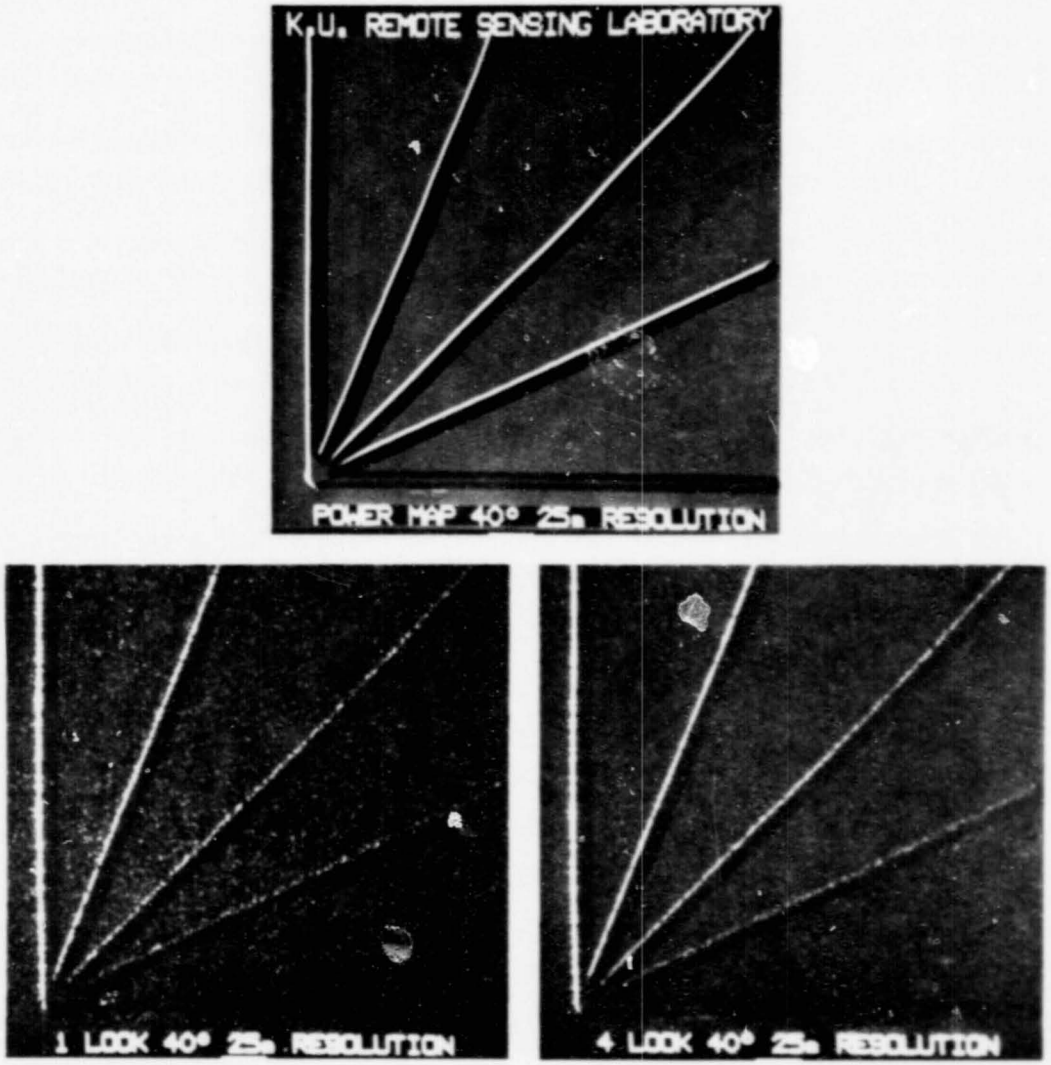

Figure 26: Linear Ridges and 40° Angle of Incidence.

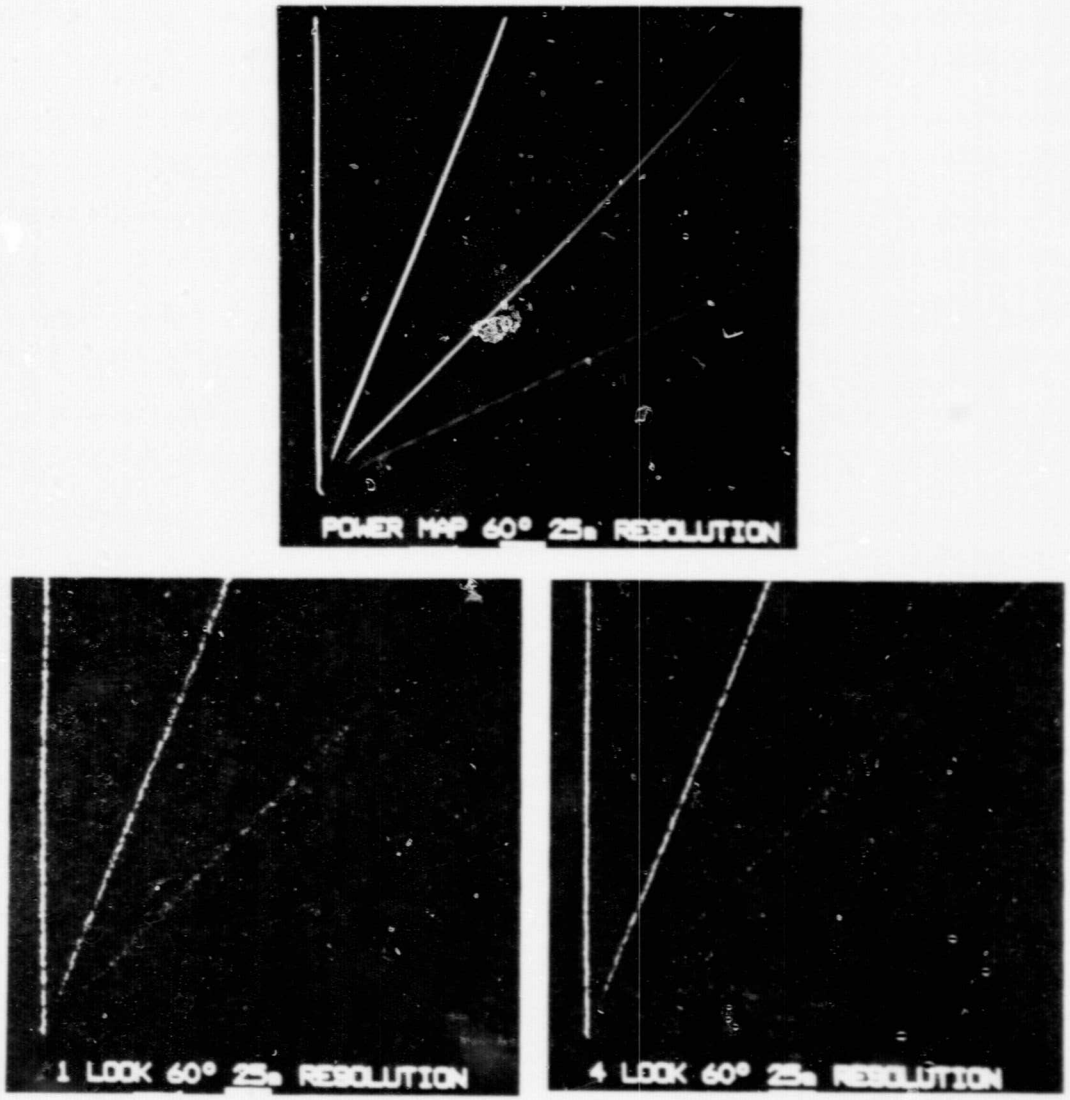

Figure 27: Linear Ridges and 60° Angle of Incidence.

slopes due to local angle variations. Layover is seen at the ground-ridge interface in the image. The bright line along the crest of the ridge is due to facet model effects. The portion of the ridge oriented parallel with the radar look direction will become less detectable, as in the noisy 1 look image of Figure 28. Averaging four looks improves the interpretability of such a ridge geometry (and orientation) as viewed in the figure.

At a 40 degree angle of incidence, the elliptical ridge is more difficult to discern (given this particular backscatter model) in Figure 29 (power map). The darkening is again due to local angle and not to shadow. Portions of the ridge become difficult to see in the faded scene of the 1 look case of Figure 29, whereas averaging to four looks just barely allows the feature to be seen (i.e., the part of it which is parallel with the radar look direction). The fact that it is a portion of such a ridge type would probably not be recognized without supplementary knowledge.

The 60 degree angle of incidence case is shown (power map) in Figure 30. Given this specific combination of backscatter model, ridge model, and orientation, the greater part of the geologic feature disappears in the fully coherent scene of the 1 look case in Figure 30. Averaging four looks helps to determine the outline of the feature, but the image in Figure 30 provides few clues for the identification process.

Two major conclusions can be stated from these results. First, even for a very simple geologic feature, a linear hogback ridge, the character of its radar image changes drastically with its orientation to the radar look direction. Therefore, it will be difficult if not impossible to determine the optimum sensor parameters for detecting general linear hogback ridges. However, simulation will provide an indication of the geologic mapping potential with respect to linear hogback ridges at a specific orientation in relation to the radar given different sensor configurations. Further, these results indicate that totally automatic detection algorithms for linear hogback features will be very difficult to develop because of the diversity of their image manifestation.

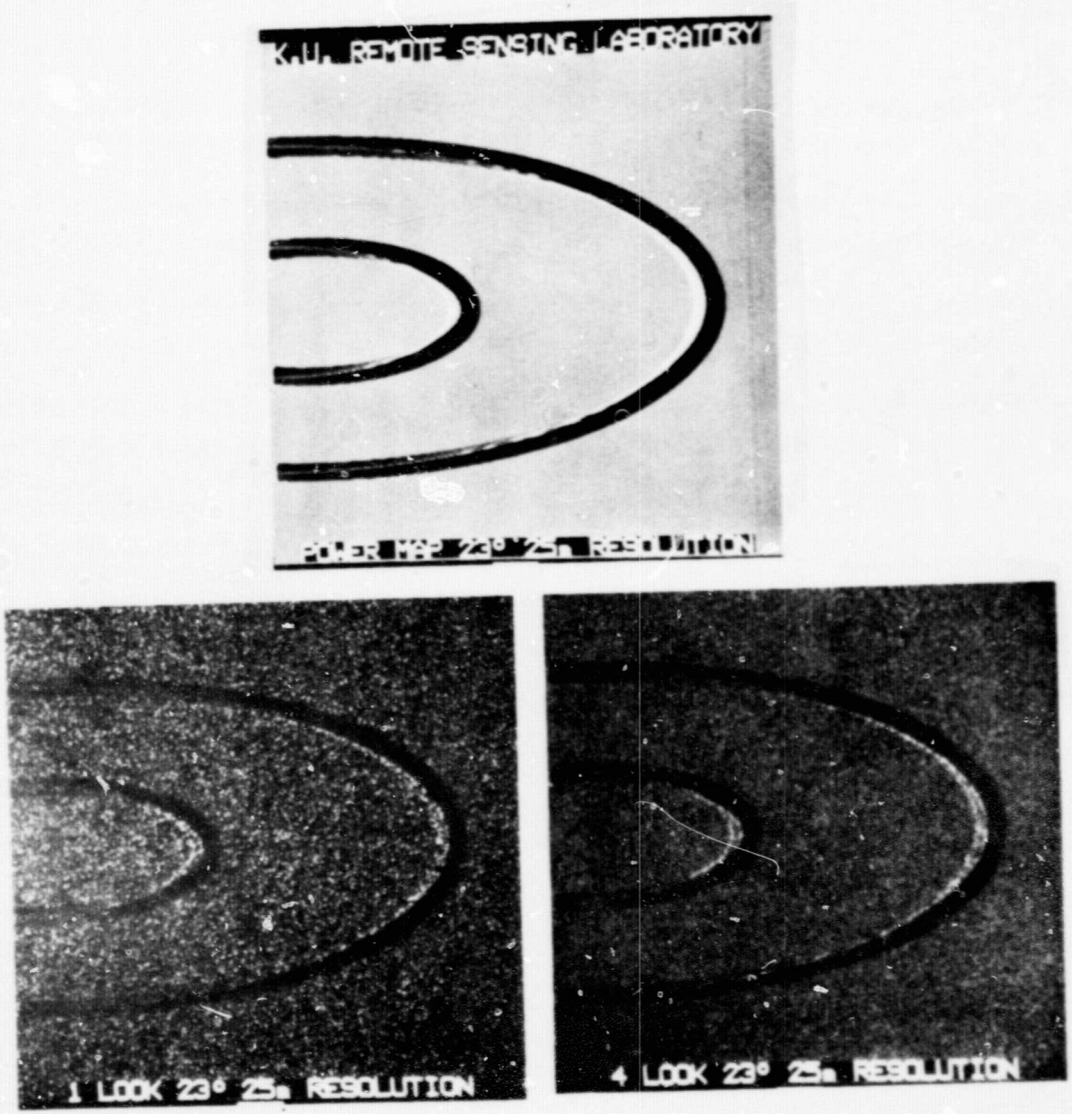

Figure 28: Elliptical Ridges and 23° Angle of Incidence.

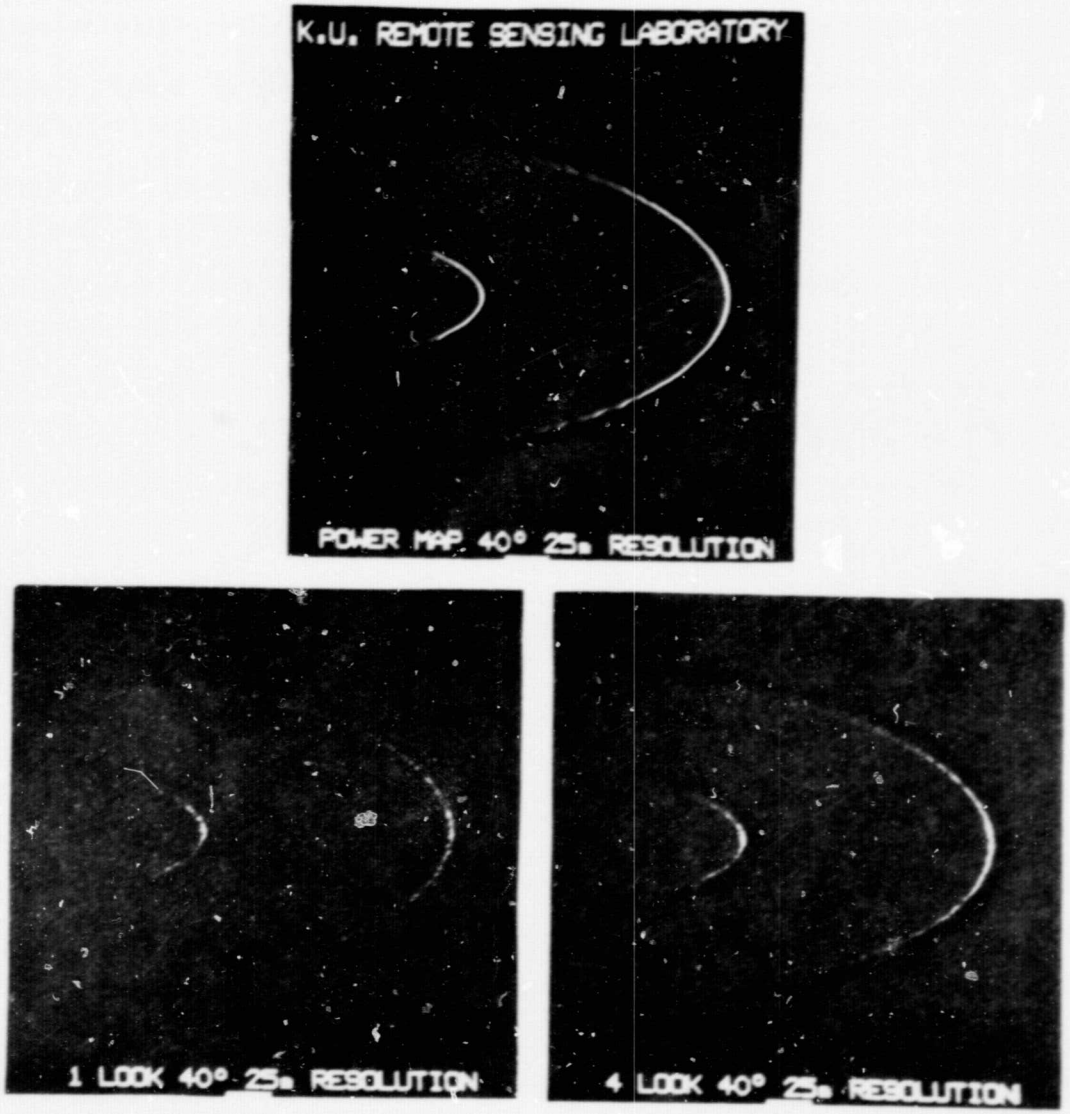

Figure 29: Elliptical Ridges and 40° Angle of Incidence.

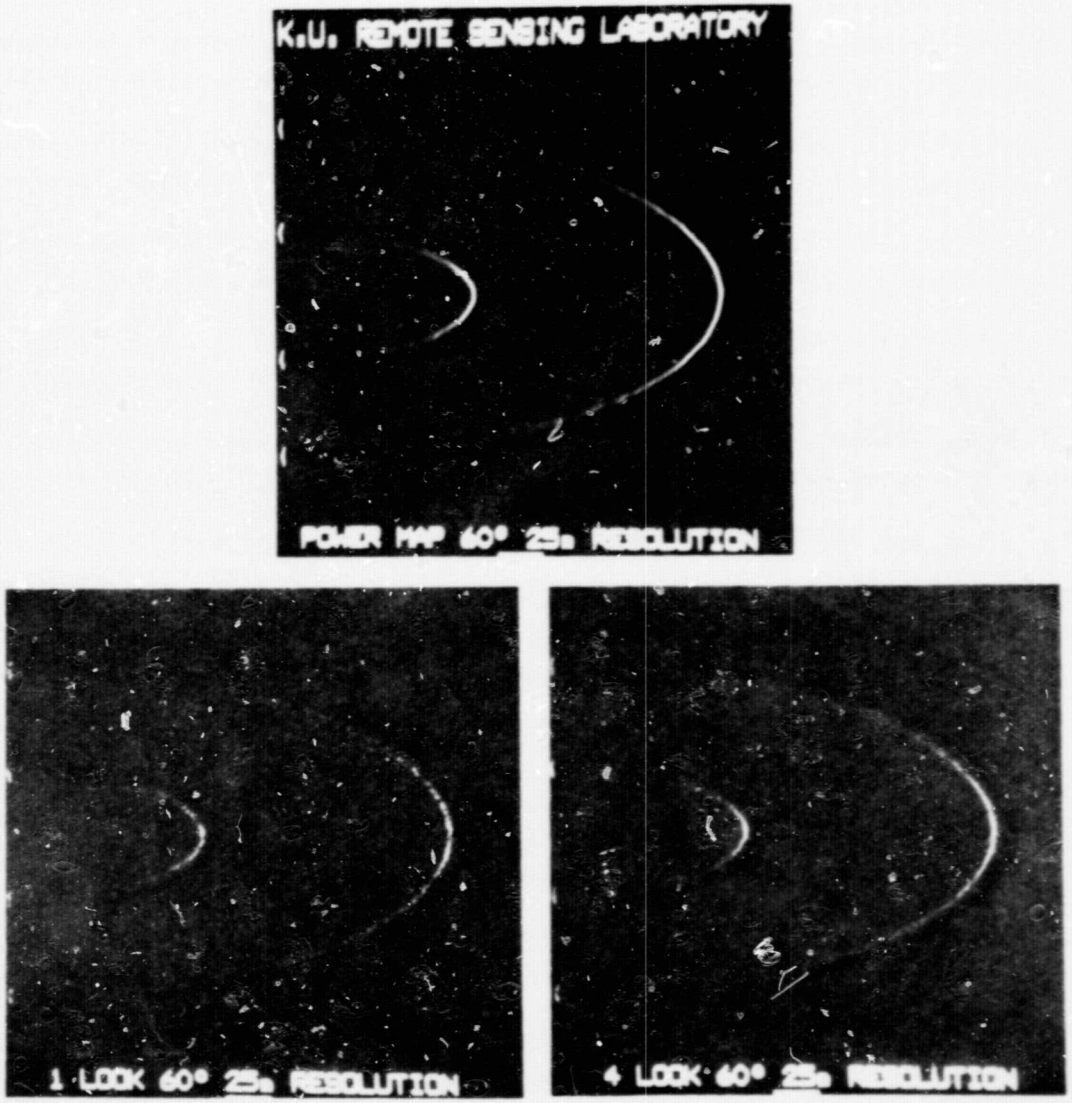

Figure 30: Elliptical Ridges and 60° Angle of Incidence.

Chapter 13

CONCLUSIONS

The analysis portion of the work reported herein shows promise for texture measures of SAR images by the GLC matrix approach despite the poor signal-to-noise ratio in the N=4 SEASAT SAR images employed in this study. The look angle dependence of the GLC results must be investigated because these effects must be factored into future use of automated texture analysis. Point statistics investigations are being pursued and will be reported for phase two, along with an update on texture analysis.

The synthesis portion of this work produced geologic feature data bases for linear and elliptical hogback ridges. The radar image simulations were produced assuming one category (backscattering type) was present, and clearly demonstrated angle of incidence and fading effects. The geologic features in this first phase of work are deterministic; random terrain models will be a refinement of the procedure and are being pursued for phase two.

REFERENCES

1 Dellwig, L. F., H. C. MacDonald, and J. M. Kirk, 1968, "The Potential of Radar in Geological Exploration," Proc. Fifth Symp. on Remote Sensing of Environment, Univ. of Michigan, Ann Arbor, pp. 747-763.

2 MacDonald, H. C., 1969, "Geologic Evaluation of Radar Imagery from Darien Province, Panama," Modern Geology, Vol. 1, No. 1, pp. 1-63.

3 Wing, R. S., 1971, "Structural Analysis from Radar Imagery, Eastern Panamanian Isthmus," Modern Geology, Vol. 2, No. 1, pp. 2-21, No. d, pp. 75-127.

4 Wing, R. S. and H. C. MacDonald, 1973, "Radar Imagery Identifies Hidden Jungle Structures," World Oil, Vol. 176, No. 5, pp. 67-70.

5 Dellwig, L. F. et al., 1975, "Use of Radar Images in Terrain Analysis: An Annotated Bibliography," RSL Tech. Rpt. 288-2, Univ. of Kansas Center for Research, Inc., Lawrence, KS, 327 pp.

6 MacDonald, H. C., 1976, "Use of Radar in Geology," Geoscience Applications of Imaging Radar Systems, RSES, Remote Sensing Comm. of Amer. Assoc. Geog., Vol. 3, No. 3, 93-104.

7 Dellwig, L. F. and R. K. Moore, 1977, "Tradeoff Considerations in Utilizatation of SLAR for Terrain Analysis," Proc. 1st Annual Pecora Memorial Symp., Sioux Falls, SD, pp. 293-306.

8 Moura, J. M. de, 1972, 'Projecto RADAM: levantamento dos recursos naturais dos Regoes Amazonica e Nordestes do Brasil por meio do radar e outros sensores," Revista Brasileria de Cartografia, v. 3, no. 6, p.1-6.

9 (Anonymous), 1980, "Digital Terrain Tapes, User Guide," Second Edition, National Cartographic Information Center, U. S. Department of the Interior, Geological Survey, U. S. Government Printing Office: 0-311-344/184.

10 Bracewell, R. N., 1978, The Fourier Transform and Its Applications, Second Edition, McGraw-Hill, New York.

11 Kaupp, V. H., H. C. MacDonald, and W. P. Waite, 1981, "Geological Terrain Models," Proc. 1981 International Geoscience and Remote Sensing Symposium, Washington, D. C.

12 Kaupp, V. H., H. C. MacDonald, and W. P. Waite, 1981, "Imaging Radar: Analysis of Propagation Distortions," Arkansas Remote Sensing Laboratory Technical Report, ARSL TR 81-1, University of Arkansas, Fayetteville.

13 Kaupp, V. H., H. C. MacDonald, and W. P. Waite, 1981, "Using Radar Image Simulation to Assess Relative Geome-

tric Distortions Inherent in Radar Imagery," Proc. 1981 International Geoscience and Remote Sensing Symposium, Washington, D. C.

14 Waite, W. P., H. C. MacDonald, J. S. Demarcke, and B. H. Corbell, "Look Direction Dependence on Radar Backscattering Cross Section for Agriculture Fields," Proc. Amer. Soc. Photogramm., Fall Technical Meeting, Niagara Falls, N. Y., p.R-2-6-1-14.

15 Ulaby, F. T., January 1975, "Radar Response to Vegetation," IEEE Transactions on Antennas and Propagation, Vol. Ap-23, No. 1, pp. 36-45, and "Radar Response to Vegetation II: 8-18 GHz Band," IEEE Transactions on Antennas and Propagation, Vol. AP-23, September 1975, pp. 608-618.

16 Cosgriff, R. L., W. H. Peake, and R. C. Taylor, May 1960, "Terrain Scattering Properties for Sensor System Design," Eng. Experiment Station Bulleting, 181, Vol. 29, Ohio State University, Columbus.

17 Fung, A. K. and H. L. Chan, September 1969, "Backscattering of Waves for Composite Rough Surfaces," IEEE Transactions on Antennas and Propagation.

18 Hevenor, R. A., October 1971, "Backscattering of Electromagnetic Waves from a Surface Composed of Two Types of Surface Roughness," TR-ETL-71-4, Engineering Topographic Laboratories, Fort Belvoir, Virginia.

19 Goodman, J. W., Introduction to Fourier Optics, New york: McGraw Hill, 1968, pp. 150-153.

20 Moore, 1975, R. K., "Microwave Remote Sensors," Manual of Remote Sensing, Chapter 9, American Society of Photogrammetry, Falls Church, VA.

21 Kaupp, V. H., W. P. Waite, and H. C. MacDonald, 1981, "Which Angle of Incidence is Best for Imaging Radars?," proc. 1981 International Geoscience and Remote Sensing Symposium, Washington, D. C.

22 Daily, M. C., C. Elachi, T. Farr, W. Stromber, S. Williams and G. Schaber, March 30, 1978, "Application of Multispectral Radar and LANDSAT Imagery to Geologic Mapping in Death VAlley," JPL Publication 78-19, Jet Propulsion Laboratory, Pasadena, California.

23 Evans, D. L., October 1, 1978, "Radar Observations of a Volcanic Terrain: Askja Caldera, Iceland," JPL Publication 78-81, Jet Propulsion Laboratory, Pasadena, California.

24 Reeves, R. G. (editor), Manual of Remote Sensing, Volume I, American Society of Photogrammetry, Falls Church, VA, 1975.

25 Rosenfeld, A. and E. B. Troy, June 1970, "Visual Texture Analysis," Computer Science Center, University of Maryland.

26 Haralick, R. M. and D. Anderson, 1971, "Texture Tone Study," Technical Report 182-2, Univeristy of Kansas Center for Research, Inc., Lawrence.

27 Sutton, R. N. and E. L. Hall, July 1972, "Texture Measures for Automatic Classification of PUlmonary Disease," IEEE Trans. Computers, Vol. C-21, No. 7, pp. 667-676.
28 Haralick R. M., K. Shanmugam and I. Dinstein, November 1973, "Textural Features for Image Classification," IEEE SMC Trans., Vol. SMC-3, pp. 610-621.
29 Galloway, M. M., June 1975, "Texture Analysis Using Gray Level Run Lengths," Computer Graphics and Image Processing, Vol. 4, No. 2, pp. 172-199.
30 Shanmugam, K. and R. M. Haralick, October 1973, "Computer Classification of Reservoir Sandstones," IEEE Trans. on Geoscience Electronics, Vol. GE-11, pp. 171-177.
31 Haralick, R. M. and K. Shanmugam, June 1974, "Combined Spectral and Spatial Processing of ERTS Imagery," Remote Sensing, Vol. 3, pp. 3-13.
32 Kruger, R. P., W. B. Thomson and F. A. Turney, January 1974, "Computer Diagnosis of Pneumoconiosis," IEEE SMC Trans., Vol. SMC-4, No. 1, pp. 40-49.
33 Weszka, J. S., C. R. Dyer and A. Rosenfeld, April 1976, "A Comparative Study of Texture Measures for Terrain Classification," IEEE SMC Trans., Vol. SMC-6, No. 4, pp. 269-285.
34 Connors, R. W. and C. A. Harlow, May 1980, "A Theoretical Comparison of Texture Algorithms," IEEE Trans. Pattern Analysis and Machine Intelligence, Vol. PAMI-2, No. 3, pp. 204-223.
35 Holtzman, J. C., V. H. Kaupp, J. L. Abbott, V. S. Frost, E. E. Komp and E. C. Davison, September 1977, "Radar Image Simulation: Validation of the Point Scattering Method," Engineer Topographic Laboratories Contract Report, ETL-0017, Volume One.
36 Holtzman, J. C., J. A. Stiles, V. S. Frost, V. H. Kaupp and E. E. Komp, June 1979, "A Digital Computation Technique for Radar Scene Simulation: NEWSLAR," Simulation, Vol. 24, No. 6, pp. 183-192.
37 Brown, William M., March 1967, "Synthetic Aperture Radar," IEEE Trans. on Aerospace and Electronics Systems, Vol. AES-3, No. 2, pp. 217-229.
38 Harger, R. O., 1970, Synthetic Aperture Radar Systems: Theory and Design, Academic Press, New York.
39 Mitchell, R. L., June 1974, "Models of Extended Targets and Their Coherent Radar Images," Proceedings of the IEEE, Vol 62, No. 6, pp. 754-758.
40 Bell, J. W., October 1976, "Digital Simulation of High Resolution Radar Imagery," RADC-TR-290, Romer Air Development Center, Griffiss Air Force Base.
41 Beckner, F. L. and G. L. Crow, January 1977, "Definition of a Mathematical Model for an Orbiting Imaging Radar," ARL-TR-77-6, Univ. of Texas ARL, Austin, Texas.
42 Holtzman, J. C., V. H. Kaupp, J. L. Abbott, V. S. Frost, E. E. Komp and E. C. Davison, September 1977, "Radar Image Simulation: Validation of the Point Scat-

tering Method," Engineer Topographic Laboratories Contract Report, ETL-0018, Volume Two.

43 Holtzman, J. C., V. S. Frost, J. L. Abbott and V. H. Kaupp, October 1978, "Radar Image Simulation," IEEE Trans. Geoscience Electronics, Vol. GE-16, No. 5, pp. 296-303.

44 Zelenka, J. S., November 1976, "Comparison of Continuous and Discrete Mixed Integrator Processors," J. Opt. Soc. Am., Vol. 66, No. 11, pp. 1295-1304.

45 Porcello, L. J., N. G. Massey, R. B. Innes and J. M. Marks, November 1976, "Speckle Reduction in Synthetic Aperture Radars," J. Opt. Soc. Am., Vol. 66, No. 11, pp. 1305-1311.

Appendix A

GEOLOGICAL TERRAIN MODELS

V. H. Kaupp, Asst. Professor,
Dept. of Electrical Engineering
H. C. MacDonald, Professor,
Dept. of Geology
W. P. Waite, Professor,
Dept. of Electrical Engineering
University of Arkansas, Fayetteville, Arkansas 72701

Chapter 1

INTRODUCTION

To date, relatively little research has been devoted to the development of optimum specifications for the radar sensor, or for optimum strategies for information extraction from radar data. Careful examination of the problem readily explains the situation. Only a limited number of radar systems have been available for geologically dedicated research programs, and evaluation has consisted of observations derived from analysis of imagery. Research has been conducted with only a limited number of combinations of sensor parameters such as frequency, polarization, depression angle (or angle of incidence), look direction, and resolution.

This deficiency in control of system parameters is overcome with the advent of computer-modeling techniques via radar image simulations. Definitive studies to optimize the complete radar remote sensing system for geology can now be made. Image simulation provides a cost-effective method for modeling terrain variation, predicting of results, and defining of optimum sensor parameters.

The first phase has recently been completed of a program to determine the interpretation strategy and best radar sensor configuration for geological applications. In this initial work, terrain modeling and radar image simulation have been used to perform extensive parametric sensitivity studies. Several terrain models have been created and numerous radar image simulations have been produced from them. It is concluded that computer-modeling via image simulation provides a cost-effective method for evaluating terrain variations, predicting results, and defining optimum sensor parameters.

Chapter 2

GEOLOGIC MODELS

In this initial work, several geological terrain models have been created. These models represent the textbook case in that they are composed of relatively simple geometric shapes that are analytically defined, and that they are completely deterministic being totally devoid of geologic noise (ie., drainage patterns, weathering effects, surface cover boundaries over the landscape model, etc.). They provide, however, ideal constructions to evaluate how the radar scene changes for a specific landscape model as radar sensor parameters are changed.

An example of such a geological (landscape) model is presented in Figure 1. Additional models have been constructed, but there is insufficient space to describe more than this one. This model was created mathematically. It consists of a grid matrix containing 512 x 512 elements. Each element symbolically represents a square region of 15.625 m on the ground (ie., an area of 244.14 sq m). The complete matrix, then, represents a square region of 64 sq km; each side being 8 km long. Each entry in the matrix specifies the terrain elevation at a point on the ground. The maximum elevation, along the crest-line, was set at 100 m.

As can be seen in the figure, the landscape model illustrated in the three-dimensional plot is that of a breached anticline and syncline. The anticline is readily identified as the structure having the long nose and infacing escarpments, while the syncline has no nose and outfacing escarpments. Slope angles have been set for these features from a plunge angle of 8 degrees (on the nose of the anticline) to approximately 60 degrees for the very steep escarpments, and to approximately 23 degrees on the more gradual slopes.

This model was created mathematically as a sinusoid rotated 8 degrees from the surface tangent plane so that it plunges into the ground. The period of the sinusoid was set so that both the desired slope angles and feature scale would be attained. As constructed, the sinusoid produced gradual slopes. When the elevation reached 100 m at any location, the sign of the function was reversed and a scale factor applied to accelerate the drop back to level ground. In this way, gradual slopes rising to a height of 100 m and terminating in steep escarpments were created.

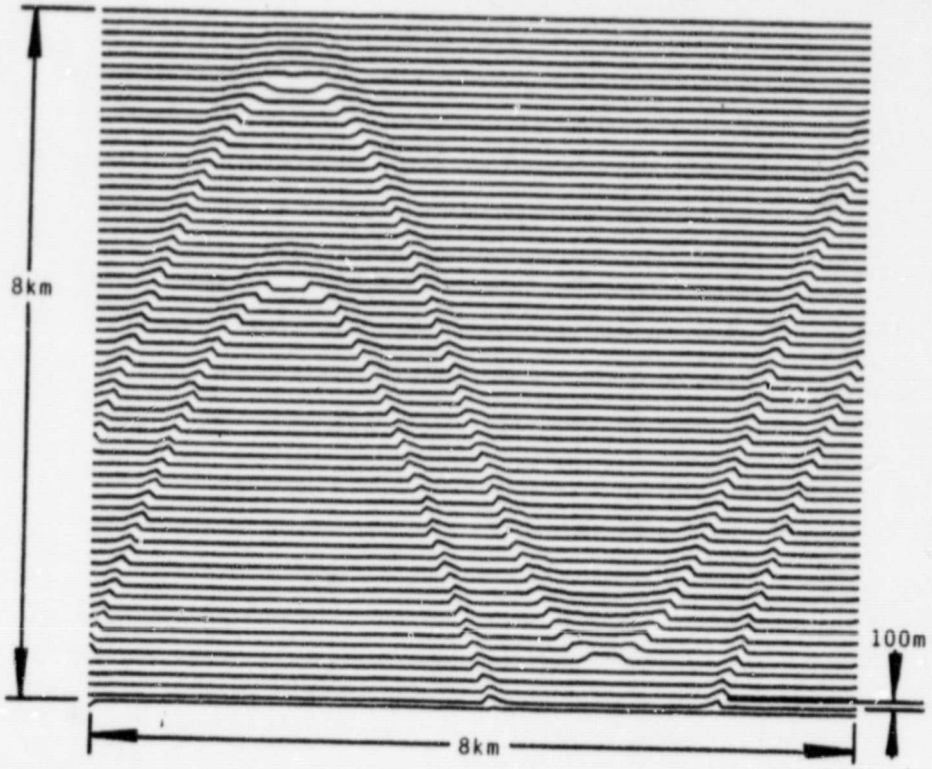

Figure 1: Landscape Model

Chapter 3

RADAR IMAGE SIMULATION

A very general approach to simulation has been developed at the University of Arkansas[1]. Figure 2 illustrates a block diagram of the computer programs. As can be seen from the figure, the simulation computer programs can produce selected intermediate and final results. The required inputs to the simulation programs are a data base and a backscatter file. Five different intermediate and final results can be produced. These are: 1). power map image; 2). slant-range image; 3). ground-range image; 4). slant-range image with noise; and 5). ground-range image with noise. Antenna and resolution effects can be incorporated via processing either in the spatial domain via convolution, or in the spatial frequency domain via the Fast-Fourier Transform and multiplication. These are all separately discussed.

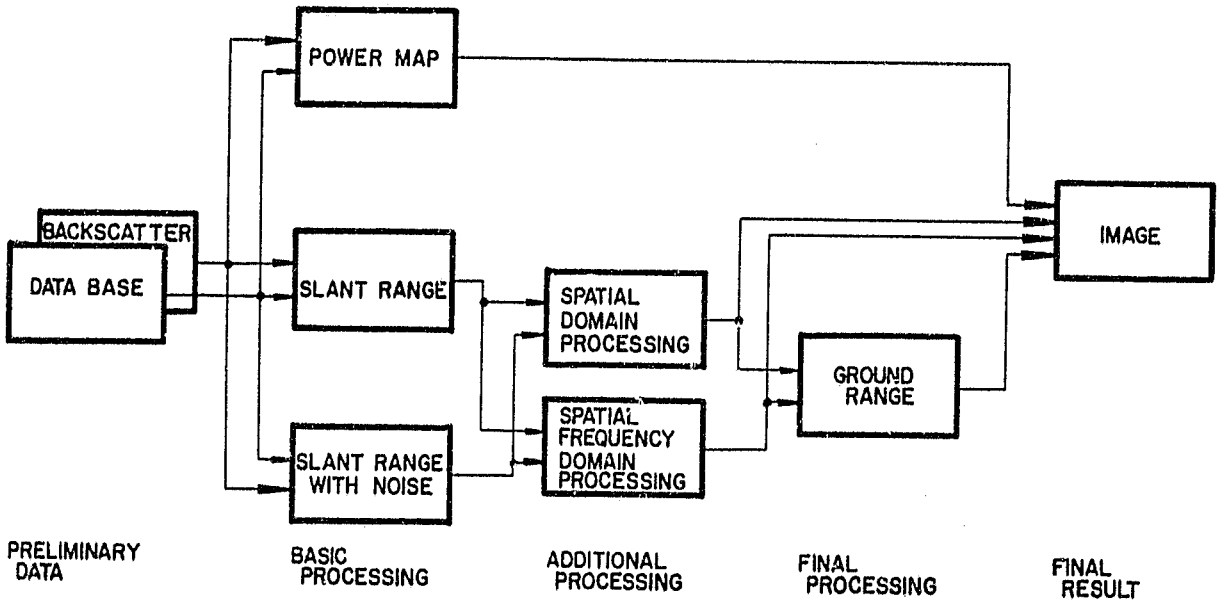

Figure 2: Simulation Computer Programs

3.1 DATA BASE

The data base is a digital replica of the ground and is the input mechanism for getting the terrain model into the computer simulation programs. This digital representation symbolizes the ground and its surface materials (ie., its cover) in a grid matrix having at least four dimensions; two for the horizontal location of each point, one for its elevation, and at least one for its cover type. Digital terrain data (ie., digital representations of terrain elevations) are used as the spatial information in a data base. These data represent either actual terrain elevations or mathematical models of terrain elevations. The data plotted in Figure 1 represents one kind of data base.

C-2

3.2 BACKSCATTER FILE

The backscatter file contains a model for the reflectivity for each terrain cover type present in a data base. It is these backscatter data which model the interaction between the transmitted electromagnetic energy and each cover type. They account for important properties both of the ground such as the complex permittivity and surface roughness, as well as of the radar such as the transmission frequency and polarization. Empirical backscatter data such as those published by Ulaby[2], or Cosgriff et al.[3] are used where possible. Theoretical backscatter models such as Fung and Chan[4], or Hevenor[5] are often important.

3.3 SIMULATION MODEL TRANSFER FUNCTION

For simulation purposes, a radar is modeled as the system illustrated in Figure 3. As can be seen from the figure, the transfer function can be symbollicaly written as

$$D = \gamma \log[f(h*P_r)] + K \qquad (1)$$

where D symbolizes the density of silver grains in the film of an image, γ is the film gamma (ie., the slope of the D vs logE curve), and K is a constant depending upon the development processing as discussed by Goodman[6]. This result arises from convolving the systems blurring function (h) with the input power (P_r). The input power is the average return power (Pr) predicted by the radar equation[7,8] multiplied by random noise (N_0).

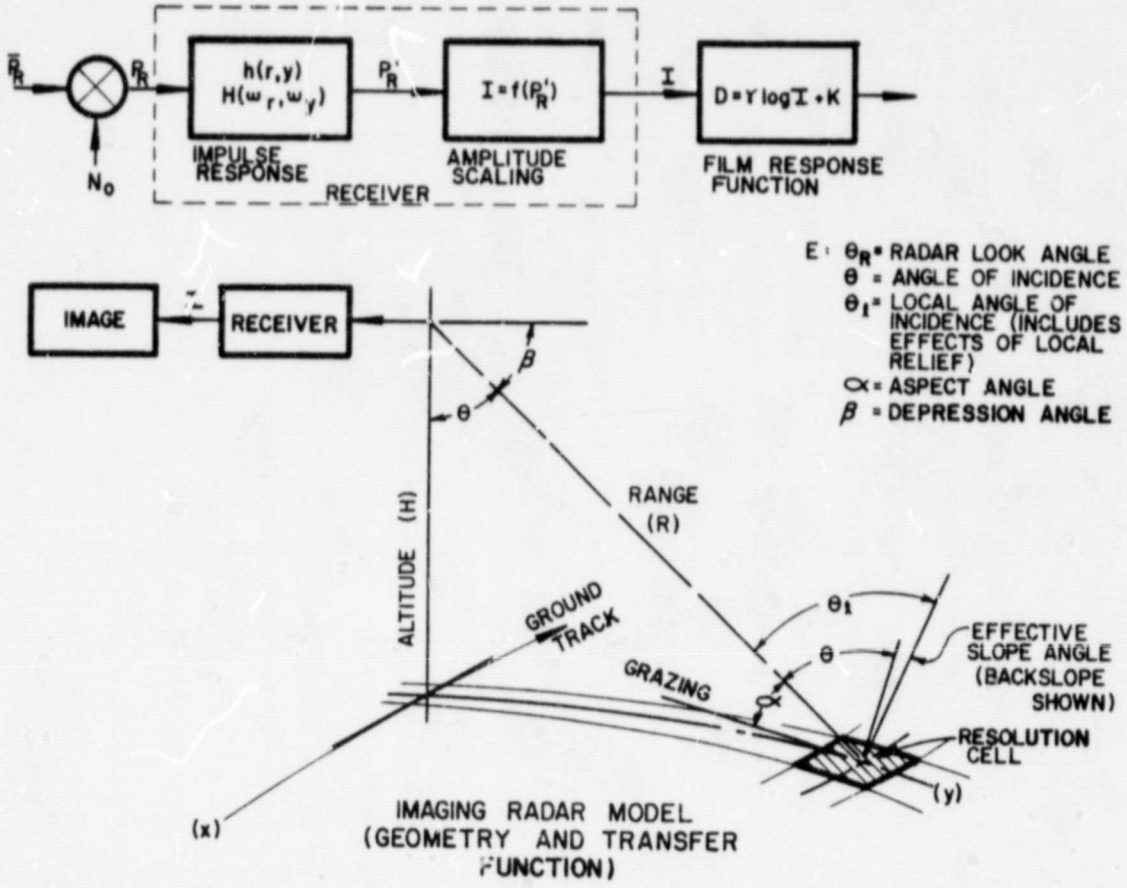

Figure 3: Transfer Function Model

3.4 POWER MAP IMAGE

The power map represents, in image form, the power density being reradiated from each point on the ground back in the direction of the radar antenna. The power map has no actual radar analogue, but it is an important interim result because it provides diagnostic evidence of backscatter effects without the perturbations of added geometric, or propagation distortions.

3.5 SLANT RANGE IMAGE

The slant-range image can be considered as either an interim product or a final image. The simulated slant-range image is directly analogous to an actual slant-range image. It embodies all the geometric distortions inherent in radar. The energy being returned to the radar has been sorted and re-arranged by time, or distance, in accordance with the geometry of the radar and the location of the individual resolution cell. Geometric distortions such as foreshortening, layover and shadow all are incorporated and properly displayed. In essence, the slant-range image represents a mapping from the spatial coordinates (x,y,z) of the ground into the image coordinates (r,y); range and azimuth, respectively.

3.6 GROUND RANGE IMAGE

The simulated ground-range image is directly analogous to an actual radar ground-range image. It represents a nonlinear mapping from a slant-range image space back into a ground-range (x,y) image space. All the distortions due to elevation (relief) in a slant-range image are accentuated when mapped into a ground-range image. This mapping preserves the geometric fidelity, or orthographic arrangement of features on a level surface such as the mean ground surface, but the location of any point above or below the flat surface, distorted in the slant-range image, is further distorted in the ground-range image.

Chapter 4

RESULTS AND DISCUSSIONS

Simulated radar images have been prepared for several geologic models. Simulation is used because it affords precise control over both input (ie., the geological model) and transformation of the input into a desired visual ouput format. Since each step is mathematically controlled, direct causal relationships and inferences can be discovered easily from the deterministic relationship between input and output.

Figures 4-7 present one set of simulated radar images created from the geologic landscape model illustrated in Figure 1. Figure 4 presents a power map. Figure 5 is a slant-range image. Figure 6 is a ground-range image, and Figure 7 is identical with Figure 6, except that noise has been added. This set of images simulates the results of an X-band radar (ie., one operating in the 5-12 Ghz region) with the radar being flown to the right across the top of each image from an altitude of 800 km. The radar operates with HH polarization (ie., Horizontal transmit and Horizontal receive) and the antenna is symbolically tilted so that it illuminates the terrain at an angle of 23 degrees in the center of the scene.

Observe in Figure 4 how well the spatial geometry and detail are preserved in the power map because none of the propagation phenomena inherent in radar have been introduced. This means, then, that the image it presents is unrealistic because it is unattainable from an actual radar. It contains a significant amount of information for our purposes, however, because it shows the normalized power density being reradiated back toward the antenna. Loosely stated, it is the photographic alternative to a radar image; as if it were somehow possible to illuminate the ground at X-band and photograph it directly.

The image presented in Figure 5 looks very different from the one in Figure 4. This is because the image in Figure 5 is a simulated slant-range radar image whereas the image in Figure 4 is not even a radar image. The slant-range image is a natural consequence of using radar to produce images. A ground distance of 8 km out to the side of the radar has been mapped (compressed), at the proper scale, into a slant-range distance of 3.13 km. We see at this angle an

Figure 4: 23 Degree
Power Map Image

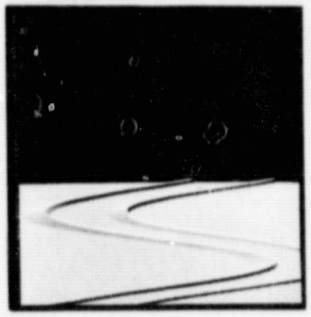

Figure 5: 23 Degree
Slant Range Image

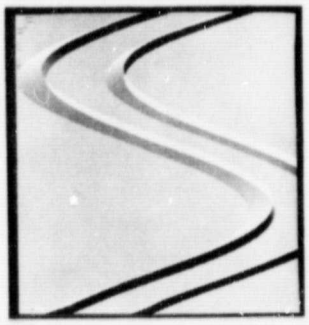

Figure 6: 23 Degree
Ground Range Image

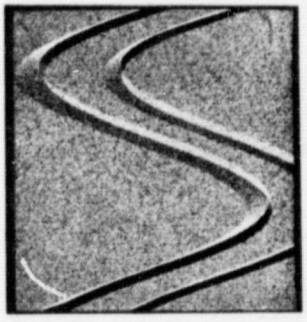

Figure 7: 23 Degree
Ground Range Image
with Noise

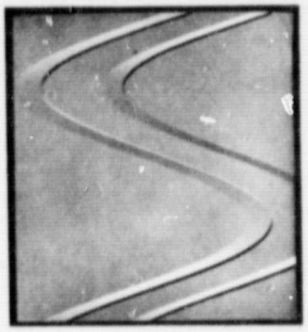

Figure 8: 40 Degree
Power Map Image

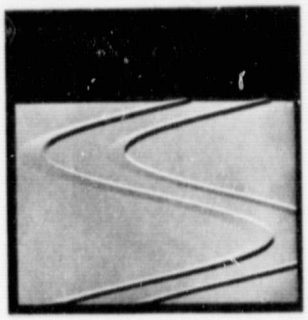

Figure 9: 40 Degree
Slant Range Image

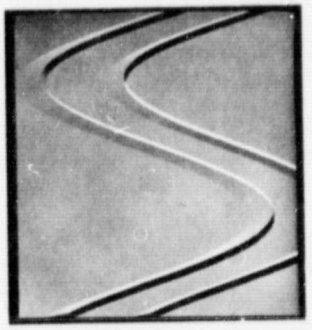

Figure 10: 40 Degree
Ground Range Image

Figure 11: 40 Degree
Ground Range Image
with Noise

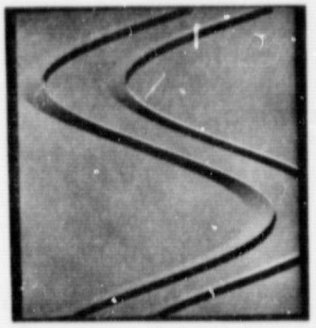

Figure 12: 60 Degree
Power Map Image

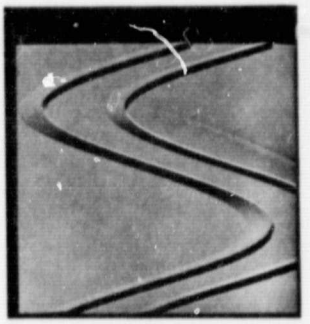

Figure 13: 60 Degree
Slant Range Image

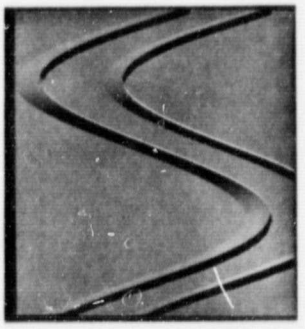

Figure 14: 60 Degree
Ground Range Image

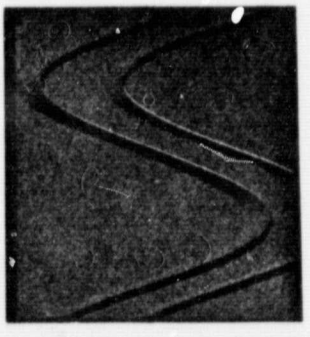

Figure 15: 60 Degree
Ground Range Image
with Noise

extreme example of compression, foreshortening, and layover. Since the data base is mathematical and, thus, smooth, it is easy for us to observe these effects.

Figure 6 shows a ground-range version of the slant-range image. In the ground-range image the compression evident in Figure 5 has been removed. Note how spatial distortion is exaggerated for features above (or equally for features below) level ground.

Figure 7 illustrates the ground-range image with statistical noise incorporated. Even for this simple, smooth, well-behaved figure, it is surprising to see how noise makes interpretation more difficult and less certain. If we had a feature contaminated with geologic noise (ie., small scale perturbations such as drainage and weathering effects, variations in the rock types, etc.), it is easy to imagine how difficult it would be to assess all of these effects, separately.

Figures 8-11 present the same sequence of simulated images from the same data base, but for a different angle. The angle for this set is 40 degrees. Evaluation of this set of images, like the previous one, shows that layover is still present though less pronounced. Spatial distortion, though, is much less severe. Note, however, how effectively the shape information is masked in the presence of noise.

Figures 12-15 present another sequence of simulated radar images for an angle of 60 degrees. Note the introduction of shadow. In this set of images, propagation effects are seen to be minimal and it is readily observed that the ground-range image agrees very favorably with the power map.

Chapter 5

CONCLUSIONS

These preliminary results show that digital image simulation and computer-modeling afford important advances for this kind of study. They provide cost-effective methods for evaluating terrain variations and sensor parameter changes, for predicting results, and for defining the optimum sensor parameters for a geologic application. In addition, they provide extremely useful mechanisms for teaching radar geology, and for defining an optimum interpretation strategy for a geologic application.

Chapter 6

ACKNOWLEDGEMENTS

The development of this digital simulation and computer modeling approach has been supported by the NASA JSC/Nonrenewable Resources Program Grant NAG 9-3.

REFERENCES

1 V. H. Kaupp, H. C. MacDonald, and W. P. Waite, "Imaging Radar: Analysis of Propagation Distortions", Arkansas Remote Sensing Laboratory Technical Report, ARSL TR 81-1, University of Arkansas, Department of Electrical Engineering, Fayetteville, Arkansas.

2 F. T. Ulaby, January 1975, "Radar Response to Vegetation", IEEE Transactions on Antennas and Propagation, Vol. AP-23, No. 1, pp. 36-45, and "Radar Response to Vegetation II: 8-18 GHz Band", IEEE Transactions on Antennas and Propagation, Vol. AP-23, September 1975, pp. 608-618.

3 R. L. Cosgriff, W. H. Peake, and R. C. Taylor, "Terrain Scattering Properties for Sensor System Design", Eng. Experiment Station Bulletin, 181, Vol. 29, Ohio State Universtiy, Columbus, Ohio, May 1960.

4 A. K. Fung, and H. L. Chan, September 1969, "Backscattering of Waves for Composite Rough Surfaces", IEEE Transactions on Antennas and Propagation.

5 R. A. Hevenor, October 1971, "Backscattering of Electromagnetic Waves from a Surface Composed of Two Types of Surface Roughness", TR ETL-TR-71-4, Engineering Topographic Laboratories, Tne United States Army, Fort Belvoir, Virginia.

6 J. W. Goodman, Introduction to Fourier Optics New York: McGraw Hill, 1968, pp. 150-153.

7 M. I. Skolnik (Editor), 1970, Radar Handbook R. K. Moore, "Ground Echo", New York: McGraw Hill.

8 R. K. Moore,"Microwave Remote Sensors", in R. G. Reeves, Manual of Remote Sensing, Falls Church,Virginia: American Society of Photogrammetry, 1975, Chapter 9.

Appendix B

USING RADAR IMAGE SIMULATION TO ASSESS RELATIVE GEOMETRIC DISTORTIONS INHERENT IN RADAR IMAGERY

V. H. Kaupp, Asst. Professor,
Dept. of Electrical Engineering
H. C. MacDonald, Professor,
Dept. of Geology
W. P. Waite, Professor,
Dept. of Electrical Engineering
University of Arkansas, Fayetteville, Arkansas 72701

Chapter 1

INTRODUCTION

Variation of the intensity or shade of grey (ie., tone) in radar images portrays the relative strength of the radar signal returned to the receiver from point to point on the ground. Variation of the radar signal arises from numerous interacting and complex causes. Two fundamental causes arise; first the interaction between the ground and the transmitted electromagnetic energy illuminating the ground, and second the geometric, or propagation, phenomena associated with the fact that radar is a ranging device (ie., it records the returned signal versus time and, thus, orders features according to their individual distances, or ranges to the radar).

Typically, the percentage of energy backscattered from slopes facing a radar is greater than from level terrain and from slopes facing away from a radar. Foreslopes are generally depicted in an image as brighter tones than level ground, and brighter still than backslopes. For the various terrain cover types present, this is governed by the backscatter trends versus the local angle of incidence (ie., the angle between the local vertical and a line to the radar). The geometric relationships are illustrated in Figure 1.

Geometric distortions arising from propagation phenomena perturb this picture. Typically in an image, areas of foreshortening and layover are represented by bright tones and regions of shadow by dark tones. This is because areas suffering foreshortening and layover cause the return signal from a relatively large ground area to be mapped into a smaller one. At the same time, shadowed regions are areas for which very little, if any, signal is returned to the radar.

In a radar image backscatter and propagation effects are simultaneously present and impossible to separate. Only through the experience gained in using radar imagery is it feasible to estimate the relative contribution of each effect for a specific tone in an image. Where it has been possible to check, we have observed a tendency for users to overestimate the backscatter contribution.

One unique method for observing the relative contributions of these effects is afforded by radar image simula-

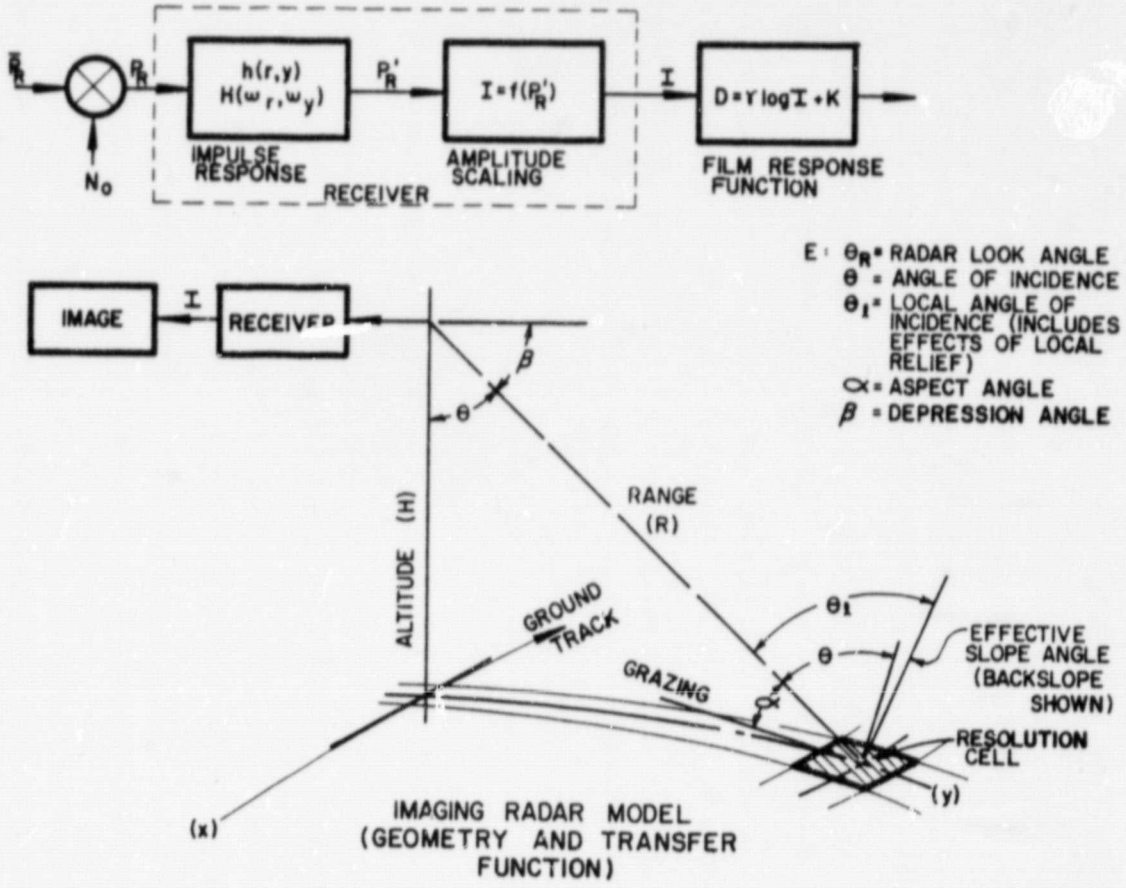

Figure 1: Radar Geometry

tion. Digital terrain data are used to model radar image formation. Both backscatter and propagation effects are separately modeled. These are serially incorporated and the image expression of each is noted. Sequences of images are presented illustrating these effects across a range of slopes and angles of incidence. The conclusions reached are that at angles of incidence smaller than the average slope of the terrain in a region, propagation phenomena dominate. As the angle of incidence increases beyond this, the radar image portrays an increasingly more faithful representation of the backscatter from the ground. It is also shown that digital simulation affords an important tool for evaluating complex interactions between the ground and radar, for training users in radar image interpretation, or for selecting optimum sensor parameters for specific applications.

Chapter 2

PROPAGATION PHENOMENA

An old radar image (circa 1957) of the Aichilik River Area in Alaska is presented in Figure 2 to illustrate the visual impact created by the various propagation phenomena. This radar image is a ground-range presentation recorded by the AN/APQ-56 system.

Figure 3 presents a topographic map for the region portrayed in the radar image. The topographic map illustrates that the mountainous terrain is relatively homogeneous whereas the radar image does not give that impression at all. The average slope of the terrain in the area is approximately 30 degrees. As can be seen in the image, the line A-C-E splits the image between the region in layover and the region not in layover. The line corresponds to an angle of incidence of approximately 30 degrees. Features above this line and, thus, nearer the radar, are in layover, while those below the line are not.

In the middle of the image (ie., in the mid-range region) note that foreslopes are brighter than backslopes, as expected. Foreshortening is maximum for features near the line A-C-E with a complete foreslope being mapped into a single line in the image. As the angle of incidence is increased and we move down the image away from the line A-C-E, note that foreshortening decreases and foreslopes are progressively mapped into larger areas in the image (closer to the actual scale size). In the far-range region, shadow begins to dominate the image presentation, foreshortening is minimized, and image tones are very nearly representative of the percentage of energy backscattered to the radar.

At the top of the image (ie., in the near-range region) layover dominates for mountainous terrain and it is very difficult to interpret the image. The VEE's so vivid in this region are the image expression of foreslopes in layover being exaggerated by a ground-range display. The tip of a VEE represents the topmost part of a mountain and is, thus, imaged closest to the radar.

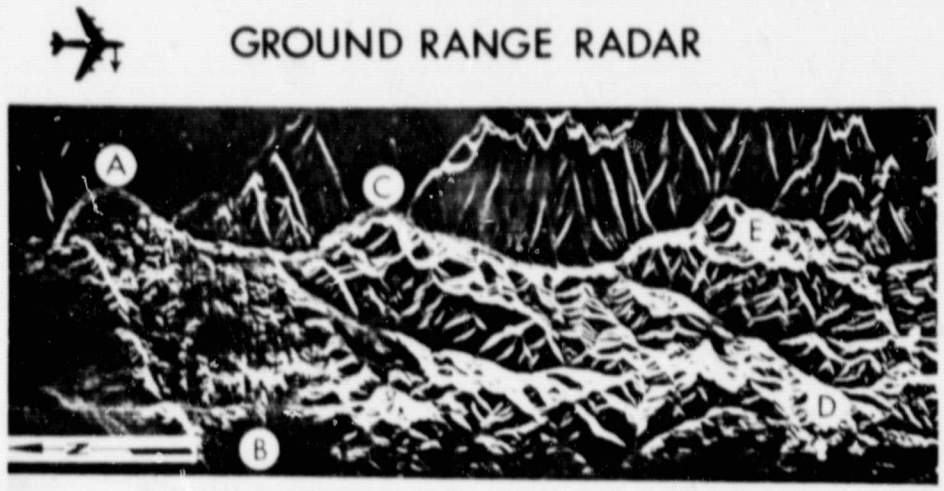

Figure 2: Aichilik River Area
Radar Image

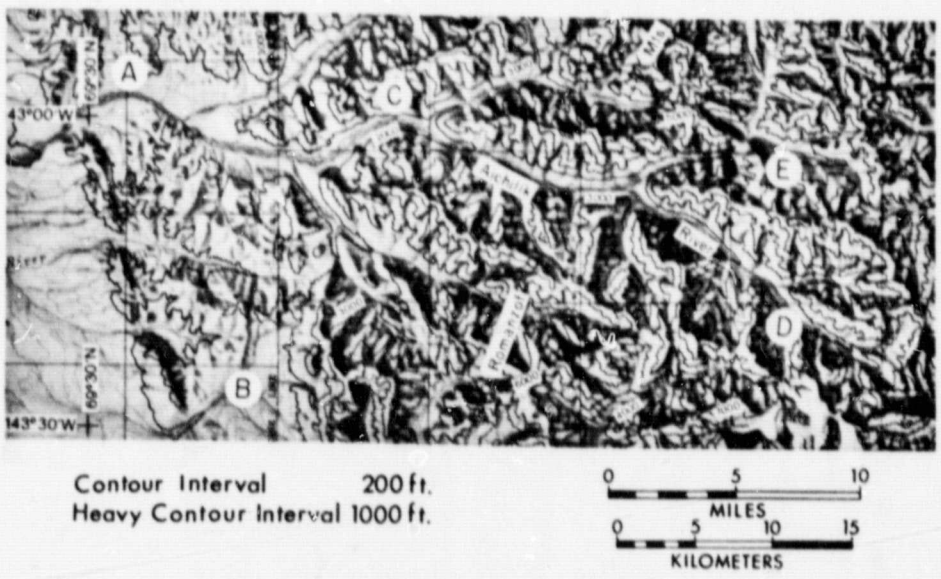

Figure 3: Aichilik River Area
Topographic Map

Chapter 3

BACKSCATTER

Radar return from the ground is described by σ° (the differential scattering cross-section, or scattering coefficient)[1]. The scattering coefficient, σ°, determines the electromagnetic energy reradiated back to the radar from the resolution cell. A resolution cell is defined for a short-pulse, side-looking, imaging radar to be the instantaneous area on the ground from which backscattered power arrives simultaneously at the radar antenna. A resolution cell is considered to consist of many individual features or objects relative to the scale of the radar wavelength, and each of these is termed a scattering element.

Figure 4 illustrates the trends of σ° versus local angle of incidence (θ_ℓ) for 4 typical surfaces: 1). specular or smooth; 2). slightly rough; 3). moderately rough; and 4). extremely rough. The scale of the roughness in terms of the wavelength of the incident radiation is what determines this characteristic. A given surface may appear almost smooth at sufficiently low frequencies (ie., at long wavelengths) and, thus, exhibit nearly specular reflection. As the frequency is increased (ie., as wavelengths become shorter) the same surface will appear progressively rougher until it becomes extremely rough and, thus, exhibits nearly uniform backscatter[2]. The scale of roughness of a surface relative to the radar frequency, within the limitations of this simplistic, general discussion, defines the shape of the vs curve. As can be seen, the surface that is smooth relative to the radar wavelength produces an extremely strong return only when the local angle of incidence is zero degrees with the strength of the return falling off rapidly as the angle is increased. An extremely rough surface relative to the radar wavelength is shown to have a σ° vs θ_ℓ trend which is almost a horizontal line. In addition, σ° vs θ_ℓ trends are shown for two intermediate surfaces. As might be expected, the slightly rough surface exhibits a more specular trend whereas the moderately rough one exhibits a more uniform trend.

Generally speaking, we can summarize backscatter trends in imagery as follows. For a given scale of roughness and complex permittivity, the smaller the local angle of incidence the higher the backscatter and the brighter the image tone. Foreslopes, typically, have small angles ($\theta_\ell < 30$ de-

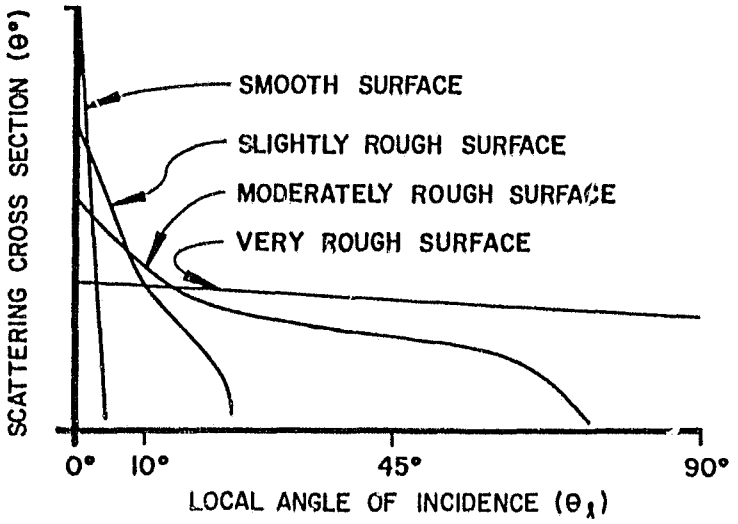

APPROXIMATE BACKSCATTERING RESPONSE OF ROUGH SURFACES (ROUGHNESS RELATIVE TO THE TRANSMISSION WAVELENGTH IS INDICATED)

Figure 4: Backscatter Trends

grees) and, thus, relatively high backscatter. Couple this with the geometric effects of compression and layover and the image tone is very bright; often it is saturated (ie., white). Once recorded in imagery, the two effects, backscatter and geometric, cannot be separated. In addition, the resulting image is probably uninterpretable in such areas due to geometric distortions. The greater the θ_ℓ, as is frequently the case for backslopes, the darker the image tone. Within 5 degrees to 10 degrees of grazing (ie., 80 degrees $< \theta_\ell <$ 90 degrees) the backscatter begins to fall off very rapidly.

Chapter 4

RESULTS AND DISCUSSIONS

Computer-generated radar images have been prepared via the University of Arkansas' radar image simulation programs[3] to illustrate the separate effects caused by propagation phenomena and backscatter. Five different intermediate and final results can be produced. These are: 1). power map; 2). slant-range image; 3). ground-range image; 4). slant-range image with noise; and 5). ground-range image with noise. Simulation is especially beneficial for separating propagation effects from those of backscatter because these effects, inseparable in actual imagery, can be modeled as serial events and the impact of each can be assessed, separately.

Figures 5-8 present one set of simulated radar images created from an input which is deterministic and ideally suited to such a study. It is the geological landscape model of a breached anticline and syncline structure previously presented[3]. This particular geologic model was created mathematically. As can be seen in Figure 5, the model represents a textbook example of an anticline and a syncline structure. The anticline is readily identified as the structure having the long nose and infacing escarpements, while the syncline has no nose and outfacing escarpements.

Figure 5 presents a power map. Figure 6 is a slant-range image. Figure 7 is a ground-range image, and Figure 8 is identical to Figure 7, except that noise has been added. This set of images simulates the results of an X-band radar (ie., one operating in the 5-12 GHz region) with the radar being flown to the right across the top of each image at an altitude of 800 km. The radar operates with HH polarization (ie., Horizontal transmit and Horizontal receive) and the antenna is symbolically tilted so that it illuminates the terrain at an angle of 23 degrees in the middle of the scene.

Observe in Figure 5 how well the spatial geometry and detail are preserved in the power map. This is because in the power map none of the propagation phenomena inherent in radar have been introduced. This means that the image it presents is unrealistic because it is unattainable from an actual radar. It contains a significant amount of information for our purposes, however, because it shows the normal-

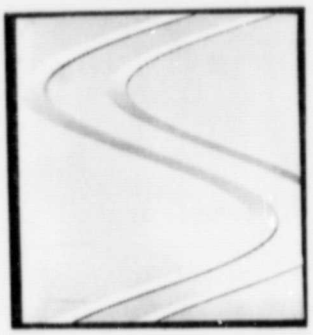

Figure 5: 23 Degree
Power Map Image

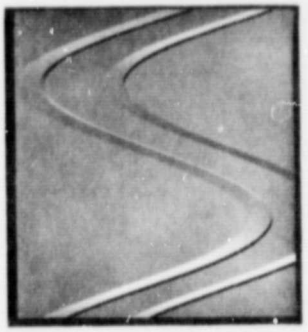

Figure 9: 40 Degree
Power Map Image

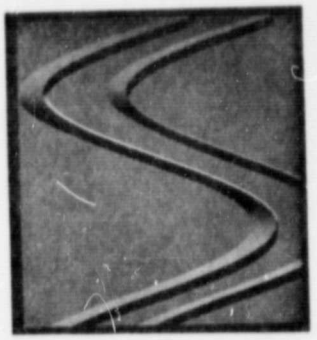

Figure 13: 70 Degree
Power Map Image

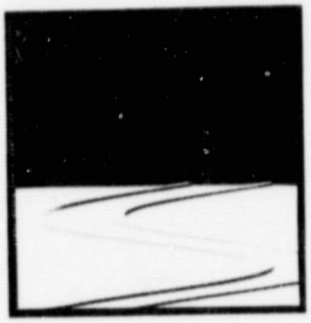

Figure 6: 23 Degree
Slant Range Image

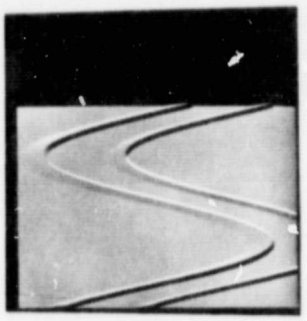

Figure 10: 40 Degree
Slant Range Image

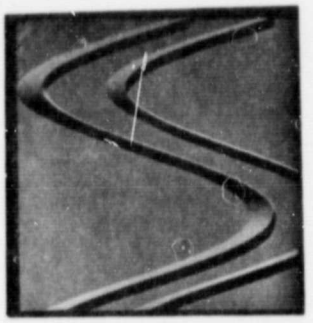

Figure 14: 70 Degree
Slant Range Image

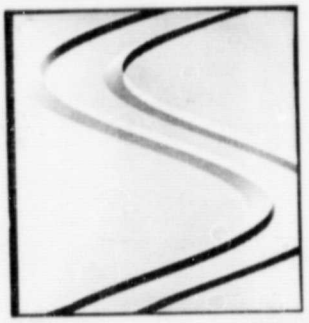

Figure 7: 23 Degree
Ground Range Image

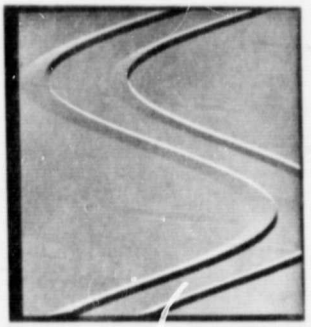

Figure 11: 40 Degree
Ground Range Image

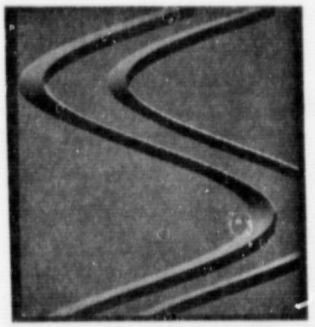

Figure 15: 70 Degree
Ground Range Image

Figure 8: 23 Degree
Ground Range Image
with Noise

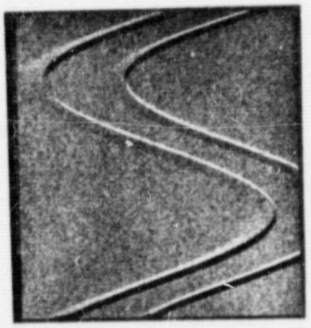

Figure 12: 40 Degree
Ground Range Image
with Noise

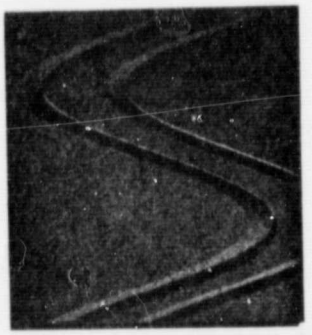

Figure 16: 70 Degree
Ground Range Image
with Noise

ized power density (ie., it is proportional to the actual backscatter) being reradiated back toward the antenna. Loosely stated, it is the photographic alternative to a radar image; as if it were somehow possible to illuminate the ground at X-band and photograph it directly.

Note in Figure 5 how each slope facing the radar (foreslope) is bright except the very steep ones, and each slope facing away (backslope) is dark relative to the tone of the background. Thus, as would be expected from typical backscatter trends (eg., Figure 4), foreslopes are brighter and backslopes are darker than the background.

The image presented in Figure 6 looks very different from the one in Figure 5. This is because the image in Figure 6 is a simulated slant-range radar image whereas the image in Figure 5 is not even a radar image. The slant-range image is a natural consequence of using radar to produce images. A ground distance out to the side of the radar of 8 km has been mapped (compressed), at the proper scale, into a slant-range distance of 3.13 km. We see at this angle an extreme example of compression, foreshortening, and layover. Follow the trace of the base of the geologic structure across the image. It is easily identified throughout most of the image as the boundary between the background and a darker tone. This is especially visible for the ridges running across the central portion of the image swath (ie., from the leftmost curve to the rightmost one). After finding the trace of the base, compare with Figure 5 and observe how the top of the ridge has been displaced toward the radar (ie., toward the top of the image). This is easily ascertained by finding the trace of the top of the ridge as the boundary between a brighter tone and the background.

Figure 7 shows a ground-range version of the slant-range image. In the ground-range image the compression evident in Figure 6 has been removed, and the trace of the base of the geologic structure preserves spatial geometry. Note how spatial distortions are exaggerated for features above (or equally for features below) level ground.

Find, now, the trace of the top of the ridge in this figure (7). It is easy in this figure to trace the top across the image. Observe how in the central portion of the swath the top is imaged before the bottom and is, thus, laid over. As the trace of the top of the ridge is followed around the curve going down the image, two crossings of the base occur. This represents a transition in the local angle of incidence from a region of layover to one of foreshortening and back to layover again. Following the trace of the top of the ridge up the image shows similar effects.

Again, compare the ground-range and power map images (Figures 5 and 7). Observe the spatial distortions that are evident. Observe also how tones are distorted. Slopes that are in layover are significantly brighter than predicted in the power map image. It is interesting to evaluate only the central ridge. The true spatial geometry is depicted in Figure 5. Compare this to the backslope in Figure 7. Since the terrain is continuous, the backslope must be the area occupying the region in the image from the top of the ridge to the base on the bottom side. We know the top of the ridge is in layover in this region (ie., top imaged before the bottom), so the backslope must extend from the top of the white trace (ie., top of the ridge) to the bottom of the dark trace (ie., bottom on backslope side). The backslope is, thus, stretched out and banded. The first band, the lower one, is the correct tone for the backslope, as can be verified by comparing with Figure 5. The second band, the upper bright one, consists of the power returned from part of the backslope, the foreslope, and level terrain in front of the ridge. In fact, it is only because we have such a well-behaved feature that it's fairly easy to interpret it properly.

Figure 8 illustrates the ground-range image with statistical noise incorporated. Even for this simple, smooth, well-behaved figure, it is surprising to see how noise makes the interpretation of this image more difficult and less certain. If we had a feature contaminated with geologic noise (ie., small scale perturbations such as drainage and weathering effects, variations in the rock types, etc.), it is easy to imagine how difficult it would be to assess all of these effects. We see, therefore, how radar image simulation is valuable for evaluating the separate impacts of various phenomena. The basic conclusion drawn from this set of images representing a small incidence angle is that propagation effects dominate backscatter ones.

Figures 9-12 present the same sequence of simulated images from the same data base, but for a 40 degree angle of incidence; power map, slant-range, ground-range, and ground-range with noise images, respectively. As can be seen from the various images, compression is less severe (ie., 8 km mapped into 5.142 km) as are all the propagation effects. Evaluation of this set of images, like the previous set, shows that layover is still present though less pronounced. Thus, propagation phenomena dominate backscatter effects even at this intermediate angle. Spatial distortion, though, is much less severe. Note, however, how effectively the shape information is masked in the presence of noise.

Figures 13-16 present another sequence for an angle of incidence of 70 degrees. Note the introduction of shadow.

This can be seen both in the images and by the fact that the local angle of incidence has exceeded the grazing angle. In the set of images, propagation effects are seen to be minimal (ie., 8 km mapped into 7.52 km) and it is readily observed that the ground-range image agrees very favorably with the power map. For this large angle set, then, it is readily seen that spatial geometry is nearly preserved and the image almost records the true backscattered signal relationships.

Chapter 5

CONCLUSIONS

Simulation was used to decouple image effects thereby allowing evaluation of the image expression of each separate effect. It was shown that propagation phenomena are important distortions, at least for radar imagery collected at angles of incidence less than 40 degrees, which must be properly accounted for when interpreting such imagery. Improper allowance for propagation distortions will lead to incorrect interpretations and erroneous beliefs regarding the properties of the ground because the relative amount of backscatter and the terrain slope will likely be misjudged. From the evidence presented, it was shown that the dominating factor in determining the level of brightness in an image is propagation phenomena for small angles of incidence, and backscatter for large angles. From this study it is obvious that digital simulation affords an important tool for correctly interpreting image distortions, and for training users in radar image interpretation.

Chapter 6

ACKNOWLEDGEMENTS

The work resulting in this analysis of radar image distortions was supported by the NASA JSC/Nonrenewable Resources Program Grant NAG 9-3.

REFERENCES

1 M. I. Skolnik (Editor), 1970, Radar Handbook, R. K. Moore, "Ground Echo", New York: McGraw Hill.

2 W. P. Waite, H. C. Macdonald, J. S. Demarcke, and B. H. Corbell, "Look Direction Dependence of Radar Backscattering Cross Section for Agricultural Fields", Proc. Amer. Soc. Photogramm., Fall Technical Meetings, Niagara Falls, N.Y., October 1980, p.R-2-6-1-14.

3 V. H. Kaupp, H. C. MacDonald, and W. P. Waite, "Geologic Terrain Models", Proceedings of the 1981 International Geoscience and Remote Sensing Symposium, June 1981, Washington, D.C.

Appendix C

WHICH ANGLE OF INCIDENCE IS BEST FOR IMAGING RADARS?

V. H. Kaupp, Asst. Professor,
Dept. of Electrical Engineering
W. P. Waite, Professor,
Dept. of Electrical Engineering
H. C. MacDonald, Professor,
Dept. of Geology
University of Arkansas, Fayetteville, Arkansas 72701

Chapter 1

INTRODUCTION

It has been held, traditionally, that the value of radar imagery is increased for most applications when the angle of incidence is large. Figure 1 illustrates the geometry for an imaging radar over a curved earth and identifies various, important relationships such as angle of incidence. With the advent of spaceborne imaging radars such as the SEASAT synthetic aperture radar, it is often infeasible to attain these desired angles for practical reasons. The tradeoffs required between frequency, antenna size, and power availability are the most limiting of these reasons.

Because the large angles which are desired (ie., $\theta > 60$ degrees) for most geological work are unattainable, a study is being conducted to assess the usefulness of imagery collected at smaller angles for satisfying geological needs. The study consists of obtaining and evaluating radar imagery collected at numerous angles of incidence for specific geological features. Since it is generally impossible to find suitable imagery of a specific feature illuminated across the complete range of angles, radar image simulation is being employed to accomplish this. The value of using simulation and computer-generated imagery is clearly established in studies such as this one.

Preliminary results indicate that the usefulness of radar imagery is highly dependent upon the application. Imagery collected at small angles of incidence was found to be useful for applications involving study of low relief terrain because typical trends of the backscatter coefficient versus the local angle of incidence results in enhanced contrast for such features in imagery; a conclusion also reached by Ford[1]. Figure 2 illustrates a curve showing typical backscatter trends. These typical trends are presented for their relative shape information, so neither amplitude scale nor frequency and polarization are identified.

Imagery collected at large angles of incidence was found to be most useful for applications involving study of mountainous terrain because of the outlining effect of radar shadow and because geometric distortions are minimized. Imagery collected at intermediate angles was found to serve neither type of application best, but probably offers a compromise for viewing mixed terrain types since large angles

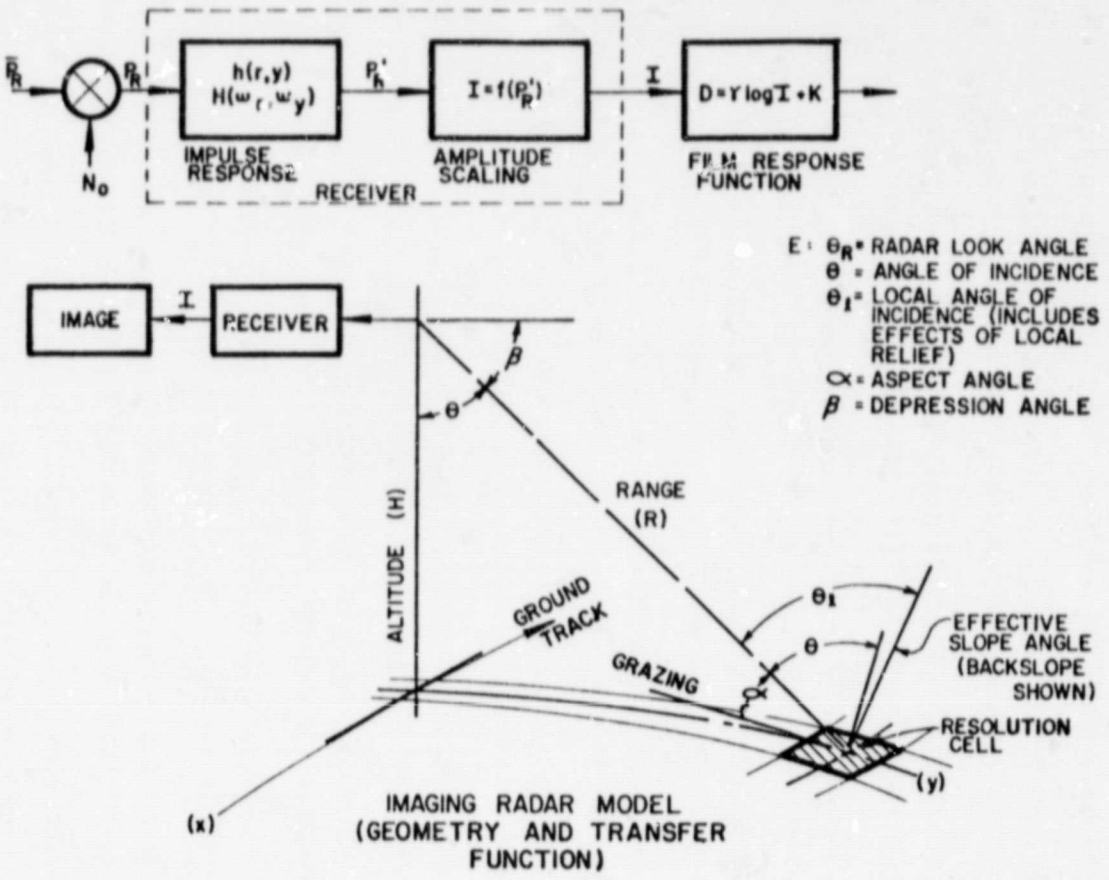

Figure 1: Radar Geometry

are difficult to attain. A system having at least two selectable angles of incidence, one small and one large, would probably be the best one for imaging mixed terrain.

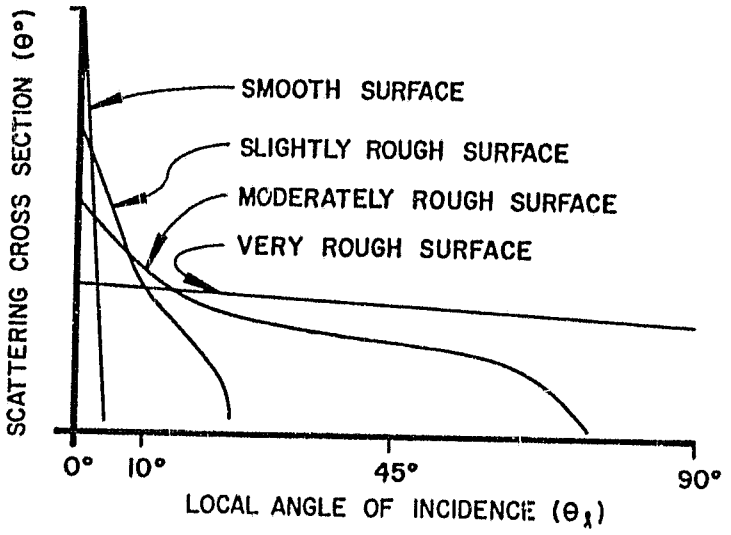

APPROXIMATE BACKSCATTERING RESPONSE OF ROUGH SURFACES (ROUGHNESS RELATIVE TO THE TRANSMISSION WAVELENGTH IS INDICATED)

Figure 2: Backscatter Trends

Chapter 2

INCIDENCE ANGLE EFFECTS IN RADAR IMAGERY

We have observed that the detail and fidelity portrayed in radar images of different kinds of terrain is dependent upon both the relative relief of the terrain as well as the radar angle of incidence. This observation was drawn from analyzing computer-generated radar images portraying a single scene imaged at numerous different angles of incidence, and it was validated by comparing these to actual imagery.

The computer-generated images were created by using the University of Arkansas' radar image simulation computer programs[2,3]. Four of these simulated radar images are presented as ground-range images in Figures 3-6. Each of the figures illustrates the same scene imaged from spacecraft altitudes at a specific radar angle of incidence; 23 degrees, 40 degrees, 60 degrees, and 80 degrees, respectively. The relative relief for every point in the scene was obtained from a digital terrain tape of the NJ 16-12E standard USGS topographic map[4]. Data on this tape recorded the elevation of the area on a 91.44 m sampling grid.

Each image consists of an array of 512 x 512 points, or pixels (ie., picture elements). Each pixel represents a ground spot of 91.44 m x 91.44 m. The scene in each figure portrays, therefore, a ground-range image of 2192 sq km (ie., 46.8 km on each side) in the southern Appalachian basin region of Tennessee. Two types of terrain are present in this region: 1). maturely dissected mountains, and 2). elongated mountain slopes.

Figure 3 presents a computer-generated ground-range image of the Tennessee terrain for a spaceborne radar orbiting the earth at 800 km and viewing the scene at an incidence angle of 23 degrees. In this simulated scenario, the angle of incidence is 21.6 degrees at the near-range edge, 23.0 degrees in the middle, and 24.4 degrees at the far-range edge of the scene. Observe in this scene how the maturely dissected mountainous terrain is distorted by extreme layover and further distorted by the ground-range presentation resulting in the characteristic VEE's pointing toward the radar, as previously discussed[5]. The presentation of mountainous terrain in this angular range severely distorts the geometric fidelity, thereby making such radar images only marginally useful for many geological investigations.

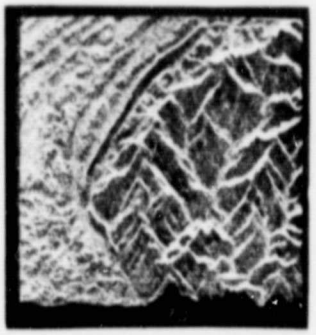

Figure 3: 23 Degree
Ground Range Image
with Noise

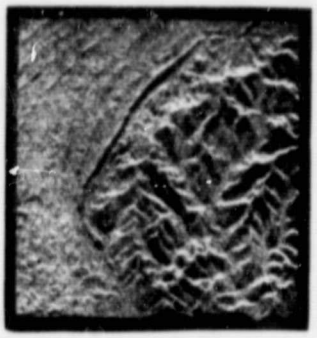

Figure 4: 40 Degree
Ground Range Image
with Noise

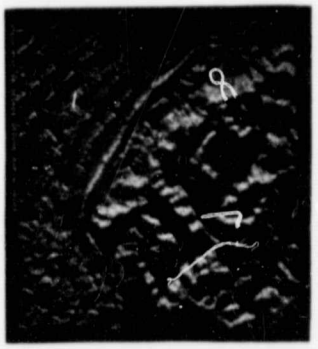

Figure 6: 80 Degree
Ground Range Image
with Noise

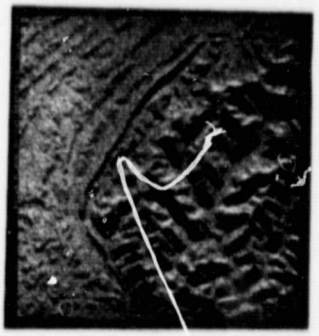

Figure 5: 60 Degree
Ground Range Image
with Noise

Note the sharp detail (ie., enhanced contrast) and apparent fidelity of the presentation in this image of the low relief, elongated ridge terrain. Even though compression and layover are present, the images of this terrain-type is useful for many investigations. The sharpness in this area is attributed to the sensitivity of the typial backscatter coefficient to small angular changes near nadir.

A curve showing the typical trends of backscatter coefficient versus local angle of incidence is presented in Figure 2. Since the backscatter coefficient determines the amount of electromagnetic energy reradiated from each resolution cell back to the radar, it is the fundamental mechanism which determines the shade of grey (or tone) of each pixel. As can be seen in the figure, small angular changes around an average angle of 23 degrees result in relatively large changes in the backscatter coefficient. The large backscatter changes are recorded in imagery as large variations in the tone from pixel to pixel. In this way, the radar expression of terrain that is very rough but not mountainous relative to the radar wavelength is recorded with enhanced contrast in imagery collected at an angle of incidence of 30 degrees (approximately), or less.

In the 30 degrees to 70 degrees region (approximately), the typical backscatter trend shows a marked reduction in the slope. We would expect small angular variations associated with very rough terrain when viewed in this region to result in imagery having very little contrast. This is precisely what is shown in Figures 4 and 5. In Figure 4, the angle of incidence is 39.0 degrees at the near-range edge, 40.0 degrees in the middle, and 41.0 degrees at the far-range edge. In Figure 5, these angles are 59.6 degrees, 60.0 degrees, 60.4 degrees, respectively. Note in both figures how the contrast has been reduced for the very rough terrain to the point where, in comparison to the presentation in Figure 3, these images are no longer indicative of the topography.

The mountainous terrain exhibits only a slight amount of layover in Figure 4, but compression is still severe(ie., 36%). This causes the linear extent of foreslopes to be foreshortened, or compressed in an image. The image of such foreslopes is largely uninterpretable. Figure 4, thus, illustrates a radar image that is only marginally useful.

Very little, if any, of the mountainous terrain is laid-over in Figure 5. Even though compression still exists at a 60 degree angle of incidence (ie., 13%), it does not cause significant distortions for most terrain. For this terrain, the appearance of radar shadow aids interpretation in the mountainous region. This image, then, marks the transition

point (approximately) from which radar imagery of mountainous regions is most interpretable. Despite the appearance of shadow, the image of the low relief terrain is not nearly as useful as the one in Figure 3.

The simulated image presented in Figure 6 was produced to represent a 79.9 degree angle of incidence at the near-range, 80.0 degrees in the middle, and 80.1 degrees at the far-range edge. This is a spectacular image even though dominated by shadow. It is easy to see why imagery near this incidence angle is so highly desired by geologists. It is shown only for comparison since a basic premise underlying our work here is that large angles are presently unattainable from spacecraft altitudes. Further analysis of this image indicates this angular region (ie., near grazing) marks (approximately) the point where a typical backscatter curve again enjoys a significant slope (eg., Figure 2). This is a region, just like the one near nadir, where small angular changes result in increased image contrast. For certain types of terrain, this occurs. Often, though, shadow dominates, causing loss of much information, but radar imagery in this angular region seems highly desirable for the great clarity of presentation it affords for most terrain types.

Chapter 3

CONCLUSIONS

The detail and fidelity portrayed in radar imagery of different kinds of terrain is dependent upon both the relative relief of the terrain as well as the radar angle of incidence. The usefulness of radar imagery for geological applications is, thus, dependent upon the application. Analysis of our preliminary results show, even though only a very limited range of parameters have been evaluated, that large incidence angle radar imagery is best for many geologic applications. If we accept the premise that these angles are unattainable, then our preliminary results indicate that applications which involve study of low relief terrain can be served best by imagery collected at small angles-of-incidence (ie., $\theta < 30$ degrees), and applications which require study of mountainous terrain can be served best by imagery produced at the largest angles-of-incidence attainable (ie.,$\theta > 60$ degrees). The angular range in between these serves neither low relief nor mountainous terrain as well, but offers a compromise. Further study is needed to evaluate additional parameters to see if a particular combination will provide imagery having increased contrast and clarity in this intermediate angular range. In general from our preliminary work, it would appear that for a mix of terrain types the best compromise is offered by a system having at least two selectable angles-of-incidence; one small and one large. The next best compromise is probably offered by a system viewing the scene only at the largest angle-of-incidence which can be attained within the spacecraft limitations.

Chapter 4

ACKNOWLEDGEMENTS

The work resulting in this analysis of angle of incidence relationships in radar imagery was supported by the NASA JSC/Nonrenewable Resources Program Grant NAG 9-3.

REFERENCES

1 J. P. Ford, "Seasat Orbital Radar Imagery for Geologic Mapping: Tennessee-Kentucky-Virginia", AAPG Bulletin, Volume 64/12, December 1980, p. 2064-2094.2.

2 V. H. Kaupp, H. C. MacDonald, and W. P. Waite, "Imaging Radar: Analysis of Propagation Distortions", Arkansas Remote Sensing Laboratory Technical Report, ARSL TR 81-1, University of Arkansas, Department of Electrical Engineering, Fayetteville, Arkansas.

3 V. H. Kaupp, H. C. MacDonald, and W. P. Waite, "Geologic Terrain Models", Proceedings of the 1981 International Geoscience and Remote Sensing Symposium, June 1981, Washington, D.C.

4 (Anonymous), "Digital Terrain Tapes, User Guide", Second Edition, National Cartographic Information Center, U. S. Department of The Interior, Geological Survey, U. S. Government Printing Office: 1980, 0-311-344/184.

5 V. H. Kaupp, H. C. MacDonald, and W. P. Waite, "Using Radar Image Simulation to Assess Relative Geometric Distortions Inherent in Radar Imagery", Proceedings of the 1981 International Geoscience and Remote Sensing Symposium, June 1981, Washington, D.C.